ION-BEAM-ASSISTED DEPOSITION OF TRANSPARENT CONDUCTIVE THIN FILMS: ON THE WAY TOWARD REPLACING INDIUM TIN OXIDE

By

Thanh Tran

A DISSERTATION

Submitted to
Michigan State University
in partial fulfillment of the requirements
for the degree of

Materials Science and Engineering- Doctor of Philosophy

2024

ABSTRACT

In light of the escalating costs of Indium Tin Oxide, the quest for its sustainable alternatives becomes imperative. This dissertation delves into the utilization of a single-beam ion source in conjunction with magnetron sputtering to manipulate film microstructures, aiming to enhance and fabricate transparent conductive electrodes.

Through the assistance of the ion source, an extensive range of modulation in the magnetron voltage was achieved. This mechanism led to a low-voltage high-current magnetron discharge, facilitating a 'soft sputtering mode' conducive for thin film growth. Indium tin oxide (ITO) thin films were successfully deposited at room temperature by employing a combined single-beam ion source and magnetron sputtering, resulting in the creation of polycrystalline ITO thin films characterized by significantly reduced resistivity and surface roughness.
Notably, the ion beam treatment played a pivotal role in the growth of a silver seed layer, approximately 1 nm in thickness, enhancing the subsequent silver film's wettability. This, in turn, led to the creation of a continuous silver film of approximately 6 nm, boasting a resistivity of 11.4 μΩ.cm.

To enhance stability of resulting silver ultra-thin films, an approach involving a cap layer of aluminum on silver was introduced. The resulting film, composed of a 1 nm buffer layer of ion beam-treated silver, a layer of pure silver sputter-deposited, and a 0.2 nm nominal thick cap layer of aluminum, significantly bolstered the film's stability without a marked compromise on its optical and electrical properties. Further, thermal treatment of the duplex film led to an enhancement in its electrical conductivity and optical transmittance owing to an improvement in crystallinity. The annealed aluminum/silver duplex structure exhibited low electrical resistance

and high optical transmittance, comparable to simulated results, positioning it among the top films reported.

The stabilized ultra-thin silver films were then leveraged to craft highly transparent and conductive electrodes on glass substrates in a sandwich structure with optimized layers of indium tin oxide (ITO). Notably, exceptional thermal stability was achieved, and annealing at 200°C in vacuum and air enhanced the film's optical and electrical performance. The resultant electrodes showcased outstanding transparency, conductivity, and thermal stability, positioning them favorably for architectural glass coatings and optoelectronic applications such as photovoltaics and displays.

Further computational works were conducted to study the optical performances of six different sandwich structures on glass, comprising typical transparent conductive oxides with an ultra-thin layer of silver at 6 nm and 7 nm in the middle. The simulation finds Glass/TiO_2/Ag/AZO, Glass/TiO_2/Ag/SnO_2 and Glass/SnO_2/Ag/SnO_2 structures exhibiting high optical performances, comparable to ITO in solar-cell and display applications, theoretically. This dissertation also shows some other examples of optimizing the optical performance of the structures for specific applications. Furthermore, a case study was conducted to explore the use of tantalum-doped tin oxide (TTO) as a viable alternative to ITO. Employing a room temperature treatment facilitated by a single beam ion source, highly transparent and conductive TTO films were produced. Specifically, the TTO thin film achieved a resistivity as low as 9.3 mΩ.cm and an average transmittance of 79% in the 400 nm to 1200 nm range. In contrast, without ion beam assistance, the minimum resistivity achieved was 15.9 mΩ.cm, accompanied by an average transmittance of 78% within the same wavelength range.

This dissertation is dedicated to my family.

ACKNOWLEDGEMENTS

Completing this Ph.D. research demanded not only personal dedication and effort but also the unwavering support of numerous individuals, all of whom I attempt to acknowledge in the following paragraphs.

First, I extend my deepest gratitude to my advisor, Dr. Qi Hua Fan, for entrusting me with the role of his graduate research assistant. Dr. Fan has been a pillar of support, readily available to offer guidance and assistance in steering research projects, even dedicating time on weekends. His mentorship not only provided close guidance but also encouraged the exploration of innovative ideas, allowing for a creative approach to my research endeavors.

I am appreciative of the guidance and constructive insights provided by other esteemed members of my Ph.D. committee, namely Dr. Jason D. Nicholas, Dr. Wen Li, Dr. Alexandra Zevalkink, and Dr. Wei Lai. Their valuable inputs and comments during my comprehensive exam and dissertation were instrumental in shaping the direction of my research and enhancing its quality.

My appreciation extends to my colleagues, classmates, and lab mates: Maheshwar Shrestha, Nina Baule, Bocong Zheng, Young Kim, Keliang Wang, Xiaobo Wang, and Al-Ahsan Talukder – for engaging in enlightening scientific discussions and extending their invaluable technical assistance.

Furthermore, I am indebted to the Department of Chemical Engineering and Materials Science at MSU for their exceptional administrative and technical support, which significantly facilitated the progression of my research activities. Special mention goes to individuals such as Heather Dainton, Jessica Gallegos, and Per Askeland for their contributions.

Lastly, it's important to note that there are numerous others whose names may not be included here. I am grateful for the support each of you provided in making this work possible.

TABLE OF CONTENTS

CHAPTER 1

BACKGROUND INFORMATION

1.1 Background Knowledge and Motivation

Transparent conductive materials were first reported in 1907 [1]. It was not until 1970s that indium-tin oxide (ITO) was found. It is a compound composed of indium, tin, and oxygen, typically with the chemical formula $In_2O_3 \cdot SnO_2$ and In_2O_3 is the main oxide. Since then, with the exponential growth of displays and touch screens, ITO has become the most important transparent conductive electrode (TCE) in photoelectronic devices. ITO contributes the most to the TCE market with two main products: ITO on glass and ITO on polyethylene terephthalate (PET). Compared with other TCEs, ITO has excellent electrical conductivity, optical transmittance, and environmental stability.

Transparent conductive films find applications in various industries and technologies where the combination of optical transparency and electrical conductivity is essential. Here are some common applications:

- Touchscreens: Transparent conductive films are integral to capacitive touchscreens in smartphones, tablets, and other electronic devices. They enable users to interact with the screen through touch gestures.
- Liquid Crystal Displays (LCDs): LCDs in TVs, monitors, and laptops use transparent conductive films to control individual pixels by applying electrical signals.
- Solar Panels: Transparent conductive oxide (TCO) films, such as indium tin oxide (ITO), are applied to solar panels to collect generated electricity and improve light absorption.

- Smart Windows: These windows can change their transparency in response to environmental conditions. Transparent conductive films enable this feature in applications like energy-efficient buildings and automobiles.
- Flexible Electronics: Transparent conductive films on flexible substrates allow for the creation of bendable electronic devices and wearable technology.
- Electroluminescent Displays: Organic light-emitting diode (OLED) displays and organic LEDs (OLEDs) use transparent conductive films as an anode layer.
- Antistatic Coatings: Transparent conductive coatings are applied to materials like eyeglasses, camera lenses, and computer screens to prevent static buildup.
- Electromagnetic Interference (EMI) Shielding: Transparent conductive films can be used in applications where EMI shielding is necessary, such as in electronic devices or medical equipment.
- Resistive Heaters: Transparent conductive films can be used for applications like defogging or deicing surfaces in automobiles and aircraft.
- Smart Mirrors: These mirrors can display information like weather updates, news, or other digital content. Transparent conductive films enable touch or gesture control on the mirror's surface.
- Electrochromic Windows: These windows can change their tint or color in response to an electrical signal, offering energy-efficient solutions for buildings and vehicles.
- Biotechnology and Sensing Devices: Transparent conductive films are used in biosensors, lab-on-a-chip devices, and medical diagnostics for their electrical and optical properties.

- Light-Emitting Devices: Transparent conductive films are used as anodes in electroluminescent devices, such as EL displays and EL lamps.
- Flexible Transparent Electrodes: In applications like flexible displays, transparent conductive films with bendable substrates enable the creation of rollable and foldable screens.

High transmittance and conductivity are the key aspects of a good TCE. A figure of merit is often used to evaluate the performance of a transparent conductive film [2, 3, 4]. A common example is the Haccke formula [3]:

$$\phi_{TC} = T^{10} / R_{sheet}$$

where ϕ_{TC} is the figure of merit, T is optical transmittance, and R_{sheet} is sheet resistance [3]. Besides transmission and conductivity, some other properties of TCEs are also taken into consideration for a specific application, such as photovoltaics [4]. These properties include environmental stability, mechanical properties (stretchable and bendable), and the cost. Therefore, there are still demands for different type of transparent conductive materials as shown in **Figure 1.1**. They are also candidate for replacing the ITO as its cost is getting higher and higher. Some of the examples are non-indium transparent conductive oxides (TCOs) [5], ultrathin metals [6], nanowires [7], conductive polymers, graphene [8], dielectric/metal/dielectric [9], and carbon nanotubes [4].

Due to the increasing cost of indium, researchers over the world have been studying alternative materials to replace or reduce the use of ITO. My research tries to tackle the problem by modifying sputtering deposited films with the assistance of a novel single-beam ion source

invented by my advisor, Dr. Qi Hua Fan at MSU [10]. In the next part of this chapter will be structure of this dissertation.

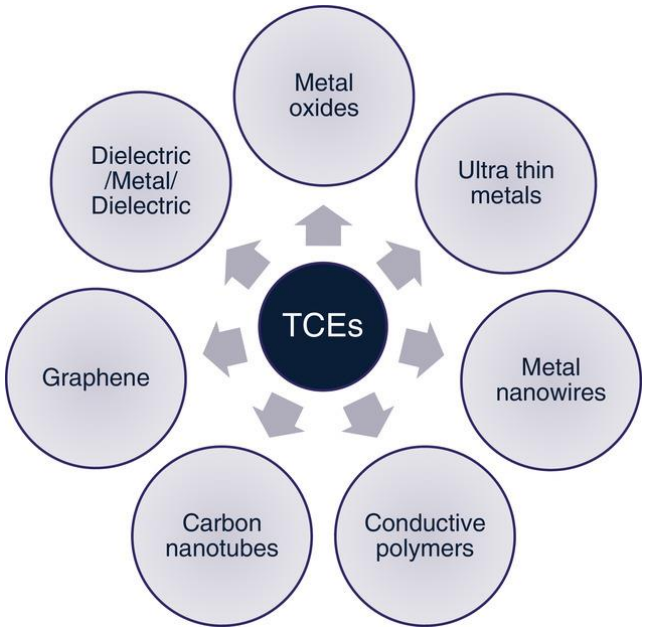

Figure 1.1: Different types of transparent conductive electrodes (TCEs) used for photovoltaics [4]. Reprinted with permission from Willey

1.2 Dissertation Structure

This dissertation encompasses seven chapters, each contributing crucial information within the realm of transparent conductive materials and their advancement:

Chapter 1 serves as an introductory segment, providing a swift insight into transparent conductive materials, elucidating the problem statement, outlining the motivating factors, detailing the chosen methodologies, and summarizing the overall dissertation.

Chapter 2 delves into the essential knowledge pertinent to the experimental methods and characterization tools employed. It meticulously covers the methodologies of RF and DC sputtering, the primary techniques utilized for depositing the studied films. Additionally, this

chapter introduces the Transfer Matrix Method (TMM) as the fundamental means for calculating the optical transmittance and reflectance of designed stacks [11, 12]. Further, it discusses several characterization tools such as scanning electron microscopy (SEM), photo-spectroscopy, 4-point probe, atomic force microscopy (AFM), and x-ray diffraction (XRD) essential for analyzing transparent conductive thin films.

Chapter 3 initiates a study on the ion-beam-assisted deposition of indium tin oxide. Not only does it delineate the positive effects of the ion source on the performance of ITO films, but it also details the structure, operational principles, and characteristics of the utilized ion source.

Chapter 4 sheds light on another significant transparent conductive material: ultra-thin silver, elucidating how ion beams contribute to enhancing its performance. This chapter highlights two pivotal results. Firstly, it demonstrates how the ion beam enhances the wettability of silver films, thereby enabling the successful fabrication of continuous ultra-thin silver films as thin as 6 nm, exhibiting remarkable optical and electrical properties. Secondly, it introduces the integration of a 0.2 nm aluminum cap layer, significantly enhancing the thermal and environmental stability of the resultant continuous ultra-thin silver films.

In Chapter 5, a comprehensive investigation into another transparent conductive electrode, oxide/metal/oxide, is conducted in conjunction with the utilization of the ultra-thin silver films introduced in Chapter 4. Notably, ITO/6-9 nm silver/ITO structures were both computationally optimized and experimentally fabricated. Additionally, the latter part of this chapter encompasses computational studies of other sandwich structures optimized for specific applications. The studies show the promising potential of using sandwich structure to replace ITO in specific applications.

Chapter 6 focuses on the study of ion beam-assisted deposition of tantalum-doped tin oxide (TTO) at room temperature. This material not only has potential to replace ITO as a standalone transparent conductive oxide (TCO), but also holds potential application within the sandwich structure mentioned in Chapter 5.

Lastly, Chapter 7 offers a conclusive segment, summarizing the key findings and paving the way for potential future research endeavors.

REFERENCES

[1] K. Bädeker, "Über die elektrische Leitfähigkeit und die thermoelektrische Kraft," *Ann. Phys.*, vol. 22, pp. 749-766, 1907.

[2] Mazur, M., Kaczmarek, D., Domaradzki, J., Wojcieszak, D., Song, S., & Placido, F. (2010, October). Influence of thickness on transparency and sheet resistance of ITO thin films. In *The Eighth International Conference on Advanced Semiconductor Devices and Microsystems* (pp. 65-68). IEEE.

[3] Haacke, G. (1976). New figure of merit for transparent conductors. *Journal of Applied physics*, 47(9), 4086-4089.

[4] Anand, A., Islam, M. M., Meitzner, R., Schubert, U. S., & Hoppe, H. (2021). Introduction of a novel figure of merit for the assessment of transparent conductive electrodes in photovoltaics: Exact and approximate form. *Advanced Energy Materials*, 11(26), 2100875.

[5] Pern, F. J., Noufi, R., Li, X., DeHart, C., & To, B. (2008, May). Damp-heat induced degradation of transparent conducting oxides for thin-film solar cells. In *2008 33rd IEEE Photovoltaic Specialists Conference* (pp. 1-6). IEEE.

[6] Zhao, G., Shen, W., Jeong, E., Lee, S. G., Yu, S. M., Bae, T. S., ... & Yun, J. (2018). Ultrathin silver film electrodes with ultralow optical and electrical losses for flexible organic photovoltaics. *ACS applied materials & interfaces*, 10(32), 27510-27520.

[7] Sohn, H., Park, C., Oh, J. M., Kang, S. W., & Kim, M. J. (2019). Silver nanowire networks: Mechano-electric properties and applications. *Materials*, 12(16), 2526.

[8] Lee, D., Lee, H., Ahn, Y., & Lee, Y. (2015). High-performance flexible transparent conductive film based on graphene/AgNW/graphene sandwich structure. *Carbon*, 81, 439-446.

[9] Park, H. J., Park, J. H., Choi, J. I., Lee, J. Y., Chae, J. H., & Kim, D. (2008). Fabrication of transparent conductive films with a sandwich structure composed of ITO/Cu/ITO. *Vacuum*, 83(2), 448-450.

[10] Fan, Q.H., Schuelke, T., Haubold, L. and Petzold, M., Michigan State University MSU and Fraunhofer USA Inc, 2021. *Single beam plasma source*. U.S. Patent 11,049,697.

[11] Byrnes, S. J. (2016). Multilayer optical calculations. *arXiv preprint arXiv*:1603.02720.

[12] Katsidis, C. C., & Siapkas, D. I. (2002). General transfer-matrix method for optical multilayer systems with coherent, partially coherent, and incoherent interference. *Applied optics*, 41(19), 3978-3987.

CHAPTER 2

EXPERIMENTAL METHODS AND THEORY

2.1 Magnetron sputtering

Magnetron sputtering is a type of physical vapor deposition (PVD) method. It is the most widely used technique for thin-film deposition in both research labs and industry, particularly for inorganic materials. There are two main types of sputtering: direct current (DC) and radio frequency (RF) sputtering. In DC sputtering, the target must be conductive, whereas RF sputtering can work with both conductive and non-conductive targets. Pulsed DC sputtering can also be adopted for use with conductive targets. Sputtering yields relatively high-quality films at low temperatures [1, 2, 3, 4, 5]. One key factor that makes magnetron sputtering attractive is its scalability. When compared with other thin-film growth techniques, such as pulsed laser deposition, magnetron sputtering is particularly well-suited for large-area coatings, which have numerous important industrial applications, including glass coatings, photovoltaics, and displays

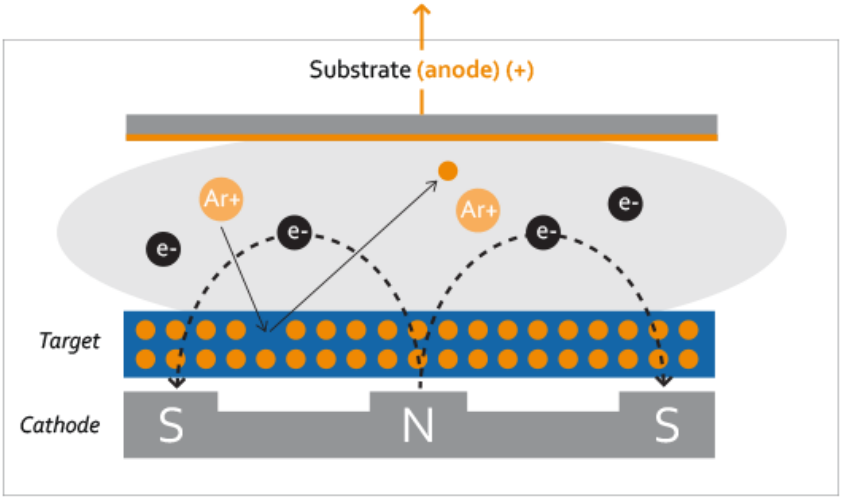

Figure 2.1: Principle of magnetron sputtering - Denton Vacuum

[6, 7]. In a magnetron discharge, electrons are confined by a magnetic field to increase the ion

density near the target and enhance the sputtering rate. The schematic diagram of a magnetron chamber is shown in **Figure 2.1**.

Figure 2.2 displays the Kurt J. Lesker sputtering system located in C.19 of the Plasma Sources and Processing Lab at Michigan State University, which is utilized for research conducted in this dissertation. This system is equipped with a single-beam ion source, SPR-10, manufactured by Scion Plasma LLC.

Figure 2.2: Kurt J. Lesker PVD75 Pro-Line magnetron RF/DC sputtering system at MSU could be equipped with up to five 3-inch magnetrons. One ion source was implemented

During the sputtering process, ionized argon atoms are accelerated by the electric field. Upon colliding with the target surface, they transfer energy to the surface atoms, breaking the bonding. The sputtered atoms then depart from the target and deposit on the substrate. The ratio between the emitted target atoms and incident ions is referred to as the sputtering yield. This value depends on the target's surface binding energy and the energy of incident ions [8].

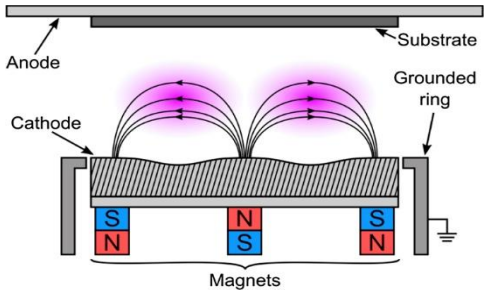

Figure 2.3: A schematic side-view of the planar magnetron sputtering discharge. The cathode target is a cylindrical tube that rotates around the fixed magnet assembly with a frequency of roughly 1 Hz [9]. Reprinted from Gudmundsson and Lundin (2020) permission from Elsevier Science

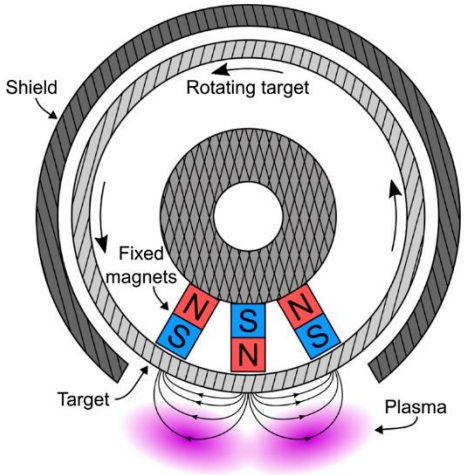

Figure 2.4: A schematic side-view of the rotating magnetron discharge used for sputtering. The magnetic field lines exit the center of the cathode, arch above the target surface, and enter the cathode at the annular [9]. Reprinted from Gudmundsson and Lundin (2020) with permission from Elsevier Science

In a basic system, a planar magnetron discharge, as depicted in **Figure 2.3**, is commonly used [9]. In this set up, only a specific area where electrons are most confined on target is sputtered, resulting in underutilization of the remaining area. To address this issue, alternative setups with a moving target are employed. **Figure 2.4** illustrates a side-view of a rotating magnetron discharge. The cathode target is a cylindrical tube that rotates around a fixed magnet assembly with a frequency of roughly 1 Hz [9]. With this configuration, the target is sputtered evenly. Another setup designed to maximize the utilization of target materials is shown in **Figure 2.5** (b). In this arrangement, a planar target is rotated around an axis near the edge of the plasma ring. This rotation allows for sputtering across a larger surface area of the target.

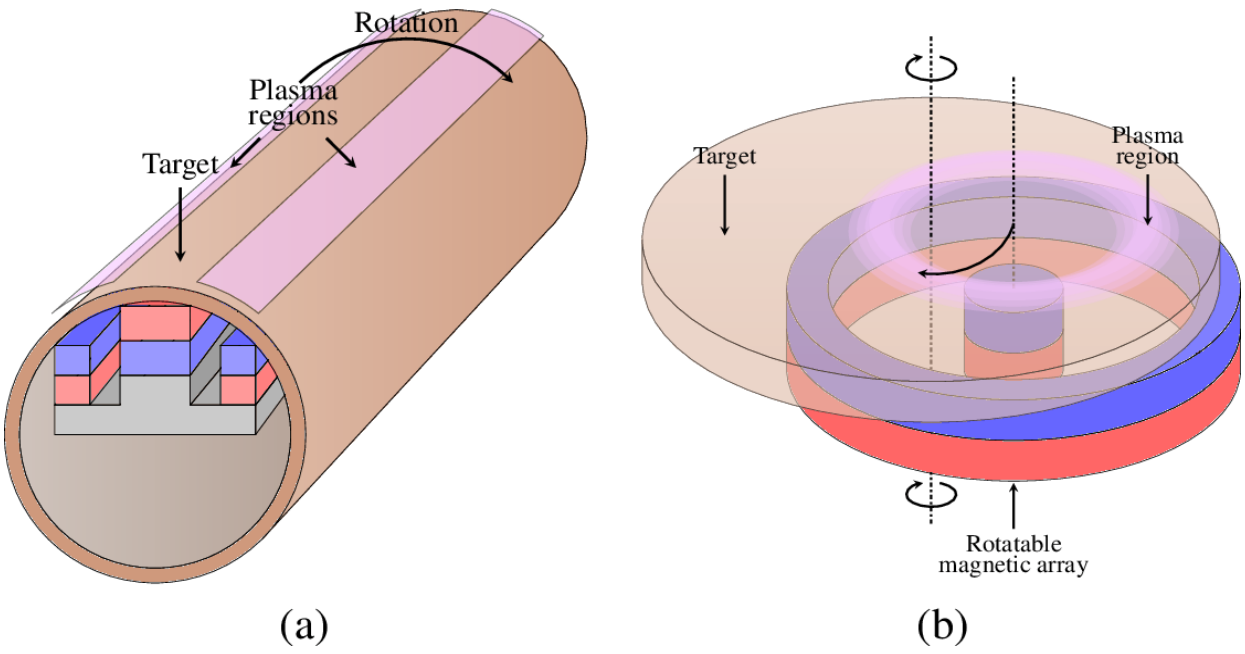

Figure 2.5: Isometric view of rotary targets using rotatable parts in magnetrons for increase in target utilization: (a) cylindrical rotatable magnetron; (b) planar circular magnetron sputtering source with rotatable magnetic array [9]. Reprinted from Gudmundsson and Lundin (2020) with permission from Elsevier Science

2.2 Ion-Beam Assisted Deposition

Ion sources are devices for plasma generation that emit ion beams to interact with the atoms as they are deposited on a substrate, subsequently modulating the microstructures of the film. Ion sources can be combined with a sputtering magnetron to modulate the discharge characteristics and enhance plasma density. Thin films deposited with ion beam assistance tend to exhibit higher density and improved stability [10]. The ion source used in this research was developed by Dr. Fan at MSU [11]. This ion source ionizes gases in the chamber and emit it at a desired energy. For example, if the processing gas is argon, the ion shot out of the ion source will be argon cations.

In the deposition process, ions can collide with sputtering atoms and transfer energy to them. **Figure 2.6** illustrates the effect of the energy of incoming atoms in the deposition process on the crystallization of deposited films [12]. Zone 1 corresponds to low adatom mobility, resulting in the continued nucleation of grains. This leads to a fine-grained structure with textured and fibrous grains, or even an amorphous structure. The crystallinity of films increases as the zone level rises. As shown in the T^* axis, a higher generalized temperature results in reaching a higher zone. The E^* axis illustrates that adding energy to incoming atoms can reduce

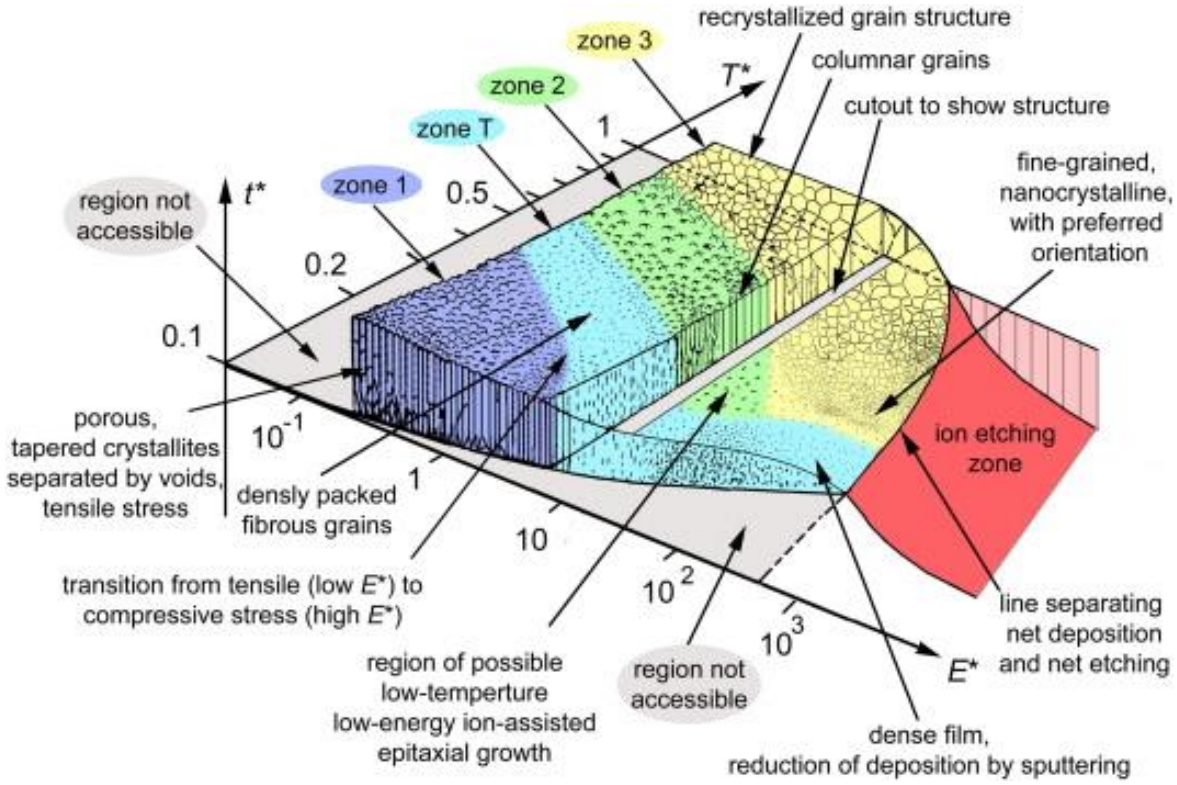

Figure 2.6: Structure zone diagram applicable to energetic deposition; the generalized temperature T∗, the normalized energy flux E∗, and t∗ represents the net thickness. The boundaries between zones are gradual and for illustration only. The numbers on the axes are for orientation only — the actual values depend on the material and many other conditions and therefore the reader should avoid reading specific values or predictions [12]. Reprinted with permission from Elsevier

processing temperature while achieving the same crystallinity. This study aims to enhance the crystallinity of deposited films at low temperatures with the assistance of an ion source. However, it is essential to note that at high value of E^*, sputtering can occur, which is detrimental to deposited films. Therefore, controlling the energy of incoming atoms is crucial. The ion source used in this research can operate within a wide range of discharge voltage setting from 50 V to 250 V, making it suitable to prevent sputtering of the deposited films.

2.3 Thin Film Nucleation and Growth

Thin film growth occurs through a series of processes, including atom adsorption, surface diffusion of atoms, chemical bond formation, nucleation, and grain growth. Similar to crystal growth in bulk structures, thin-film growth on a surface also necessitates nucleation, and the actual growth takes place once a critical size is attained. **Figure 2.7** illustrates the three main modes of thin film growth [13].

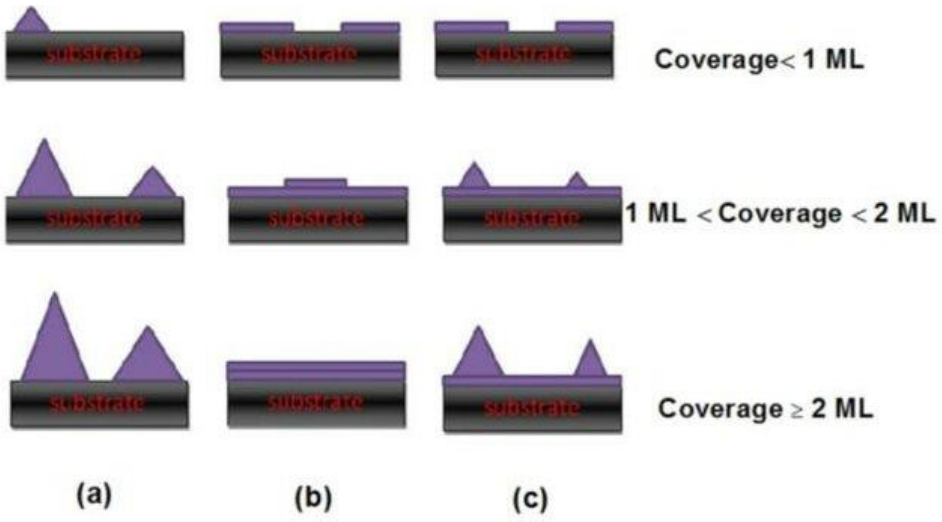

Figure 2.7: Three main thin film growth modes: (a) Volmer-Weber (island formation), (b) Frank-van der Merwe (layer-by-layer), and (c) Stranski-Krastanov (layer-plus-island). Reprinted with permission from WILEY [13]

Volmer-Weber (Island Growth): In island growth, thin films begin to form as isolated islands or clusters on the substrate. Initially, these islands are separated from each other. As more material is deposited, these islands grow and coalesce, eventually forming a continuous thin film. This mode is often observed in certain epitaxial growth processes.

Frank-van der Merwe (Layer-by-Layer Growth): Layer-by-layer growth is characterized by the deposition of material in a controlled, one-layer-at-a-time fashion. Each atomic or molecular layer is deposited evenly across the substrate's surface, resulting in well-defined, uniform layers. Atomic Layer Deposition (ALD) is a prime example of a technique that follows layer-by-layer growth.

Stranski-Krastanov (Mixed Growth): Mixed growth combines features of both island and layer-by-layer growth. It can occur when there is a balance between the formation of islands and the deposition of material layer by layer. The final thin film may exhibit characteristics of both growth modes, making it a versatile approach in certain applications.

The growth mode determines the morphology, crystallography, and therefore, the properties of growth films. Consequently, understanding and knowing how to control growing mode is essential for thin films deposition.

Figure 2.8 presents three main forces affecting the wettability of materials at an interface. It is important to note that this is a thermodynamic calculation. In real cases, processes take time, and therefore, kinetics must be considered.

Balancing the forces in the diagram gives the equation of equilibrium:

$$\cos(\Theta) = \frac{\gamma_{SA} - \gamma_{SB}}{\gamma_{SB}}$$

From this equation, we can derive the conditions for different growth modes shown in **Figure 2.7** as following:

- If $\gamma_{SA} \geq \gamma_{SB} + \gamma_{AB}$, the growth mode is possibly layer by layer or Frank- van der Merve.
- If $\gamma_{SA} < \gamma_{SB} + \gamma_{AB}$, the growth mode is island formation or Volmer – Weber.
- In the case $\gamma_{SA} \geq \gamma_{SB} + \gamma_{AB}$, the growth mode can be layer-plus-island mode or Stranski-Krastanov mode. This occurs due to the strain developed during deposition process, which leads to the variation of surface tensions.

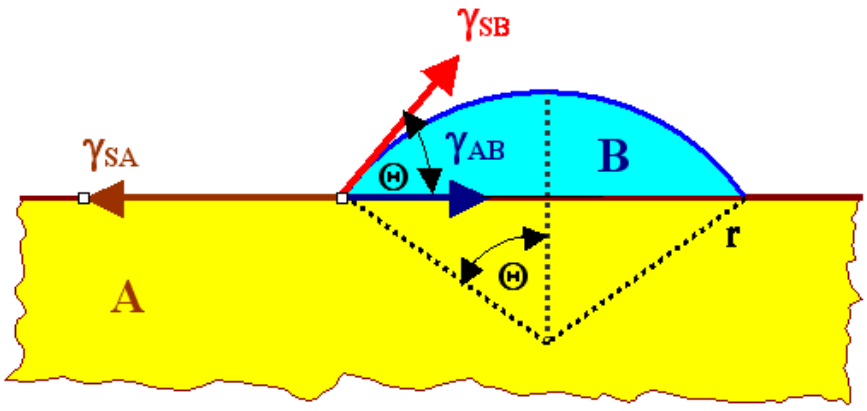

Figure 2.8: Diagram of surface tension and corresponding wetting angle

In most cases, the layer-by-layer growth mode is preferred because it can produce dense and continuous films. In contrast, the island growth mode often leads to porous and discontinuous films, as seen in the case of ultrathin silver films [14]. To control the growth mode of thin films, surface modifications can be employed, such as changing the roughness of the substrate surface and adding a wetting layer of intermediate materials [15]. The growth mode and growth kinetics not only affect the film density but also influence the film roughness, consequently impacting the electrical and optical properties of the thin film.

2.4 Optical Design - Transfer Matrix Method

Propagation of a light ray through a single layer of TCEs shows an infinite series of transmittance and reflectance (**Figure 2.9**). The situation becomes much more complicated when additional layers of materials are introduced. The Transfer Matrix Method (TMM) provides a straightforward means of obtaining exact solutions for the transmittance, reflectance, and absorbance of single or multilayer thin films [16]. In this method, light propagation is viewed in a holistic perspective through the multiplications of refraction matrices or transmission matrices Ds and propagation matrices Ps.

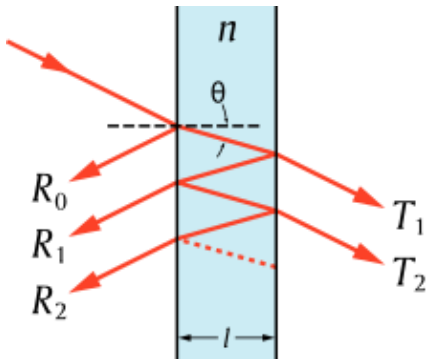

Figure 2.9: Light propagation through a single thin film

The mathematical denotation for the light transmission in a stack of N layers is expressed as following:

$$\begin{pmatrix} E_0^+ \\ E_0^- \end{pmatrix} = D_0^{-1} \left[\prod_{m-1}^{N} D_m P_m D_m^{-1} \right] D_{N+1} \begin{pmatrix} E_{N+1}'^+ \\ E_{N+1}'^+ \end{pmatrix} = \begin{bmatrix} T_{11} & T_{12} \\ T_{21} & T_{22} \end{bmatrix} \begin{pmatrix} E_{N+1}'^+ \\ E_{N+1}'^- \end{pmatrix}$$

Where plus (+) and (-) signs show the direction of the electric waves to the right or to the left of the picture and the prime show the side of the interface in a medium (prime denotes the left side). E_i denotes tangential electric field at the ith medium, N denotes the number of layers in

the optical structure. D denotes the dynamical matrix at a side of interface [16] and $\begin{bmatrix} T_{11} & T_{12} \\ T_{21} & T_{22} \end{bmatrix}$ denotes the system transfer matrix, which is the product of all listed matrixes. Product of two dynamical matrixes at two sides of an interface are defined as following:

$$D_{m-1}^{-1} D_m = \frac{1}{t_{m-1,m}} \begin{bmatrix} 1 & r_{m-1,m} \\ r_{m-1,m} & 1 \end{bmatrix}$$

With $t_{m-1,m}$ and $r_{m-1,m}$ are the Fresnel transmission and reflection. P_m is called propagation matrix dealing with the changing of electric field transferring inside the medium *m*.

$$P_m = \begin{bmatrix} \exp(i\delta_m) & 0 \\ 0 & \exp(-i\delta_m) \end{bmatrix}$$

With $\delta_m = 2\pi\sigma n_m d_m$ with σ is the wavenumber, n_m and d_m are the refractive index and thickness of the m[th] medium, respectively. The product matrix $D_{m-1}^{-1} D_m$ is called refraction or transmission matrix. From equation 3, we can have the overall transmittance and reflectance as following:

$$r = r_{0,N+1} = \left. \frac{E_0^-}{E_0^+} \right|_{E_{N+1}'^- = 0} = \frac{T_{21}}{T_{11}}$$

$$t = t_{0,N+1} = \left. \frac{E_{N+1}'^+}{E_0^+} \right|_{E_{N+1}'^- = 0} = \frac{1}{T_{11}}$$

Table 2.1 shows the list of materials used in my research and the reference for reflective index used in my calculations. To execute the calculation, I use tmm Python package with the inputs are reflective index and design of stacks [17].

Table 2.1: Refractive index used in my calculations

Material	***Reference for reflective index***
ITO	König et al. 2014 [18]
Ag	Rakić et al. 1998: Brendel-Bormann model [19]
Silica fused glass	Malitson et al. 1965 [20] Tan et al. 1998 [21]
SnO_2	Salman et al. 2018 [22]
TiO_2	Sarkar et al. 2019 [23]
AZO	Treharne et al. 2011 [24]

2.5 Thin Film Characterization

2.5.1 Thickness measurement

Film thickness can be measured at a step using a profilometer. Stylus profilometers use a probe to detect the surface, physically moving a probe along the surface in order to acquire the surface height (**Figure 2.10**). This is done mechanically with a feedback loop that monitors the force from the sample pushing up against the probe as it scans along the surface. A feedback system is used to keep the arm with a specific amount of torque on it, known as the 'setpoint'. The solenoid shown in **Figure 2.10** has a cylindrical recess to allow free space for a small permanent magnet attached to the end of the stylus shaft [25]. The solenoid applies a counter force to tune the stylus rotation and to raise and lower the stylus tip according to the current controlled flowing through the solenoid. The changes in the Z position of the arm holder can then be used to reconstruct the surface.

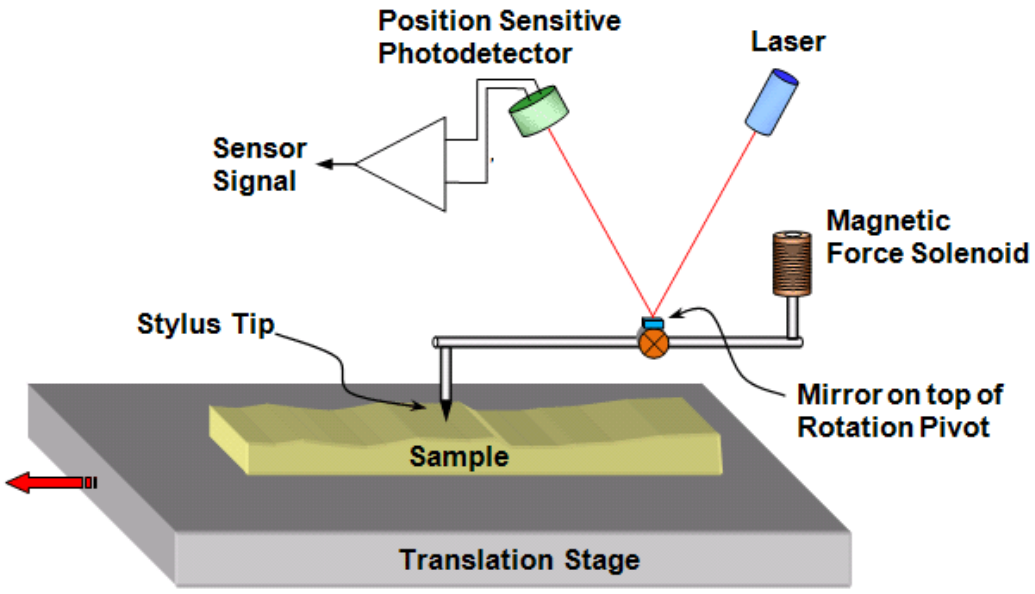

Figure 2.10: Basic element of a stylus profilometer

Stylus profilometry requires force feedback and physically touching the surface, so while it is extremely sensitive and provides high Z resolution, it is sensitive to soft surfaces and the probe can become contaminated by the surface. This technique can also be destructive to some surfaces.

Figure 2.11 shows a picture of a DektakXT stylus profilometer system and **Figure 2.12** illustrates an example of a measurement to measure a step profile formed by deposited materials and substrate. A stylus profilometer can provide information about roughness of surface as well. Because a stylus profilometer involves physical movements in X, Y and Z while maintaining contact with the surface, it is slower than non-contact techniques. The stylus tip size and shape can influence the measurements and limit the lateral resolution. Besides stylus profilometer,

Figure 2.11: DektakXT stylus profilometer at Fraunhofer USA Center Midwest, East Lansing

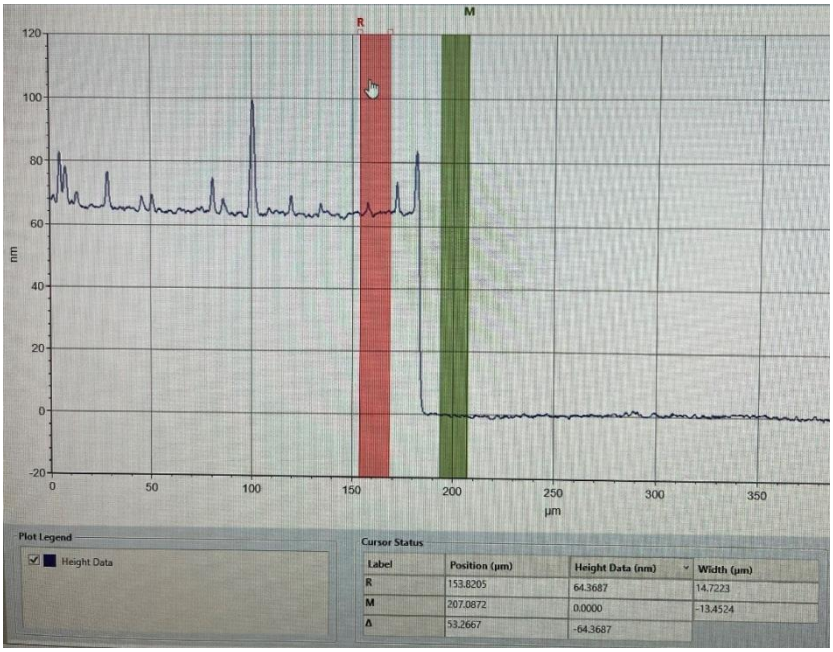

Figure 2.12: Screen capture of a random thickness measurement using the Bruker DektakXT® stylus profilometer. The step profile shown is formed after removing the ink mark

there are many other options to get thickness of thin film such as ellipsometry and grazing incidence X-ray reflectivity.

2.5.2 Electrical Conductivity

Electrical conductivity is a fundamental property of TCEs. To evaluate the electrical performance of thin film in optoelectronic applications, we use sheet resistance, defined as the resistance of a square piece of thin material with contacts made to two opposite sides of the square, assuming the thickness of the film (t) is much less than the length of the square (L) (**Figure 2.13**).

$$R_s = R_{A-B}$$

To calculate R_{A-B} , we follow the formula for bulk material:

$$R_{A-B} = \rho \times \frac{L}{W \times t}$$

In the case of sheet resistance, L=W. Therefore, we have the formula of sheet resistance as following:

$$R_s = R_{A-B} = \frac{\rho}{t}$$

This formula indicates that in the ideal case, sheet resistance is inversely proportional to the thickness t of the film.

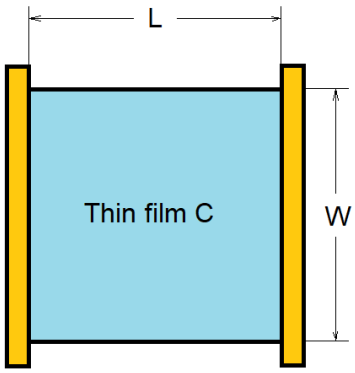

Figure 2.13: Sheet resistance of a thin film C is the resistance between the two electrodes when L and W has the same length and L is much larger than the thickness of the film

In semiconductors, electrical conductivity is the result of the charge of the main electric charge carrier, the concentrations of the main carrier (electron and/or hole), and the mobility of these carriers. **Figure 2.14** displays the electron density and electron mobility of typical materials and their conductivity lines. In the case of ITO, tin is an excellent dopant for indium oxide not only because it has one more valence electron than indium and the atom's diameter is slightly smaller than indium making it perfectly fit into the position of indium in the lattice structure, but also because this free electron comes from s orbital, not from d orbital as in many other metals. Free electrons from s-electron oxides have less effective mass than d-electron oxides [26, 27]. This leads to higher mobility of s-electron oxides as electron mobility is inversely proportional to effective mass as shown in the following equation:

$$\mu_e = e \times \frac{t_s}{m_e^*}$$

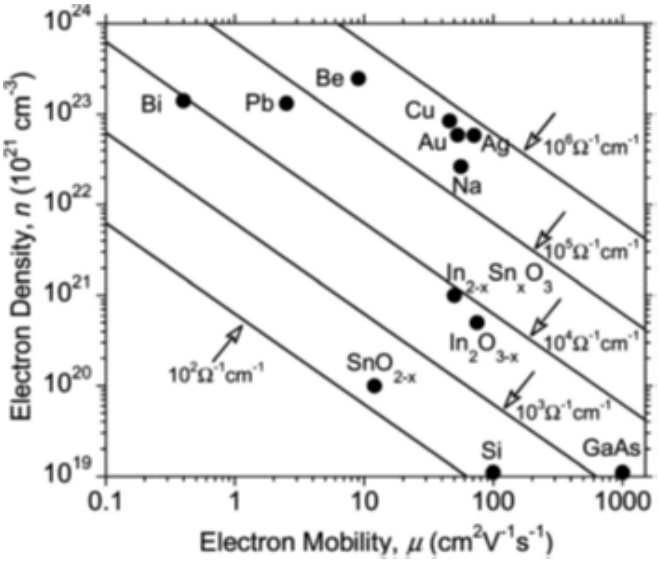

Figure 2.14: Electrical properties of some metals, semiconductors, and metal oxides. Reprinted from Sebastian [26] with permission from Royal Society of Chemistry

where μ_e is electron mobility, e is electron's charge, t_s is average scattering time, and m_e^* is electron's effective mass.

The electrical conductivity of an n-type semiconductor oxide is calculated as in following equation:

$$\sigma = en_e\mu_e$$

where σ is conductivity, e is electron's charge, n_e is concentration of free electron, and μ_e is free electron mobility.

A 4-point probe is often used to measure the sheet resistance and a Hall effect instrument can be used to characterize the carrier concentration and mobility of TCEs thin films. In the 4-point probe method, sheet resistance in the ideal case is calculated as the following equation:

$$R_S = \frac{\pi}{ln\,(2)}\frac{\Delta V}{I}$$

where ΔV is the potential difference between two inner needles, I is the current provided by the two outer needles (**Figure 2.15**) [28].

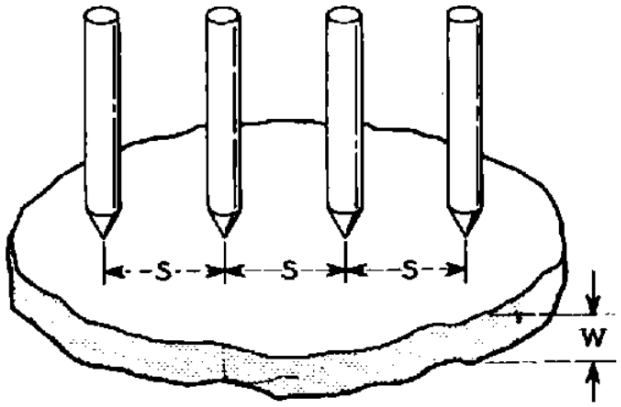

Figure 2.15: Schematic diagram of 4-point probe method

In this method, the ideal case is that the distances between adjacent needles are the same and much larger than the thickness of the film (w<<s). In addition, the distance between needles

is much smaller than the size of the film. Depending on the shape and size of the film, the above equation can be modified by adding a geometry factor. Resistivity, ρ, of the materials can be derived by multiplying sheet resistance, R_S, with the thickness, t, of the film as the following equation:

$$\rho = R_S \times t$$

Figure 2.16 shows a 4-point probe sheet resistivity meter used for measuring sheet resistance of TCE films in this dissertation.

Another technique to get electrical properties of semiconductors is Hall effect

Figure 2.16: SRM-232-100, Guardian Manufacturing, four-point probe sheet resistivity meter

measurement. This method can determine the sign of the main charge carriers, carrier concentration, and carrier mobility. Concentration of electron, n, and mobility of electron, μ_e, can be calculated by following equations:

$$n = \frac{1}{e\ R_H}$$

$$\mu_e = \sigma \times R_H$$

where R_H is the Hall coefficient determined by the Hall measurement as following equation:

$$R_H = \frac{E_y}{j_x \times B_z}$$

In the above equation, E_y is the electric field produced by charges accumulated at the edge of the sample due to the Lorentz force, j_x is the current density produced by the system at steady state, and B_z is the magnetic field generated by the system. J_x, E_y, and B_z are perpendicular to each other in x-, y-, and z-direction, respectively. **Figure 2.17** presents the hall measurement system used to get sheet resistance as well as carrier concentration and mobility of films in this dissertation.

2.5.3 Optical properties-UV–Vis spectroscopy

Transmittance is another important property of TCEs. The optical band gap of a thin films having direct-band gap is related to the absorption coefficient via the Tauc relation:

Figure 2.17: MeasureReady™ FastHall™ Station

$$\alpha hv = A\left(hv - E_g\right)^{1/2}$$

where α is absorption coefficient ($\alpha = -\frac{1}{d}\ln(T)$), T is the optical transmittance, hv is the photon energy, and A is an optical constant [29]. Transmittance or reflectance of TCEs is measured by UV-Vis spectrophotometer . This method measures the transmittance or reflectance of TCEs thin film in the wavelength range of roughly 200 nm to 2000 nm of the light spectrum.

Figure 2.18 illustrates the schematic diagram of a UV-Vis spectrophotometer. It incorporates a white light source filtered through a slit. The light beam disperses into different wavelengths as it passes through a dispersive element. Subsequently, the exit slit scans through the spectrum of the dispersed light to record the light intensity at each wavelength after passing

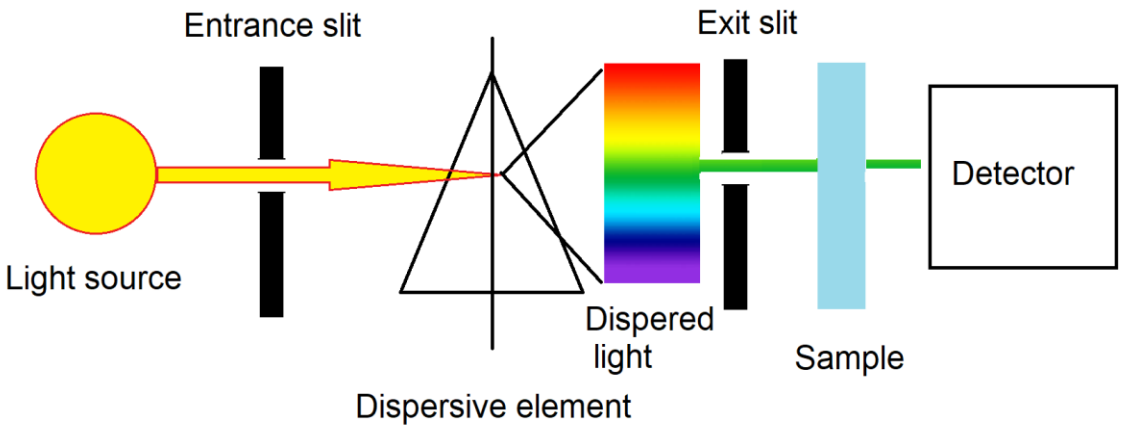

Figure 2.18: Schematic diagram of a single beam UV-Vis Spectrometer

through the sample. The signal is then compared with the scan obtained when there is no sample in between, allowing for determination of the transmittance spectrum of the sample.

A noticeable feature is the fluctuation of transmittance caused by interference which is common in thin films. A common practice is to evaluate the transmittance of ITO by measuring the peak at around 550 nm or taking the average transmittance in the range of visible light. ITO thin film

of ideal quality can have a transmittance of ~90%. **Figure 2.19** shows the spectroscopy system used to get transmittance and reflectance of TCE films in this dissertation.

In optical measurement of thin films, the effect of substrate is inevitable. For getting the transmittance, we can reference air or the substrate as the based transmittance. In the case of using the bare substrate, the transmittance is called optical transmittance. **Figure 2.20** shows the transmittance and reflectance spectra of borosilicate glass substrate used in this work.

Figure 2.19: UV-Vis F20 Spectroscopy

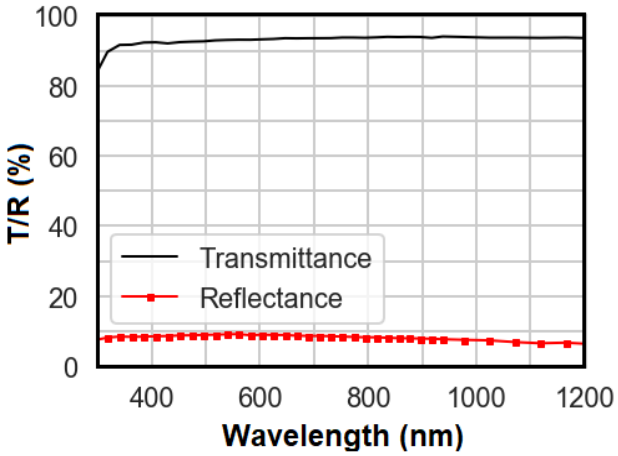

Figure 2.20: Optical properties of borosilicate glass substrate used in this research

2.5.4 Microstructure Characterization

The microstructure of TCE thin films is directly related to the growth conditions and determines the film properties, such as electrical conductivity and transmittance. XRD, SEM, and AFM are used to the microstructures of TCEs. From XRD measurement, we can define crystallization, grain size, and growth direction. From SEM and AFM, we can define the morphology of thin films such as crystal size and roughness. These methods cross-check each other and fortify the structure analysis results of TCEs thin films.

2.5.4.1 X-ray Diffraction

X-ray Diffraction (XRD) is a powerful analytical technique used in materials science and crystallography to determine the atomic and molecular structure of a wide range of materials, including crystalline solids, powders, and thin films. It relies on the interaction of X-rays with a crystalline sample. When X-rays strike a crystal, they are scattered as shown in **Figure 2.21** by

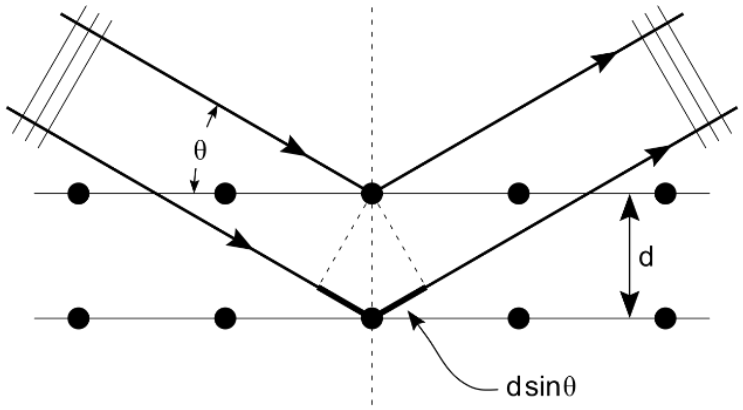

Figure 2.21: Interaction of X-ray with atoms in a crystal structure

the crystal's atomic arrangement in a manner that forms a distinctive diffraction pattern known as finger prints of crystals. By analyzing this pattern, XRD provides information about the crystal's lattice structure, spacing between atoms or planes, and the types of atoms present. This non-destructive technique is widely employed for material identification, phase analysis, and the study of crystalline imperfections, making it an essential tool in fields such as chemistry, physics, geology, and materials engineering. The needed condition for a diffraction spot to appear is govern by Bragg equation:

$$n\lambda = 2dsin\theta$$

with n is an integer, λ is the wavelength of the x-ray, d is the distance between two diffracting planes, θ is the incident angle.

To use XRD for thin film, glancing angle X-ray diffraction (GAXRD) is a specialized application of X-ray diffraction tailored for the precise analysis of thin films. Unlike conventional XRD, GAXRD involves tilting the sample at a shallow or "glancing" angle to the incident X-ray beam. This technique is particularly valuable for studying thin films because it enhances sensitivity to the near-surface region, where thin films often exhibit unique properties and structures. GAXRD provides insights into the crystallographic orientation, texture, and thickness of thin films, allowing researchers to uncover details about the film's growth, defects, and structural changes at the nanoscale.

The Scherrer equation, named after Paul Scherrer, is a fundamental equation in X-ray and neutron diffraction used to determine the average crystallite size or grain size of crystalline materials. It relates the width of diffraction peaks observed in a diffraction pattern to the size of the crystalline domains within the material. The equation is expressed as follows [30]:

$$\beta \cos(\theta) = \frac{K\lambda}{D}$$

Where:

- β is the full width at half maximum (FWHM) of a diffraction peak in radians.
- θ is the Bragg angle (the angle at which the X-ray or neutron beam strikes the crystal lattice).
- λ is the wavelength of the X-ray or neutron radiation.
- D is the average crystallite size or grain size of the material.
- K is a dimensionless shape factor, often considered to be around 0.9.

The Scherrer equation is a useful tool for researchers in materials science and crystallography. By measuring the FWHM of a diffraction peak and knowing the values of θ, λ, and K, the equation allows for the estimation of the average size of crystalline domains in a

material. This information is valuable for characterizing the structural properties of crystalline materials and is used in a wide range of scientific and industrial applications, including the analysis of metals, ceramics, and minerals.

2.5.4.2 AFM

Atomic Force Microscopy (AFM) operates on the principle of scanning a sharp tip, typically at the end of a flexible cantilever, over the surface of a sample. The tip interacts with the atoms on the sample's surface, creating forces that cause the cantilever to deflect. This deflection is carefully measured using a laser beam directed onto the back of the cantilever, which is reflected onto a position-sensitive photodetector. As the tip scans the surface, maintaining a constant force or distance, the deflections are recorded, and a three-dimensional image is constructed. The remarkable sensitivity of AFM allows researchers to visualize and analyze surfaces at the nanoscale, providing information about the topography, roughness, and even the mechanical properties of materials. The versatility of AFM extends beyond imaging; it can be employed for various modes, such as force spectroscopy, enabling detailed investigations into the interactions and properties of materials at the atomic and molecular levels. The non-destructive nature of AFM makes it an indispensable tool in fields ranging from materials science and biology to physics and nanotechnology.

REFERENCES

[1] Gehman, B. L., Jonsson, S., Rudolph, T., Scherer, M., Weigert, M., & Werner, R. (1992). Influence of manufacturing process of indium tin oxide sputtering targets on sputtering behavior. *Thin Solid Films*, *220*(1-2), 333-336.

[2] Gwamuri, J., Marikkannan, M., Mayandi, J., Bowen, P. K., & Pearce, J. M. (2016). Influence of oxygen concentration on the performance of ultra-thin RF magnetron sputter deposited indium tin oxide films as a top electrode for photovoltaic devices. *Materials*, *9*(1), 63.

[3] Kelly, P. J., & Arnell, R. D. (2000). Magnetron sputtering: a review of recent developments and applications. *Vacuum*, *56*(3), 159-172.

[4] Liu, C., Matsutani, T., Yamamoto, N., & Kiuchi, M. (2002). High-quality indium tin oxide films prepared at room temperature by oxygen ion beam assisted deposition. *Europhysics Letters*, *59*(4), 606.

[5] Gehman, B. L., Jonsson, S., Rudolph, T., Scherer, M., Weigert, M., & Werner, R. (1992). Influence of manufacturing process of indium tin oxide sputtering targets on sputtering behavior. *Thin Solid Films*, *220*(1-2), 333-336.

[6] Sierros, K. A., Cairns, D. R., Abell, J. S., & Kukureka, S. N. (2010). Pulsed laser deposition of indium tin oxide films on flexible polyethylene naphthalate display substrates at room temperature. *Thin Solid Films*, *518*(10), 2623-2627.

[7] Adurodija, F. O., Izumi, H., Ishihara, T., Yoshioka, H., Matsui, H., & Motoyama, M. (1999). Pulsed laser deposition of low-resistivity indium tin oxide thin films at low substrate temperature. *Japanese journal of applied physics*, *38*(5R), 2710.

[8] Seah, M. P. (2013). Universal equation for argon gas cluster sputtering yields. *The Journal of Physical Chemistry C*, *117*(24), 12622-12632.

[9] Gudmundsson, J. T. and Lundin, D., "Introduction to magnetron sputtering," in *High Power Impulse Mangetron Sputtering: Fundamentals, Technologies, Challenges and Applications*, vol. 29, Amsterdam, Elsevier, 2020, p. pp1–48.

[10] Martin, P. J., MacLeod, H. A., Netterfield, R. P., Pacey, C. G., & Sainty, W. G. (1983). Ion-beam-assisted deposition of thin films. *Applied Optics*, *22*(1), 178-184.

[11] Fan, Q. H., Schuelke, T., Haubold, L., & Petzold, M. (2021). *U.S. Patent No. 11,049,697*. Washington, DC: U.S. Patent and Trademark Office.

[12] Anders, A. (2010). A structure zone diagram including plasma-based deposition and ion etching. *Thin Solid Films*, *518*(15), 4087-4090.

[13] Kim, G., Kim, D., Choi, Y., Ghorai, A., Park, G., & Jeong, U. (2023). New approaches to produce large-area single crystal thin films. *Advanced Materials*, *35*(4), 2203373.

[14] Gu, D., Zhang, C., Wu, Y. K., & Guo, L. J. (2014). Ultrasmooth and thermally stable silver-based thin films with subnanometer roughness by aluminum doping. *Acs Nano*, *8*(10), 10343-10351.

[15] Jothi Prakash, C. G., & Prasanth, R. (2021). Approaches to design a surface with tunable wettability: a review on surface properties. *Journal of Materials Science*, *56*, 108-135.

[16] Katsidis, C. C., & Siapkas, D. I. (2002). General transfer-matrix method for optical multilayer systems with coherent, partially coherent, and incoherent interference. *Applied optics*, *41*(19), 3978-3987.

[17] Byrnes, S. J. (2016). Multilayer optical calculations. *arXiv preprint arXiv:1603.02720*.

[18] Konig, T. A., Ledin, P. A., Kerszulis, J., Mahmoud, M. A., El-Sayed, M. A., Reynolds, J. R., & Tsukruk, V. V. (2014). Electrically tunable plasmonic behavior of nanocube–polymer nanomaterials induced by a redox-active electrochromic polymer. *ACS nano*, *8*(6), 6182-6192.

[19] Rakić, A. D., Djurišić, A. B., Elazar, J. M., & Majewski, M. L. (1998). Optical properties of metallic films for vertical-cavity optoelectronic devices. *Applied optics*, *37*(22), 5271-5283.

[20] Malitson, I. H. (1965). Interspecimen comparison of the refractive index of fused silica. *Josa*, *55*(10), 1205-1209.

[21] Tan, C. Z. (1998). Determination of refractive index of silica glass for infrared wavelengths by IR spectroscopy. *Journal of Non-Crystalline Solids*, *223*(1-2), 158-163.

[22] Manzoor, S., Häusele, J., Bush, K. A., Palmstrom, A. F., Carpenter, J., Zhengshan, J. Y., ... & Holman, Z. C. (2018). Optical modeling of wide-bandgap perovskite and perovskite/silicon tandem solar cells using complex refractive indices for arbitrary-bandgap perovskite absorbers. *Optics express*, *26*(21), 27441-27460.

[23] Sarkar, S., Gupta, V., Kumar, M., Schubert, J., Probst, P. T., Joseph, J., & König, T. A. (2019). Hybridized guided-mode resonances via colloidal plasmonic self-assembled grating. *ACS applied materials & interfaces*, *11*(14), 13752-13760.

[24] Treharne, R. E., Seymour-Pierce, A., Durose, K., Hutchings, K., Roncallo, S., & Lane, D. (2011, March). Optical design and fabrication of fully sputtered CdTe/CdS solar cells. In *Journal of Physics: Conference Series* (Vol. 286, No. 1, p. 012038). IOP Publishing.

[25] [Online]. Available: https://australiasurfacemetrologylab.org/new-page.

[26] David, S. P., Soosaimanickam, A., Sakthivel, T., Sambandam, B., & Sivaramalingam, A. (2020). Thin Film Metal Oxides for Displays and Other Optoelectronic Applications. *Metal and Metal Oxides for Energy and Electronics*, *55*, 185.

[27] Dixon, S. C., Scanlon, D. O., Carmalt, C. J., & Parkin, I. P. (2016). n-Type doped transparent conducting binary oxides: an overview. *Journal of Materials Chemistry C*, *4*(29), 6946-6961.

[28] F. M. Smits, "Measurements of Sheet Resistivity with the Four-Point Probe," *The Bell System Technical Journal*, vol. 37, no. 3, pp. 711-718, 1958.

[29] Zhang, L., Lan, J., Yang, J., Guo, S., Peng, J., Zhang, L., ... & Xie, W. (2017). Study on the physical properties of indium tin oxide thin films deposited by microwave-assisted spray pyrolysis. *Journal of Alloys and Compounds*, *728*, 1338-1345.

[30] Holzwarth, U., & Gibson, N. (2011). The Scherrer equation versus the'Debye-Scherrer equation'. *Nature nanotechnology*, *6*(9), 534-534.

CHAPTER 3

SINGLE-BEAM ION SOURCE ENHANCED GROWTH OF INDIUM TIN OXIDE THIN FILMS

This chapter is adapted from the preprint of Tran, Thanh, Young Kim, Nina Baule, Maheshwar Shrestha, Bocong Zheng, Keliang Wang, Thomas Schuelke, and Qi Hua Fan. "*Single-beam ion source enhanced growth of transparent conductive thin films*." Journal of Physics D: Applied Physics 55, no. 39 (2022): 395202.

3.1 Introduction

Indium tin oxide (ITO) thin films are the primary transparent conductive materials used in a broad variety of applications, such as solar cells, displays, smart windows, and LEDs [1]. ITO thin films are commonly produced by magnetron sputtering and require elevated deposition temperatures (e.g., >200 °C) to achieve satisfactory electric conductivity and optical transmittance. However, many applications involve heat-sensitive materials that limit the thin-film growth temperature. An example is ITO deposition on polyethylene terephthalate (PET) for touch screens, where the process temperature should be below 80 °C. Under low temperatures, ITO thin films have an amorphous microstructure, which leads to high resistivity, low optical

transmittance, and poor stability [2]. Producing polycrystalline ITO thin films under the off-phase equilibrium temperature is a fundamental challenge.

Ion source assisted deposition has the potential to produce high-quality ITO films at low temperatures. Ion sources are plasma generation devices that enable ion beams to interact with the materials at the atomic level as they are deposited to effectively produce dense films with tunable morphology and superior stability [3, 4, 5]. Two major types of ion sources have been widely used for surface treatment – filament and racetrack (anode layer) types [6]. Filament-type ion sources can produce ions with controllable energy over a wide range. Some processes require the use of reactive gases, such as oxygen, which could be detrimental to the filament. Racetrack-type ion sources are compatible with reactive gases. The closed-loop drift of the electrons leads to circular or racetrack beam patterns, while some applications would require the ions to be focused onto a small area. Furthermore, the ion sources used to enhance thin-film growth must be compatible with magnetron discharges and can stably operate over an extended period.

A single beam ion source has been recently developed to address the needs described above. This single beam ion source combines several desired features:

- Focused single beam of ions generated without a filament;
- Widely tunable discharge voltage (e.g., 0 to 250 V) for optimal ion-surface interactions;
- Wide range of operation pressure (1 to 500 mTorr) compatible with magnetron sputtering and chemical vapor deposition in inert and reactive gases; and
- Hidden anode suitable for long-term operation in the thin-film manufacturing environment and easy to maintain.

This paper reports the initial study to validate the basic characteristics of the single beam ion source enhanced magnetron sputtering. The goal is to demonstrate the feasibility of low-temperature high-rate deposition of ITO thin films that have the desired microstructure and properties, which could only be obtained at elevated temperatures in conventional magnetron sputtering.

3.2 Material and Methods

The single-beam ion source used in this study is illustrated in **Figure 3.1** (model SPR-10, Scion Plasma LLC). It consists of an anode with a center cavity and a closed bottom. A cathode cover with a center opening is located above the anode, which is not directly exposed to the atoms sputtered off the magnetron target. A magnetic field is generated by a magnet assembly and forms a closed loop inside the anode cavity to confine the electrons. Details of this single beam plasma source can be found in reference [7].

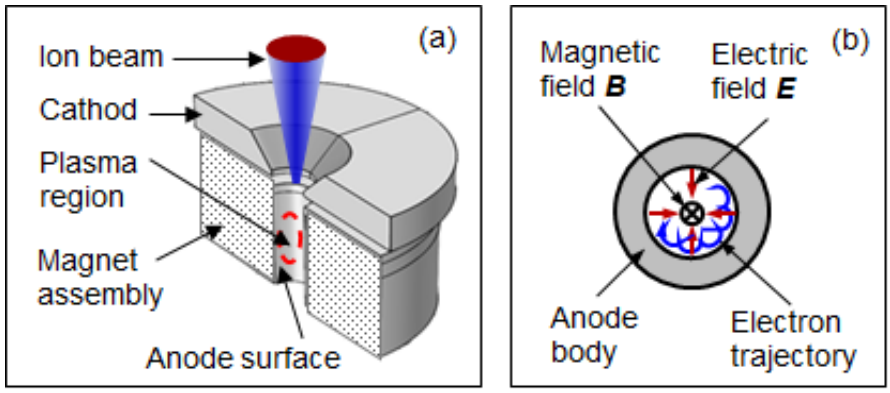

Figure 3.1: (a) Profile size view and (b) top view of the single beam plasma source

A circular magnetron (model TORUS TM3, KJ Lesker) was used for sputtering deposition of ITO thin films. The ITO target was 76.2 mm in diameter and ~3.2 mm in thickness. The target was 99.99% purity with a composition of In_2O_3/SnO_2 = 90/10 wt%. The ion source

and the magnetron were arranged at an angle of 45 degrees with their center lines crossing at the substrate surface (see details in Results).

Before the ITO film deposition, the system was pumped down to a base pressure below 1×10^{-6} Torr. Ar gas mixed with 0.1% oxygen was used in all the depositions. The process pressure was 3 mTorr. All the ITO films were deposited at room temperature. The magnetron sputtering power was 60 W of pulse DC in all the depositions. However, the ITO film deposition rates strongly depended on and increased almost linearly with the voltage of the ion source. Therefore, the deposition time under each ion source voltage was adjusted to produce the ITO films of 100 nm thickness. The substrates were a soda-lime glass of 25 mm×25 mm×0.7 mm.

The film thickness was measured using a Dektak 150 profilometer. The ITO film transmittance was characterized using a spectrophotometer (F20, Filmetics). The sheet resistance was measured using a four-point probe (SRM-232-1000, Guardian Manufacturing). The film microstructure was determined using X-ray diffraction (SmartLab, Rigaku). The surface morphology was characterized using atomic force microscopy (AFM5000, Hitachi).

3.3 Results

The sputtering magnetron and the single beam ion source could be arranged at any angle, such as parallel, 45 degrees, and 90 degrees. Although all these configurations showed similar discharge characteristics, the preferred arrangement is 45 degree or larger angle for focusing the beam on the substrate area. **Figure 3.2** (left) shows a typical discharge image of the magnetron operating simultaneously with the ion source. The magnetron was set at 45 degrees from the ion source in this case. The magnetron and the ion source can be excited by various combinations of power sources. For example, the magnetron can be powered by DC, pulsed DC, or RF, while the ion source can be powered by DC, RF, or DC+RF. The discharges were stable in all these

combinations. In consideration of the practical application, this study used pulse DC to power the magnetron and DC+RF to power the single beam ion source. The RF power was 0-10 W with a maximum peak-peak voltage of ~400 V.

When the single beam plasma source simultaneously operates with a sputtering magnetron, it can discharge over a wide range of voltages, as illustrated in the I-V curve in **Figure 3.2** (right). The DC bias voltage could be varied from 0 V. The ion source current increased almost linearly with the voltage.

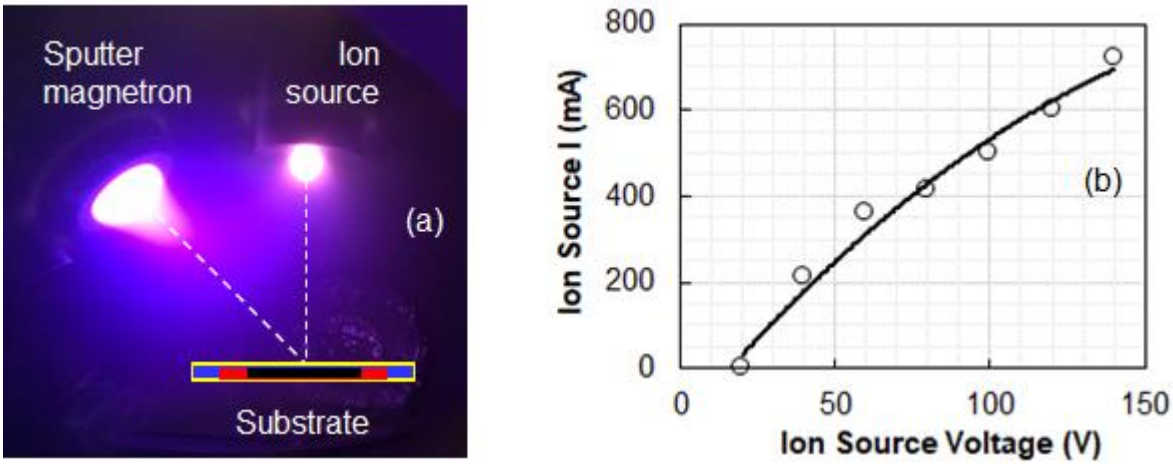

Figure 3.2: (left) Discharge image of the single beam plasma source operating with a sputtering magnetron. The black area in the substrate is the effectively treated region and the blue area is untreated, while the red area is a transition region partially treated. (right) I-V characteristics of the single beam plasma source operating with a magnetron power of 60 W

The single-beam ion source could drastically modulate the magnetron discharge. As the voltage of the ion source increased from 0 to 140 V, the magnetron discharge voltage dropped from 234 V to 138 V, while the magnetron current increased accordingly from 256 mA to 435 mA as illustrated in **Figure 3.3**. Hence, the beam plasma source enables a low-voltage and high-current sputtering mode, marked by the dotted blue line in Figure 3. We call this "soft sputtering mode". In comparison with magnetron sputtering alone (0 V ion source voltage), the "soft sputtering mode" led to over 35% higher deposition rates of ITO films. It is worth noting that the current of the single beam ion source became larger than the magnetron current at an ion source voltage above 40 V. This result indicates that the single beam ion source can "amplify" the current from the magnetron discharge by creating additional electrons and ions. Therefore, the ion source and the magnetron mutually enhance each other.

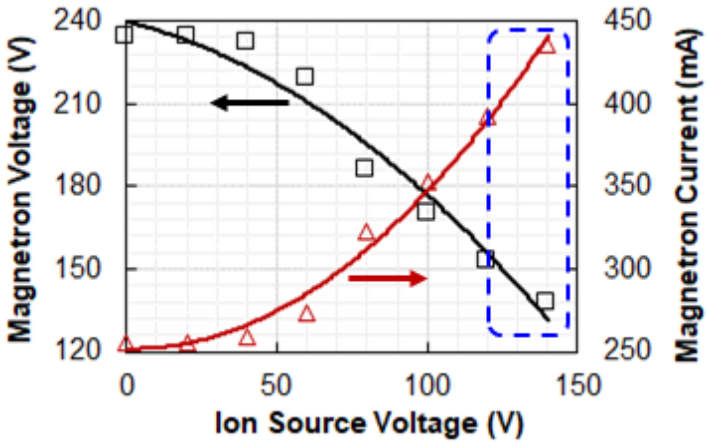

Figure 3.3: Variation of the magnetron current and voltage with the voltage of the ion source

Figure 3.4 shows the sheet resistance of ITO films deposited at different ion source voltages with the magnetron power fixed at 60 W. The ITO film sheet resistance dropped from 118 to 56 Ω/Sq as the ion source voltage increased from 0 to 120 V. Further increasing the ion source voltage led to an increase in the ITO sheet resistance. Therefore, there is an optimum voltage that reflects the proper energy of the ions interacting with the ITO films as they were deposited. It is worth noting that the process conditions were not fully optimized. The results only show one typical set of process parameters (e.g., pressure, oxygen fraction, and magnetron power) with different ion source voltages.

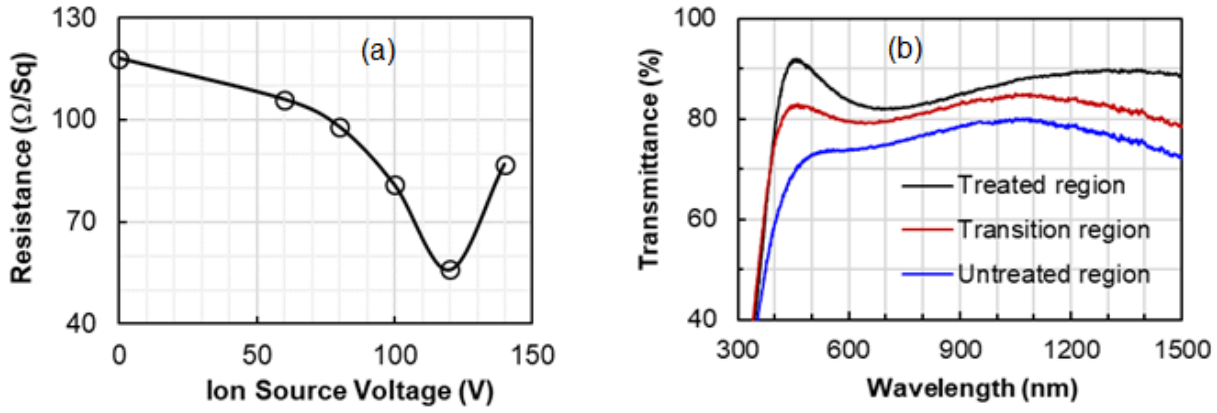

Figure 3.4: (a) Sheet resistance of 100 nm ITO films deposited at different beam plasma source voltages with the same magnetron power. (b) Optical transmittance spectra of ITO films in different regions of the same substrate

The optical transmittance of the ITO film varies with the location on the substrate. The transmittance is the highest in the central region where the ion beam effectively interacts with the film. This center region was about 38 mm in diameter. Away from this region, the transmittance dropped greatly. Therefore, the ion beam "amplified" the effect of oxygen by effectively delivering oxygen species to the film, while the oxygen concentration was still not sufficient without the ion beam treatment. It is worth noting that ITO films with transmittance close to the

ion beam treated region could be made by magnetron sputtering alone if higher concentrations of oxygen were introduced. However, this is usually at the cost of increased resistivity.

Atomic force microscopy (AFM) scanning revealed distinct surface morphologies of the ITO films deposited with and without the ion source treatment, as illustrated in **Figure 3.5**. The ion source led to a much smoother ITO film with a root mean square roughness of Rms = 1.09 nm, while the ITO film deposited with magnetron alone has a roughness of Rms = 2.97 nm.

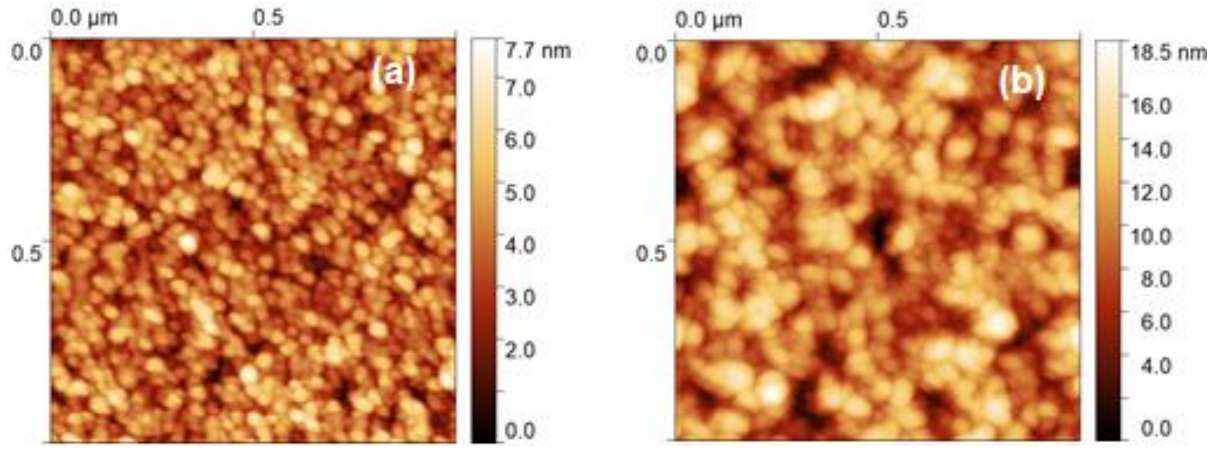

Figure 3.5: AFM images of ITO film deposited by magnetron sputtering with the ion source (a) on (100 V) and (b) off (0 V)

The significant effects of the single beam ion source on the ITO film properties are closely related to the film microstructure. X-ray diffraction patterns shown in **Figure 3.6** indicate that the ion beam led to much improved ITO film crystallinity once the plasma source discharge voltage was above a threshold value (e.g., 100 V). Below this threshold (e.g., 0-80 V), the ITO films appeared to be amorphous. Interestingly, a plasma discharge voltage of 100 V resulted in preferentially oriented crystals, while higher voltages led to random orientations. These effects can be understood in terms of the ion energy delivered to the ITO films as the atoms were

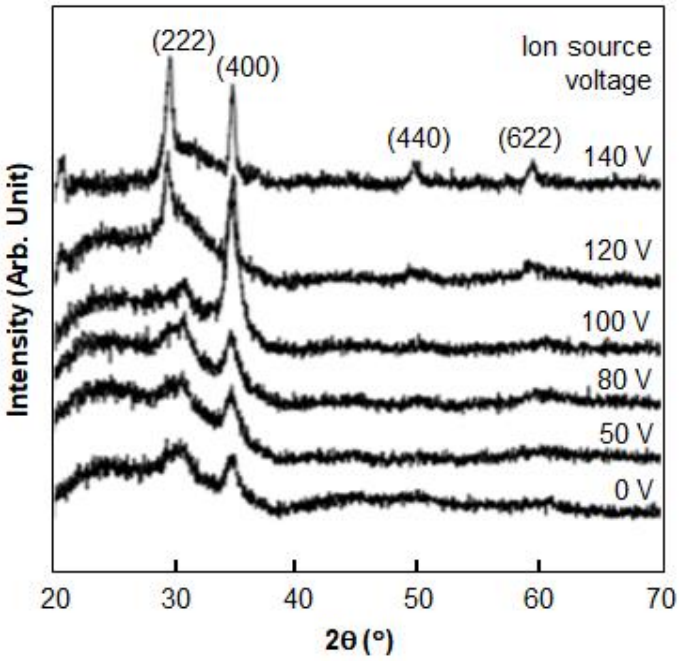

Figure 3.6: X-ray diffraction patterns of ITO films deposited at different beam plasma source voltages

deposited on the substrate. There is optimum ion energy. It is worth noting that all the ITO films were deposited at room temperature, which is expected to yield an amorphous structure.

3.4 Discussion

3.4.1 Beam plasma source enhanced magnetron discharge

The discharge voltage is coupled with the current in conventional magnetron sputtering. This means the voltage and current would increase simultaneously with the excitation of DC power. On the other hand, it has been well recognized that RF sputtering generally results in better film quality than DC. One of the reasons is the DC bias on the cathode (target) during RF discharge is in the range of 100-140 V, which is much lower than the DC discharge voltage which is usually above 250 V. A low discharge voltage eliminates the high-energy tail of the sputtered atoms. According to Thompson's Law [8, 9], a fraction of the sputtered atoms has

energy close to the magnetron discharge potential energy (e.g. 250 eV). These energetic atoms could induce disordered film microstructures and create rough surfaces.

Although a low sputtering voltage is generally preferred, RF sputtering and DC sputtering at low voltages suffer from low deposition rates and are practically difficult to be adopted into coatings manufacturing. The single-beam ion source enhances magnetron discharge, leading to low target voltage and high current sputtering that yields an even higher deposition rate than magnetron sputtering alone. This soft sputtering mode opens a new thin-film deposition regime that has many potential applications. The soft sputtering mode cannot be achieved in conventional DC magnetron discharges.

Previous research has indicated that there is a significant potential drop between the bulk plasma and the substrate in RF discharge, while this potential is negligible in DC magnetron sputtering [10, 11]. Therefore, pronounced ion bombardment to the substrate is expected in RF magnetron sputtering. This is another reason that RF sputtering generally produces better film quality than DC sputtering at low temperatures. However, the potential between the bulk plasma and substrate has little tunability in RF magnetron discharges. On the other hand, the single-beam ion source delivers ions with controllable energy to the film, while it enables a soft sputtering mode on the target side. Hence, it can modulate the film microstructure and properties even at practically high deposition rates and low temperatures.

2.4.2 Electron and ion energies

The energies of the electrons and argon ions created by the single beam plasma source depend on the excitation power source (DC and/or RF) and voltage, as well as the substrate being a conductor or insulator. **Figure 3.7** shows the simulated electron energy probability function (EEPF) and ion energy distribution function (IEDF). The simulation was performed

using an established particle-in-cell Monte Carlo collision code ASTRA. The detail of this simulation scheme is described in previous work [12]. The electron energy probability function includes two regions: inside and outside the anode cavity of the single beam plasma source. The results indicate that higher RF peak voltage and DC bias lead to increased energetic tails that could enhance the plasma density of the magnetron discharge.

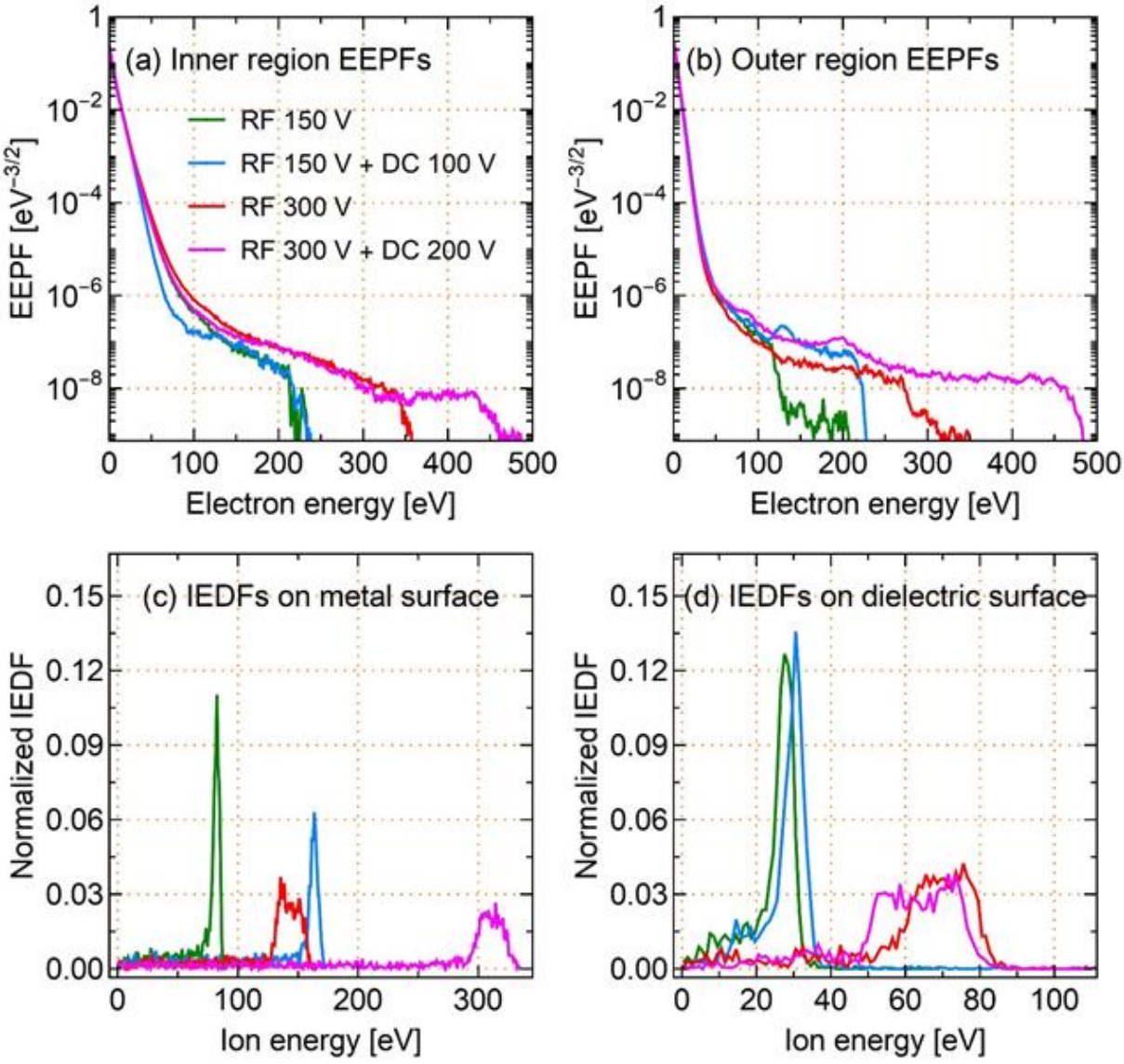

Figure 3.7: (a) and (b): electron energy probability function (EEPF) inside and outside of the anode cavity. (c) and (d): ion energy distribution function (IEDF) on substrates

The ion energy distribution function shows that the ion energy is proportional to the RF and DC voltages on an electrically conductive substrate. Therefore, this result confirms the previous observation (see Figure 4) that there is optimum ion energy that leads to the lowest sheet resistance of the ITO films. On the other hand, the ion energy is much reduced if the substrate is an insulator. In this case, the RF excitation plays an important role in modulating the ion energy.

3.4.3 Scalability of the single beam ion source

This study used a round-shape single-beam ion source that can effectively treat a substrate area about 38 mm in diameter when the source was set at about 76 mm away from the

Figure 3.8: Round and linear (78 mm effective length) single beam plasma sources and discharges

substrate. The single-beam plasma source can be designed into a linear structure of any custom length, as illustrated in **Figure 3.8**, for treating larger areas. It can treat a rectangular area of about 38 mm wide and the effective length of the source.

3.5 Conclusion

This research demonstrates the use of a single beam ion source to enhance magnetron discharge and thin-film growth at low temperatures. The single-beam plasma source enables a soft sputtering mode that features low magnetron discharge voltage and high current, which can potentially produce high-quality thin films without sacrificing the deposition rates. The soft sputtering in combination with ion beam interactions with the film leads to high-rate deposition of ITO films with tunable microstructures. Polycrystalline ITO thin films can be produced at room temperature once the ion energy reaches a threshold value. The single-beam ion source enhanced sputtering leads to greatly reduced ITO film resistivity and surface roughness. The single-beam ion source is scalable to a linear structure of any length for large-area coatings.

REFERENCES

[1] Ginley, D. S., & Perkins, J. D. (2010). Transparent Conductors. In *Handbook of Transparent Conductors* (pp. 1-25). Boston, MA. Springer US.

[2] Addonizio, M. L., Gambale, E., & Antonaia, A. (2020). Microstructure evolution of room-temperature-sputtered ITO films suitable for silicon heterojunction solar cells. *Current Applied Physics*, 20(8), 953-960.

[3] Ren, Z. M., Du, Y. C., Ying, Z. F., Qiu, Y. X., Xiong, X. X., Wu, J. D., & Li, F. M. (1994). Electronic and mechanical properties of carbon nitride films prepared by laser ablation graphite under nitrogen ion beam bombardment. *Applied physics letters*, 65(11), 1361-1363.

[4] Písařík, P., Mikšovský, J., Remsa, J., Zemek, J., Tolde, Z., & Jelínek, M. (2018). Diamond-like carbon prepared by pulsed laser deposition with ion bombardment: physical properties. *Applied Physics A*, 124, 1-9.

[5] Wang, W., Liu, L. F., Yao, Y. J., Lu, S. D., Wu, X., Zheng, T., ... & Li, Y. J. (2018). Growth dynamics controllable deposition of homoepitaxial MgO films on the IBAD-MgO substrates. *Applied Surface Science*, 435, 225-228.

[6] J. Reece Roth (1995). *Industrial Plasma Engineering*, IOP Publishing Ltd.

[7] Fan, Q. H., Schuelke, T., Haubold, L., & Petzold, M. (2021). *U.S. Patent No. 11,049,697*. Washington, DC: U.S. Patent and Trademark Office.

[8] Thompson, M. W. (1968). II. The energy spectrum of ejected atoms during the high energy sputtering of gold. *Philosophical Magazine*, 18(152), 377-414.

[9] Serikov, V. V., & Nanbu, K. (1996). Monte Carlo numerical analysis of target erosion and film growth in a three-dimensional sputtering chamber. *Journal of Vacuum Science & Technology A: Vacuum, Surfaces, and Films*, 14(6), 3108-3123.

[10] Zheng, B., Fu, Y., Wang, K., Schuelke, T., & Fan, Q. H. (2021). Electron dynamics in radio frequency magnetron sputtering argon discharges with a dielectric target. *Plasma Sources Science and Technology*, 30(3), 035019.

[11] Zheng, B., Fu, Y., Wang, K., Tran, T., Schuelke, T., & Fan, Q. H. (2021). Comparison of 1D and 2D particle-in-cell simulations for DC magnetron sputtering discharges. *Physics of Plasmas*, 28(1).

[12 Zheng, B., Wang, K., Grotjohn, T., Schuelke, T., & Fan, Q. H. (2019). Enhancement of Ohmic heating by Hall current in magnetized capacitively coupled discharges. *Plasma Sources Science and Technology*, 28(9), 09LT03.

CHAPTER 4

STABLE ULTRA-THIN SILVER/ALUMINUM ALLOY FILMS

4.1 Ion Beam-Assisted Deposition of Ultra-Thin Silver Film

This part of the chapter is adapted from Thanh Tran, Xiaobo Wang, Maheshwar Shrestha, Keliang Wang and Qi Hua Fan, *"Ultra-thin silver films grown by sputtering with a soft ion beam-treated intermediate layer"*, Journal of Physics D: Applied Physics, Volume 56, Number 36

Published 7 June 2023

Published by IOP Publishing Ltd

4.1.1 Introduction

Ultra-thin continuous silver films with thicknesses of less than 10 nm are attractive for low-E glass coatings and optoelectronic devices because of the high electrical conductivity, optical transmittance, and plasmonic figure of merit [1]. However, it is a challenge to produce ultra-thin and environmentally stable silver films. One of the limitations is the low wettability of silver on glass and many other surfaces. As a result, the initial growth stage of silver thin films follows the Volmer-Weber mode characterized by the formation of non-continuous islands with micro-voids [2, 3]. The micro-porous silver films have poor adhesion to the substrate and are easily de-wetted in ambient air or at elevated temperatures, especially with the presence of reactive gases [4, 5, 6, 7].

Various methods have been studied to enhance the wettability of silver to substrates and grow ultra-thin continuous and dense silver films. A primary method is to grow a wetting layer such as Ge [8, 9, 10], Cu [11, 12], Ni [13], Al [14], oxygen-incorporated silver films (Ag(O))

[15, 16, 17, 18], and aluminum doped zinc oxide (AZO) [19]. Other methods such as using silver alloys were also reported [1, 5]. However, there are several drawbacks to using a wetting layer. It requires additional processing steps, and the added layer usually reduces the film transmittance. Table 4.1 summarizes sheet resistance of ultra-thin silver films along with their structures and effective thicknesses, reflecting a significant variation in the electrical performance of silver films due to the effectiveness of different wetting methods. It is worth noting that creating a silver alloy typically results in increased resistivity, and this effect can be particularly significant in the case of silver-aluminum binary alloy [5, 20].

Table 4.1: Sheet resistance of some silver ultra-thin films reported. The effective thickness is the sum of thickness of silver film and metal seeding layer

Film structure	Effective thickness (nm)	Sheet resistance ($\Omega/sq.$)	Reference
Al-doped Ag_6 nm/Glass	6	73.9	[5]
Ag_5 nm/ Ge_1 nm/Glass	6	23	[12]
Ag_5 nm/ Cu_1 nm/Glass	6	20	[12]
Ag_6 nm/Glass	6	>1000	[12]
Ag_10 nm/ Ge_2 nm/SiO_2/Si (100)	12	20	[10]
Ag_6 nm/ Cu_1 nm/SiO_2/Si (100)	7	15	[11]
Ag_4.5nm/Ag(O)_1.5 nm/ZnO/Glass	6	12.5	[15]
ZnO/Ag(O)_8 nm/ZnO/PET	6	27	[16]
Ag_10 nm/Al_1 nm/Glass	9	13	[14]

Ion beam assisted deposition has been recognized as an effective approach to modulating thin-film growth. In ion beam assisted deposition, ions transfer energy to the atoms as they are deposited, leading to enhance nucleation and crystallization [21]. However, conventional ion

sources (e.g., the anode layer ion source) compatible with thin-film growth usually create ions with energies over 100 eV. These energetic ions can intensively sputter the deposited silver atoms on the substrates due to the high sputtering yield, leading to limited control of the silver film microstructure.

This work demonstrates the growth of ultra-thin silver films by using a soft ion beam treatment to enhance the wettability of silver films on glass substrates. The soft ions are generated by a proprietary single beam ion source that can emit ions with controllable energies below 60 eV. This study focuses on using the soft ion beam treatment to grow an initial silver seed layer of ca. 1 nm thickness and its effects on the structure of the ultimate films of 6-9 nm thickness. This growth scheme aims to mimic the in-line large-area coatings where an ion source combined with a sputtering magnetron would only treat the initially deposited film as the substrate passes in front of the plasma sources. The optical transmittance and electric resistivity of the silver films grown with and without the ion beam treated seed layer are compared and correlated with the film microstructure and morphology.

4.1.2 Experiment and Method

Borosilicate glass was used as substrates. The substrates were cleaned in an ultrasonic bath using acetone and methanol followed by baking at 100 °C for 30 minutes before the deposition. The sputtering system (Kurt J. Lesker Company® PVD 75 PRO Line) had multiple sputtering magnetrons, each having a shutter for pre-sputtering to clean the target. A single beam ion source (SPR-10, Scion Plasma LLC) was integrated into the sputtering system so that both ion gun and magnetron point to substrate's center from different directions at an angle of approximately 60 degree as shown in **Figure 4.1**. The ion gun emitted argon ions with estimated peak energy of 60 eV and flux density of $1 \times 10^{20}\ m^{-2}.s^{-1}$ [21, 22].

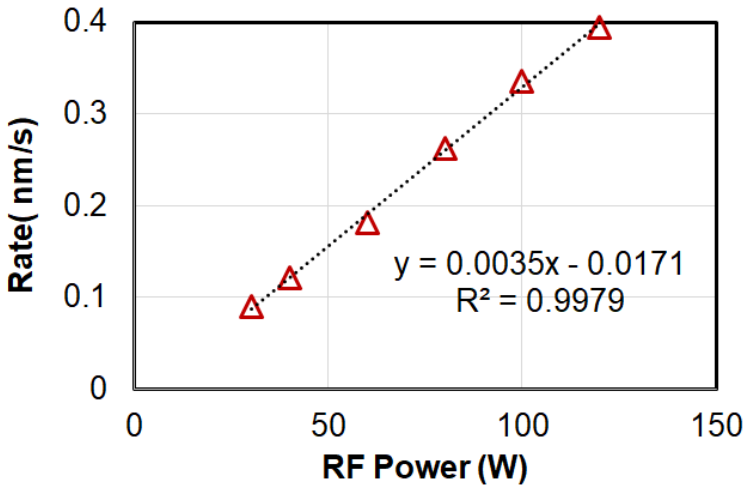

Figure 4.1: Magnetron power and deposition rates correlation of silver deposition

The vacuum chamber was pumped down to 1.3×10^{-4} Pa before the deposition. The sputtering gas was ultra-high purity grade Argon (99.999%) and the pressure was 0.4 Pa. RF sputtering was used to have better control over the thickness [23]. **Figure 4.2** illustrates the

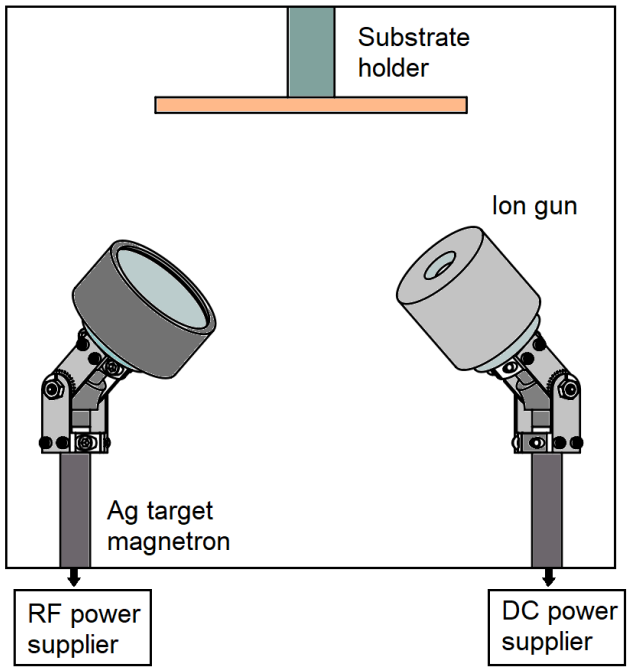

Figure 4.2: Configuration of the sputtering chamber

deposition rate of silver as a function of sputtering power. Regarding ion beam generation, the ion source was excited by a DC voltage of 120 V with a discharge current of 0.8 A. This ion source operated in a low-voltage high-current regime, generating ions with relatively low energies below 60 eV that could restructure silver films without significant sputtering of the deposited film [21]. The substrate holder rotated at a constant speed of 10 rpm during the deposition. All the depositions were conducted at room temperature. A summary of the deposition conditions is described in **table 4.2**.

Table 4.2: Depositing conditions used in this study

	IB pretreatment	**Silver (pure)**	**Silver (IB -treated)**
Target		Silver 99.99% purity	Silver 99.99% purity
Target diameter		76.2 mm (3 inches)	76.2 mm (3 inches)
Based pressure	1.3×10^{-4} Pa	1.3×10^{-4} Pa	1.3×10^{-4} Pa
Processing pressure	2 Pa	0.4 Pa	2 Pa
Processing gases	Argon (99.99%)	Argon (99.99 %)	Argon (99.99 %)
Discharge stage	120 V, 800 mA	100 W	10 W
Deposition temperature	Room temperature	Room temperature	Room temperature
Deposition technique	Ion beam pretreatment	RF magnetron sputtering	RF magnetron sputtering

The film thickness was controlled by the deposition time assuming that the deposition rate was constant under specific process conditions. For each set of process parameters, a rate test was performed first by depositing a film for an extended period of time to achieve a

thickness over 100 nm to ensure measurement accuracy. The film thickness was measured using a profilometer (DektakXT® stylus, Bruker). Before deposition, an ink line was marked across the center of a cleaned substrate. After deposition, the ink mark was removed together with the silver film on top using acetone in an ultrasonic bath leaving behind a step profile for the profilometer measurement. Then, the deposition rates were determined from the film thickness and the deposition time. The deposition rate-power correlation is shown in **Figure 4.2**.

Optical transmittance was measured using a spectrophotometer (F20 thin-film measurement system, KLA Instruments). The sheet resistance was characterized in ambient air using a four-point probe sheet resistivity meter (SRM-232-1000, Guardian Manufacturing) having a range of 0-1000 Ω/□, resolution of 0.4 Ω/□, and accuracy of 0.7 Ω/□ at 100 Ω/□. The morphology of silver films was characterized using a scanning electron microscope (Auriga Dual Column Focus Ion Beam SEM, Carl Zeiss). Glancing angle X-ray diffraction (GAXRD) was performed at an incident angle of 1^{o} (SmartLab, Rigaku). The diffractometer used Cu Kαradiation having wavelength of 1.54 Å.

The optical simulation was performed using the transfer matrix method [24, 25]. The refractive indices of silver and glass were taken from Johnson and Christy bulk silver results [26] and SCHOTT Zemax catalog 2017-01-20b, respectively.

4.1.3 Results and Discussion

4.1.3.1 Optimizing ion beam-treated silver layer

Figure 4.3 illustrates the optical performance of 6 nm silver films under different ion beam pretreatment times, corresponding to different thicknesses of ion beam-treated silver layer. In this research, a treatment time of 21 seconds corresponds to a thickness of 1 nm of ion beam-treated silver. With a treatment time of 0 second, the transmittance curve behaves as if it were

uncontinuous. The introduction of an ion beam-assisted silver layer leads to an improvement in film transmittance due to enhanced wetting properties. Notably, the ion beam-assisted silver film with a treatment time of 21 seconds demonstrates the best optical performance, as compared to theoretical results that will be discussed later in this chapter.

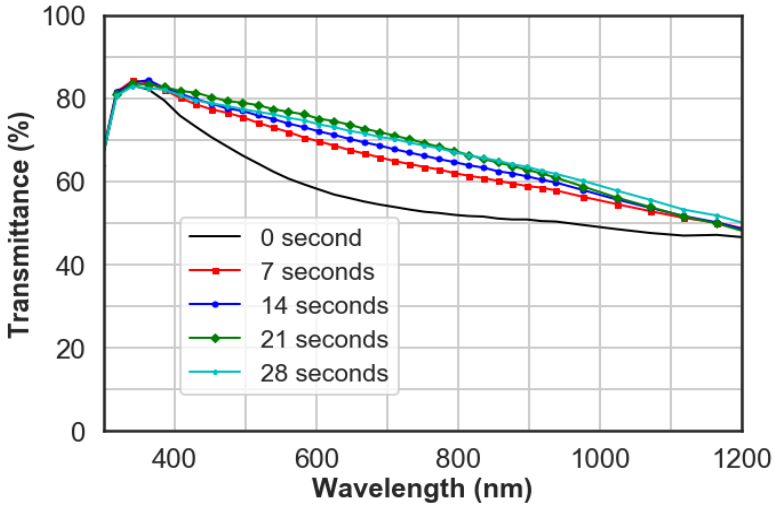

Figure 4.3: Influence of ion beam pretreatment time to optical properties of silver films

Figure 4.4 presents the sheet resistance of the films mentioned above. It strengthens the conclusion that the films without ion beam assistance lack continuity, evident in their significant higher sheet resistance compared to films containing ion beam-treated silver layer. This figure also highlights an important point: as the ion beam-treated layer exceeds a specific thickness, the sheet resistance of the film deteriorates. Therefore, there is an optimum thickness for the ion beam-assisted silver layer, which may depend on the overall thickness of silver films. In this research, with the target thickness in the range of 6-9 nm, the treatment time of the ion beam-treated silver layer was chosen to be 21 seconds, corresponding to a thickness of 1 nm. Treatment times of 7 and 14 seconds result in better sheet resistance. However, the optical performance is not as good as the film treated for 21 seconds.

Figure 4.5 illustrates the structure of a silver film with a thickness of X nm, where an ion beam-treated silver layer is incorporated for comparative research with a silver film lacking this treatment. The thickness of ion beam-treated silver layer is included in the total thickness, X, of the silver film.

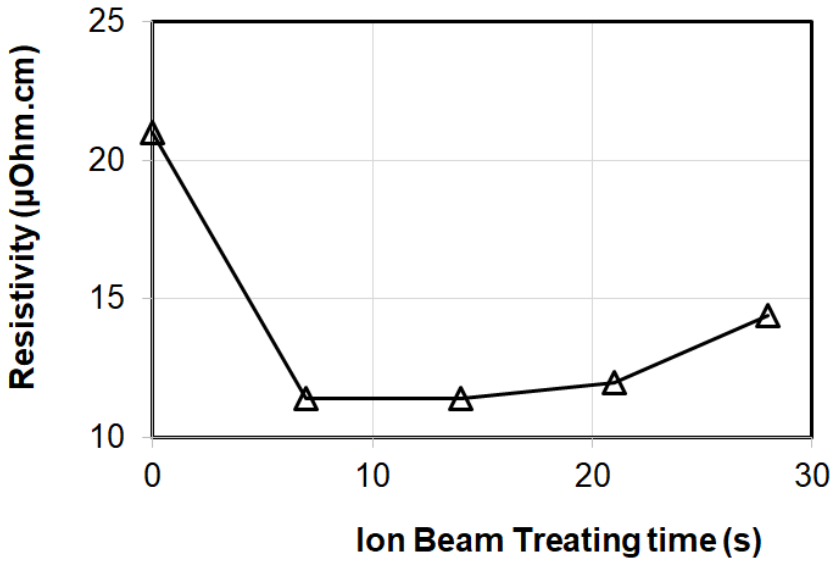

Figure 4.4: Influence of ion beam pretreatment time to resistivity of silver films. 21 seconds correspond to 1nm IB treated silver film

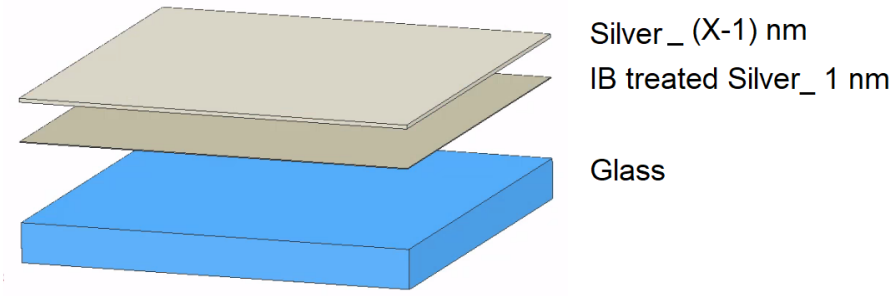

Figure 4.5: Structure of X nm silver film with the 1nm ion beam treated silver layer

4.1.3.2 Characterizations

Scanning electron microscopy (SEM) images of the silver thin films of different nominal thicknesses are shown in **Figure 4.7**. Although there are still small voids, the silver film of 5 nm thickness with the ion beam (IB) treatment is continuous and no isolated islands are observed. This is crucial to achieving high electrical conductivity. On the other hand, the silver film of 5nm and 6 nm thicknesses without the ion beam treatment have isolated islands, resulting in poor conductivity. These islands become connected once the films reach 8-9 nm. Hence, the ion beam treatment significantly reduces the percolation threshold for a continuous silver film.

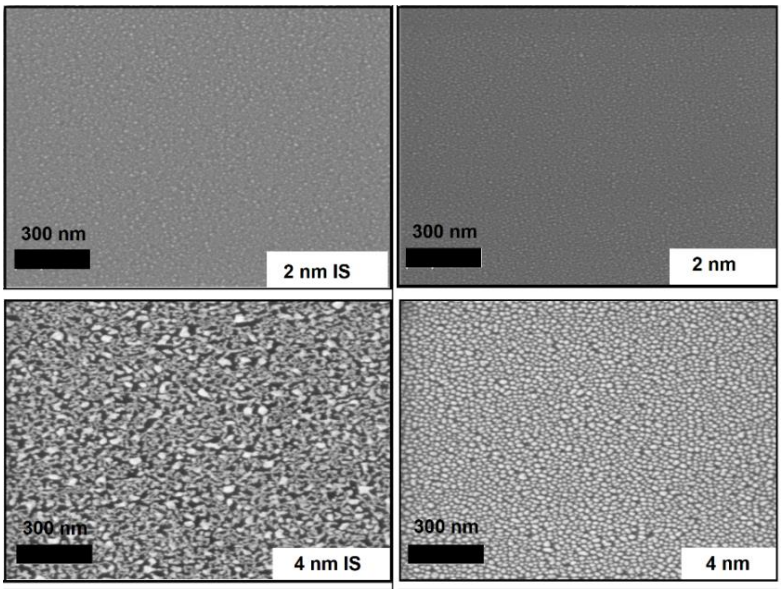

Figure 4.6: SEM images of silver thin films deposited on carbon grid at early growing stage with nominal thicknesses of 2 and 4 nm. IS: With ion beam treatment. The scale bar is 300 nm

The early growing stage of silver deposited on carbon grids with and without the ion beam treatment were examined to further investigate the effect of ion beam treatment. As shown in **Figure 4.6**, silver films thinner than 4 nm are still in islands with and without ion beam

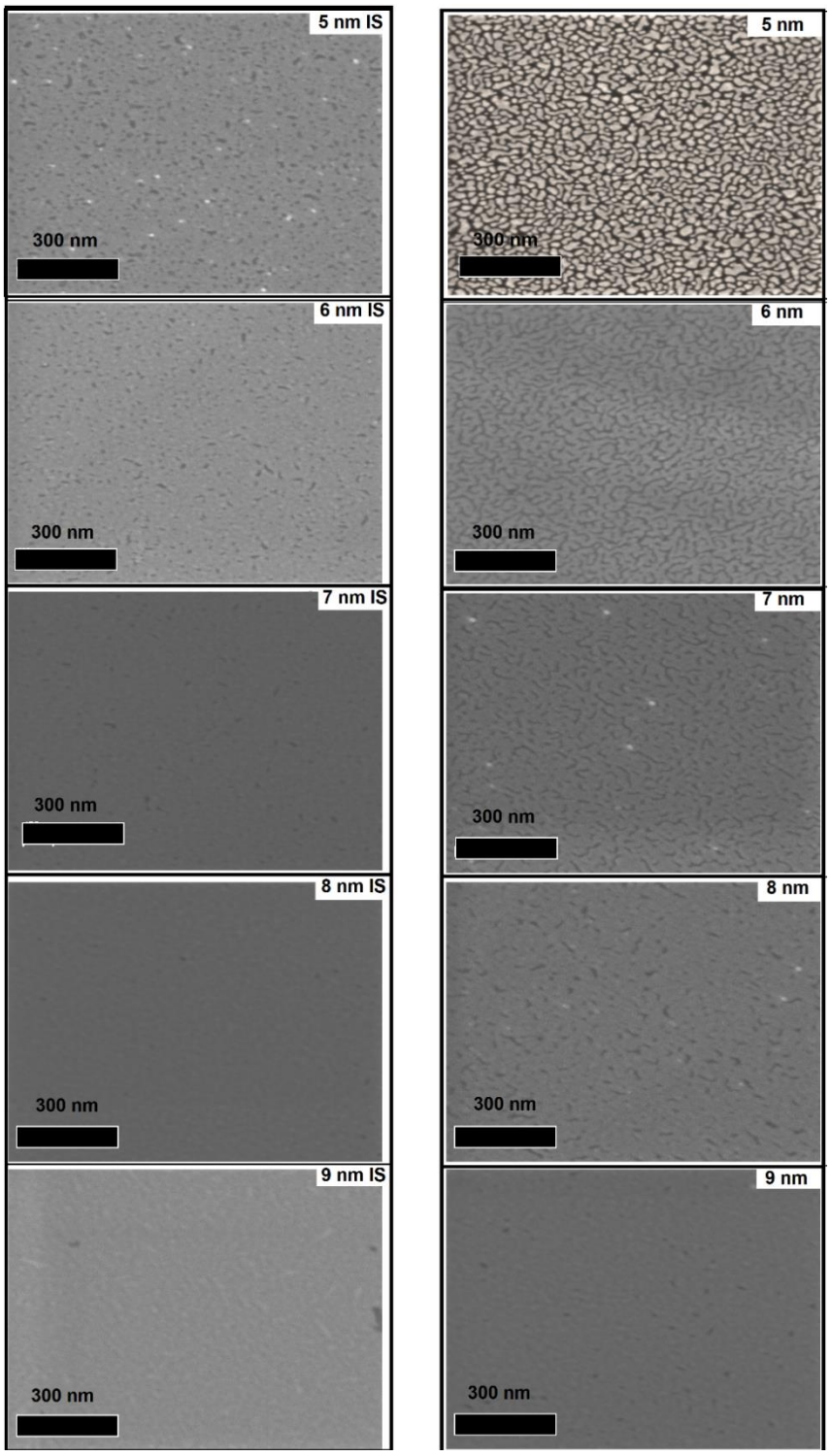

Figure 4.7: SEM images of silver thin films with nominal thicknesses of 5 to 9 nm with and without IB-treated intermediate layer. IS: With ion source. The 5 nm without IS one was deposited on carbon grids so that the film can be conductive enough for SEM characterization. The scale bar is 300 nm

treatment. However, there are two distinctions between them. The first one is the island size in the ion beam treated film bigger and a network between the islands has been formed. The second one is the islands in the ion beam treated film have irregular shapes other than round. These distinctions indicate that the ion beam treated silver has better wettability to the substrate than the untreated one.

The ion beam treatment could have several favorable effects to the growth of silver thin films. One was cleaning the substrate surface, which promoted the film wettability by increasing the substrate surface energy. The other was the ion bombardment that promoted the mobility of the deposited silver atoms and densified the film. It is worth noting that the single beam ion source discharge voltage was only 120 V, which led to a soft beam of ions with average energy below 60 eV [21]. This soft ion-surface interaction can effectively modulate the film microstructure without severe sputtering of the deposited atoms. The appearances of silver films

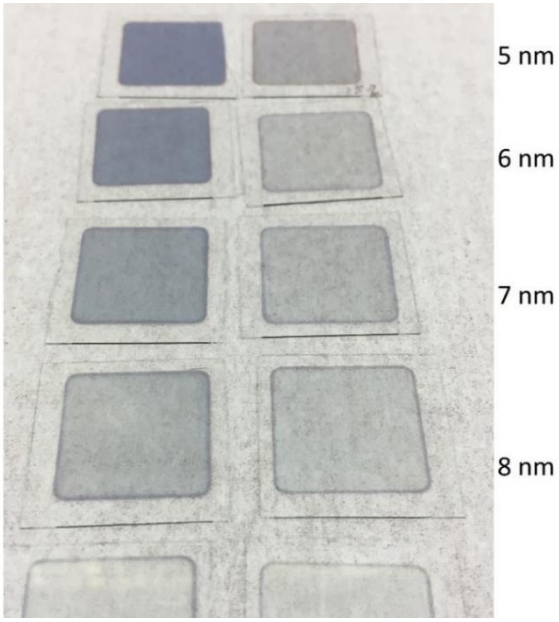

Figure 4.8: Appearance of 5-9 nm silver films with and without ion beam pretreatment

with and without ion beam pretreatment are shown in **Figure 4.8** reflect the continuity of silver films. When the film is not continuous, the color of the film turns blackish whereas the film with high continuity possesses a high clearance.

Glancing Angle X-Ray Diffraction (GAXRD) could determine the crystal structure of ultra-thin silver films [27, 28]. **Figure 4.9** illustrates the glancing angle XRD patterns of three silver films of 9 nm thickness: untreated silver film, film with 1 nm IB-treated intermediate layer, and film with 6 nm IB-treated seed layer. The 6 nm IB-treated layer is chosen for exaggerating the effects of ion beam treatment and examining the effects of simple sputtering deposition of the remaining 3 nm atop the treated layer.The XRD pattern of the untreated film shows (111) dominant crystal orientation. This result agrees with a previous report [29]. On the other hand, IB-treatment suppresses the (111) orientation and enhances the (200) growth as evidence by the decreased intensity of (111) peak and increased intensity of (200) peak when the thickness of the IB-treated layer increases. Although the mechanism is still unknown, we assume it is because of suitable energy transferred to the deposited atoms, allowing them to organize into a thermodynamically stable structure on glass substrate and this is still needed to be studied further.

The ion beam treatment not only changes the crystal orientation, but also affects the crystallinity as evidenced by the full width at half maximum (FWHM) of the (200) peak. Scherrer equation is used to calculate the crystal size: $\mathcal{T} = \frac{K\lambda}{\beta \cos\theta}$ where $\mathcal{T}$ is the mean size of the oriented crystal, K is the shape factor and is given the value of 0.9 in this work for all films, λ is the X-ray wavelength of 0.154 nm in this work, β is the full width at half maximum (FWHM) in radians, and θ is the Bragg angle. The crystal sizes of the 9 nm silver films without and with only 1 nm IB-treated seed layer are calculated to be ~6 nm. The crystal size of the silver film

with a 6 nm IB-treated seed layer is calculated to be ~17 nm, much larger than the thickness of the film. Hence, the ion beam treatment greatly enhanced the lateral growth of the crystals oriented in (200) planes.

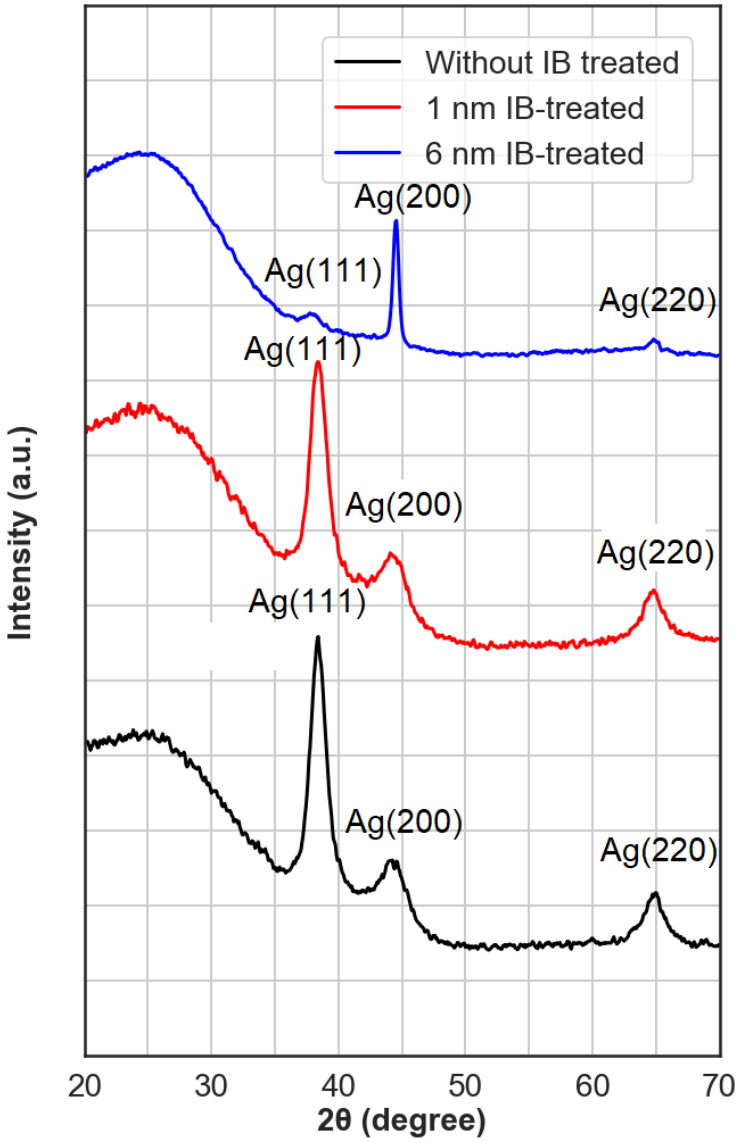

Figure 4.9: XRD patterns of silver films with total thickness of 9 nm: without ion beam treated layer, with 1 nm ion beam treated layer, and with 6 nm ion beam treated layer

Table 4.3 shows computational results of surface energy for different surfaces: (100), (110), and (111) [30]. The results imply that (111) orientation would be preferred growth direction if no additional energy is provided to the deposited atoms as it has lowest surface energy. Especially (111) is the close-packed surface and consequently has highest density of atoms. Therefore, the binding of atoms on (111) surface are weak. In other perspective, it means that atoms on (111) surface are expected to have lower activation energy and consequently have higher mobility. Therefore, diffusion of surface atoms on (111) surface is supposed to be easier than on (100) surface. According to Poletaev et al. activation energy for the migration for Ni atoms and clusters is multiple times higher in (100) nickel surface than the (111) nickel surface [31]. Both silver and nickel are transition metals and have FCC crystal structure. It is likely that the activation energy for silver atoms in (200) plane is higher than in (111) plane. Therefore, the ion beam treatment could provide significant energy to the silver atoms and enhances the growth of (200) orientation even at room temperature.

Table 4.3: Computational surface energy of silver of different surfaces [30]

Surface	Surface energy γ ($\mathrm{J.m^{-2}}$)
(1 0 0)	0.810
(1 1 0)	0.866
(1 1 1)	0.7725

High surface atom diffusivity poses challenges when attempting to create a continuous thin film. This issue arises because the combination of surface tension and the high mobility of atoms leads to the agglomeration of atoms into spherical islands to minimize energy as observed in the SEM image of a 4 nm film without IB-pretreatment (**Figure 4.6**).

To illustrate the impact of surface atom diffusion on film quality, let's consider the deposition rate. An increase in the deposition rate results in surface atoms having less time to relocate, which reduces agglomeration. Consequently, higher deposition rates tend to yield continuous film at lower thickness, as reported by previous studies [32, 33]. However, it is important to note that excessively high deposition rates can have adverse effects on film quality. For example, the higher deposition rate corresponding to less time for relocating will result in low crystallinity.

4.1.3.3 Properties and performance

An immediate effect of the improved wettability with ion beam treatment was the increased silver film adhesion. This is confirmed by using a standard 100-grid tests on 100 nm silver films deposited on glass with and without ion beam pretreatment. The result shows that the silver film with ion beam pretreatment had nearly no peeling off over the grids, whereas the majority of the grids were removed by a sticky tape (Scotch, 3 M) for the film deposited without ion beam pretreatment (**Figure 4.10**).

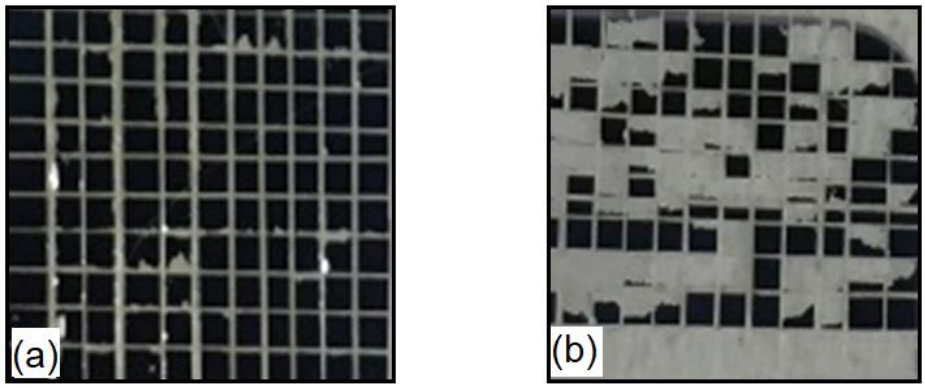

Figure 4.10: Silver film surface after 100-grid tests using Scotch tape. The silver films were deposited (a) with and (b) without ion beam pretreatment

The borosilicate glass substrate used has typical transmittance and reflectance with negligible absorption in the visible and near-infrared wavelength range. Theoretically, an ultra-thin silver film (e.g., <10 nm thickness) has low absorption. The simulated transmittance and reflectance spectra of silver thin films of different thicknesses from 5 to 9 nm on glass substrates show that a thinner silver film results in a higher transmittance, in the condition that the film is smooth and continuous [24, 25]. From the transmittance *T* and reflectance *R*, the absorptance *A* can be deduced (*A* = 100-*T*-*R*). For a silver film of 6 nm, the absorptance is less than 5% in the visible and near-infrared range (**Figure 4.11**). Therefore, an ultra-thin silver film combined with appropriate anti-reflection coatings can be highly transparent.

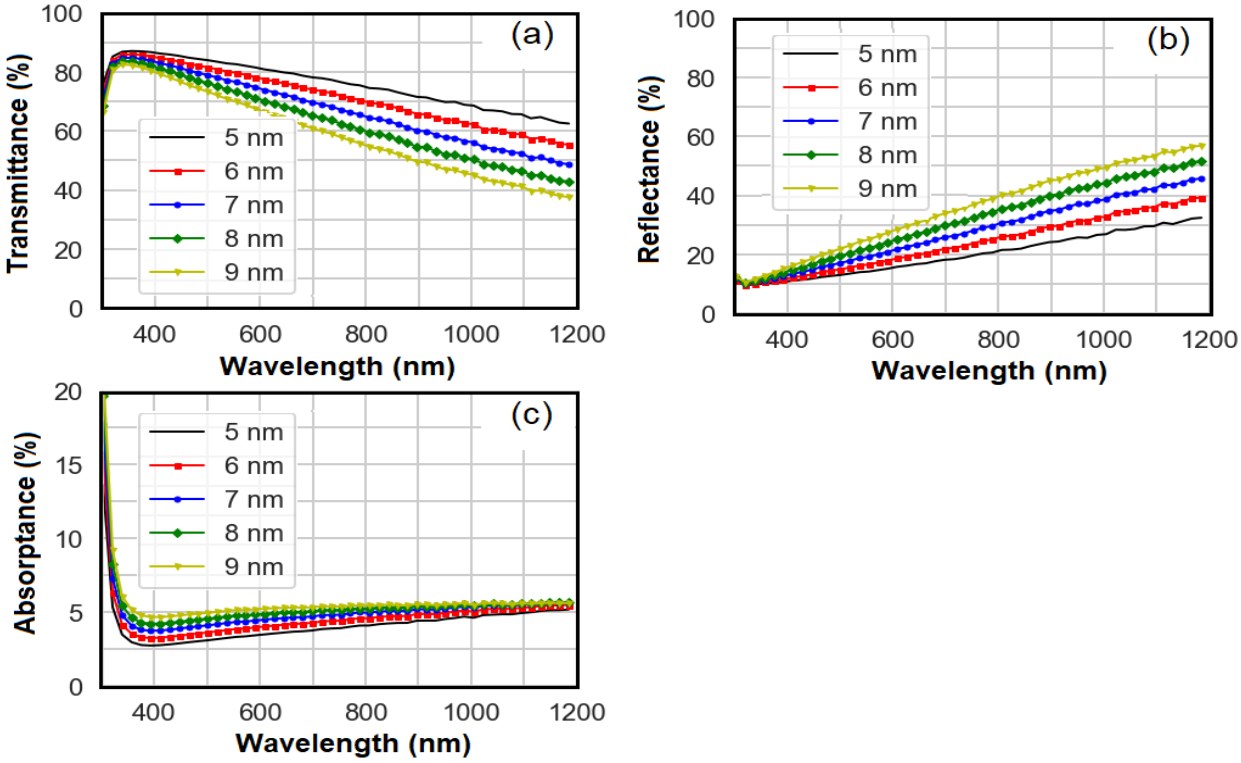

Figure 4.11: Simulated (a) transmittance, (b) reflectance, and (c) absorptance spectra of silver thin films of different thicknesses on glass. The reflective index of silver is from Brendel-Bormann model and of glass is from SCHOTT Zemax catalog 2017-01-20b

Although an ultra-thin silver film is desirable to achieve attractive optical and electrical properties, it is challenging to produce continuous silver films of less than 9 nm thickness using conventional physical vapor deposition such as sputtering. **Figure 4.12** shows the transmittance spectra of silver films of different thicknesses produced by RF magnetron sputtering. The transmittance of 9 nm thickness silver film has a similar trend as the simulated spectrum. However, the transmittance spectra of the 5-8 nm thickness films deviate from the simulation results and exhibited an obvious dip from 400 to 900 nm, which is due to the known plasmonic effect of non-continuous silver [34].

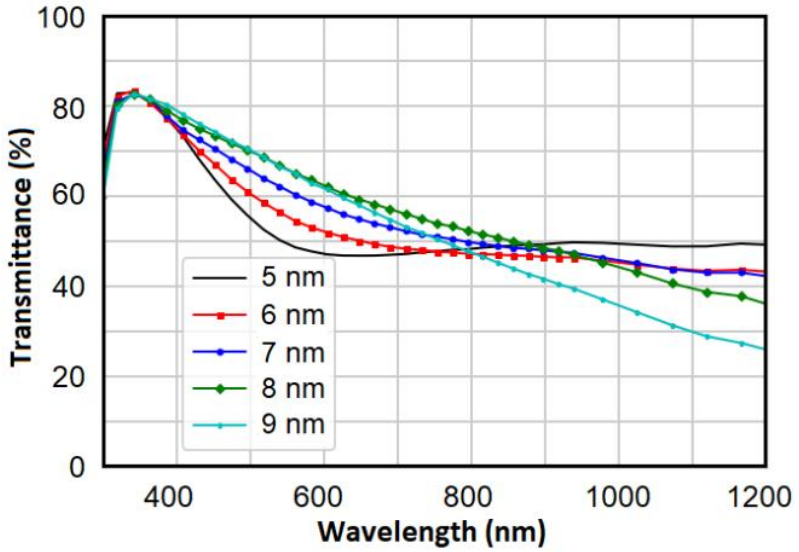

Figure 4.12: Transmittance spectra of silver thin films deposited by RF magnetron sputtering

The single beam ion source was used to enhance the growth of silver thin films. Only the initial silver layer of ca. 1 nm was treated with the soft ion beam. This seed layer was not necessarily continuous yet. A subsequent silver layer was grown on top of this seed layer by magnetron sputtering without the ion beam treatment and the total film thickness included both layers as shown in **Figure 4.5**.

Figure 4.13 (a) shows the transmittance spectra of silver films of different thicknesses sputtered atop the 1 nm ion-beam-treated intermediate layer. Except the film of 5 nm thickness, the transmittance spectra of the other silver films of 6-9 nm thickness followed the same trend as the simulated results shown in **Figure 4.13** (b). From SEM characterization, a continuous silver

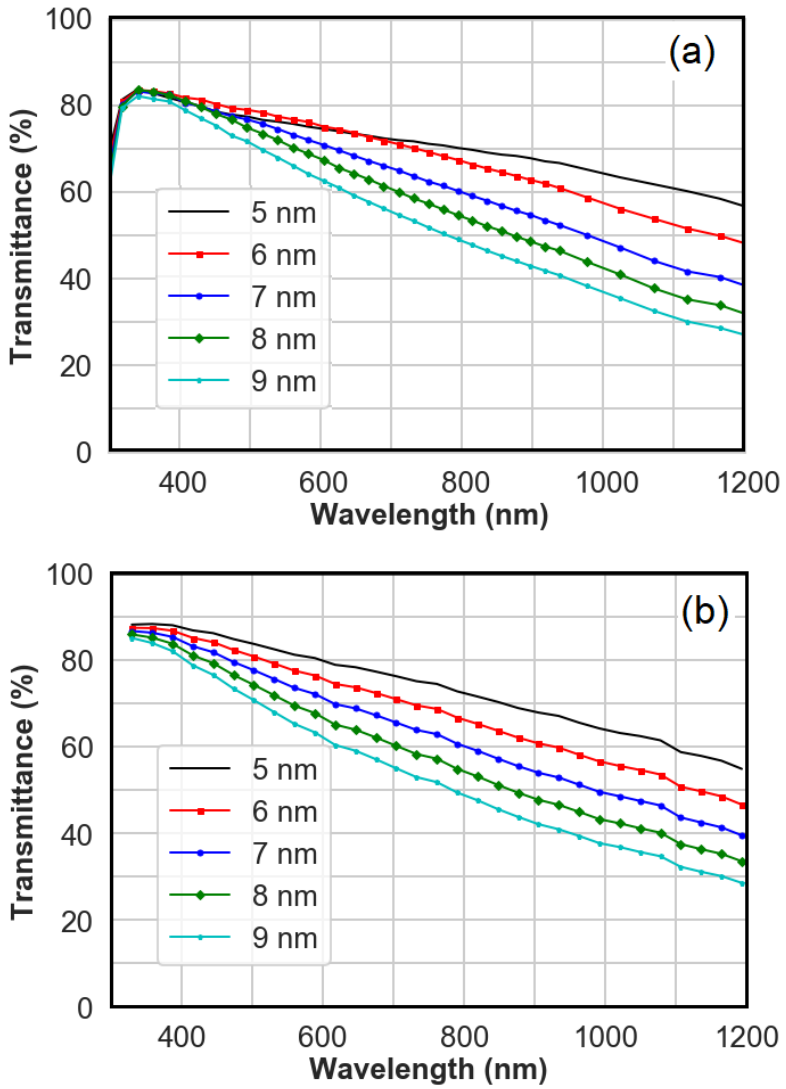

Figure 4.13: (a) Transmittance spectra of silver thin films sputtering deposited with ion beam treatment, and (b) simulated transmittance spectra of continuous silver thin films based on experimental reflective index from Johnson and Christy bulk silver results [26]

film of ~6 nm was produced on glass with the assistance of the single beam ion source, whereas a thickness of about 9 nm was required to produce a continuous silver film without the ion beam treated seed layer. This indicates that the discontinuity is the reason for having concave shape in the transmittance spectrum at the wavelength region of 400 nm to 600 nm.

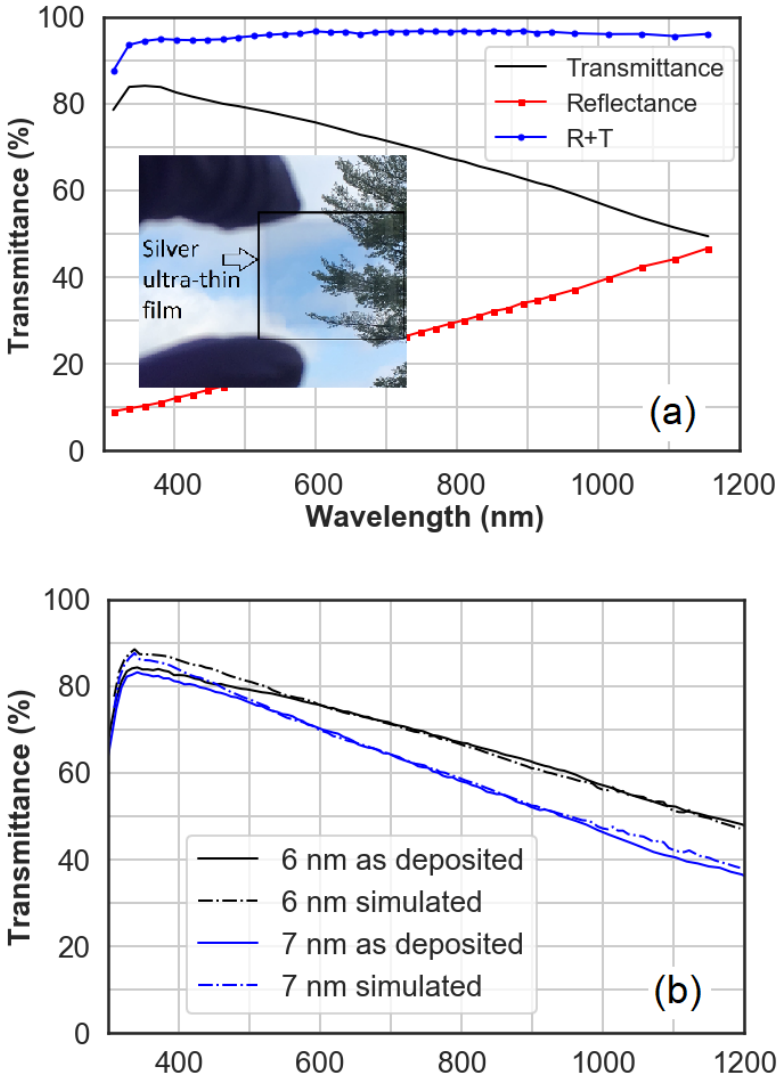

Figure 4.14: (a) Transmittance (T), Reflectance (R), and their sum (R+T) of a 6 nm continuous silver film deposited with the support of ion beam pretreatment and aluminum cap layer. The absorptance consequently is 1-(R+T) is supposed to be smaller than 5%. (b) Comparison of deposited and simulated transmittances of 6 nm and 7 nm films show a good agreement except at short wavelength part due to scattering effect

Figure 4.14 (a) shows the transmittance T, reflectance R, and T+R in one graph for a 6 nm silver film deposited on glass with the ion beam treated seed layer. A photograph is inserted to demonstrate the highly transparent film. The sum of transmittance and reflectance is higher than 95% in visible and infrared ranges. Therefore, with an appropriate optical design, this ultra-thin silver film could lead to high reflectance in the infrared and high transmittance in visible light ranges, which is particularly attractive for low-E glass coatings [35]. **Figure 4.14** (b) shows a closer look at the transmittance of 6 nm and 7 nm compared to simulation resulted using Johnson and Christy bulk silver refractive index [26]. The spectra are in good agreement in the long wavelength range and slightly off in the short wavelength range, likely due to the scattering caused by the voids.

In addition to achieving high transmittance, the ion beam treatment also resulted in significantly reduced resistivity of ultra-thin silver films, as shown in **Figure 4.15**. For example,

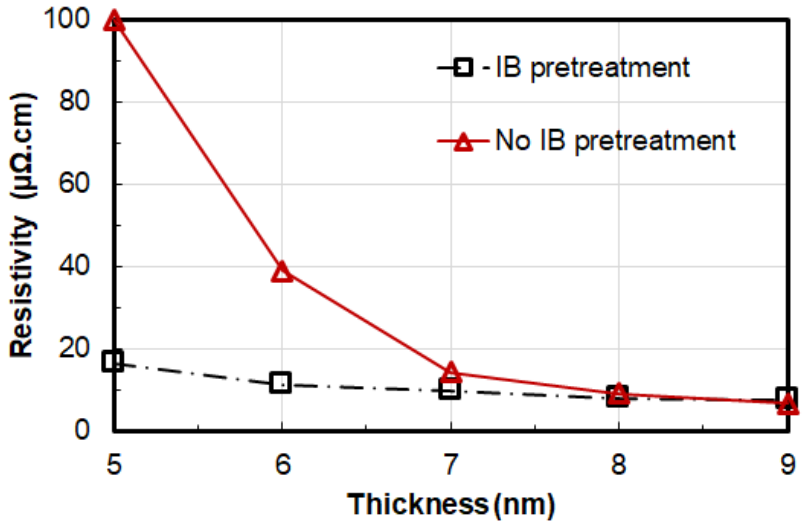

Figure 4.15: Resistivity of silver thin films produced with and without ion beam pretreatment

the ion beam treated silver thin film of 6 nm thickness had a resistivity of approximately 11.4 μΩ.cm, corresponding to a sheet resistance of roughly 19 Ω/□, compared to 39 μΩ.cm of the untreated silver film of the same thickness. This is among the best performances of reported ultra-thin silver film (see **Table 4.4**). These results match with the transmittance spectra presented above, indicating that the ion beam treatment forms continuous silver films and results in improved transmittance and resistivity.

Table 4.4: Sheet resistance of some silver ultra-thin films reported. The effective thickness is the sum of thickness of silver film and metal seeding layer

Film structure	Effective thickness (nm)	Sheet resistance ($\Omega/sq.$)	Reference
Al-doped Ag_6 nm/Glass	6	73.9	[5]
Ag_5 nm/ Ge_1 nm/Glass	6	23	[12]
Ag_5 nm/ Cu_1 nm/Glass	6	20	[12]
Ag_6 nm/Glass	6	>1000	[12]
Ag_10 nm/ Ge_2 nm/SiO_2/Si (100)	12	20	[10]
Ag_6 nm/ Cu_1 nm/SiO_2/Si (100)	7	15	[11]
Ag_4.5nm/Ag(O)_1.5 nm/ZnO/Glass	6	12.5	[15]
ZnO/Ag(O)_8 nm/ZnO/PET	6	27	[16]
Ag_10 nm/Al_1 nm/Glass	9	13	[14]
Ag_5 nm/ IB-treated Ag_1 nm/Glass	6	19	This work

4.1.4 Conclusions

This work studied the influences of the ion beam treated intermediate silver layer on practical properties of sputtering grown ultra-thin silver films, including optical, electrical, and

adhesive properties. Initially, a single beam ion source was used for pretreatment, resulting in the creation of an optimized 1 nm ion beam-treated silver layer. This treatment greatly improved the film's wettability. Consequently, we were able to achieve a continuous silver film with a thickness of only 6 nm, while conventional magnetron sputtering alone would require ~9 nm to achieve the continuous film. The SEM images show that the introduction of the ion beam-treated intermediate layer encourages the silver to spread out on the surface. In contrast, without the ion beam-treated layer, silver atoms tend to cluster together, forming spherical islands. The difference in behavior is likely due to the higher surface energy of the substrate treated by the soft ion beam or the reduced mobility of surface atoms on the ion beam-treated films.
X-ray diffraction (XRD) characterization revealed distinct crystallographic differences in the ion beam-treated layer compared to silver-alone sputtered films. Notably, the ion beam-treated layer exhibits a preference for (100) growth direction over (111), with growth in the (111) direction being suppressed. Additionally, as more atoms are deposited and treated with the ion beam, there is an increase in the size of crystals with a surface direction of (100). The combination of SEM and XRD results indicates that silver surface atoms exhibit higher diffusivity on the (111) surface compared to the (100) surface.

The as-deposited films demonstrate high transmittance, consistent with simulated results. The resistivity of the 6 nm and 7 nm films is measured at 11.4 μΩ·cm and 9.8 μΩ·cm, respectively. Based on these findings, we can make modifications to further enhance the wettability of silver films. For example, increasing the deposition rate can reduce the movement time of surface atoms, and introducing a portion of nitrogen as the sputtering gas, which has been reported to aid in the growth of (100) silver.

4.2 Stable Ultra-Thin Silver Films Grown by Soft Ion Beam-Enhanced Sputtering with an Aluminum Cap Layer

This part of the chapter 4 is adapted from Thanh Tran, Maheshwar Shrestha, Nina Baule, Keliang Wang and Qi Hua Fan, *"Stable Ultra-thin Silver Films Grown by Soft Ion Beam-Enhanced Sputtering with an Aluminum Cap Layer"*, ACS applied materials & interfaces. Publication Date:June 9, 2023,

4.2.1 Introduction

Ultra-thin continuous silver films (< 9 nm in thickness) have many attractive electrical and optical properties that makes them suitable for variety of optoelectronic applications. They have the lowest resistivity of any metal ($1.59 \times 10^{-8}\ \Omega\,\mathrm{m}$), making them highly conductive [36]. They have low optical absorption in both the visible and infrared ranges [37]. Using appropriate optical coatings, such as a sandwich structure, the reflectance and transmittance of the stack can be engineered for specific applications (e.g., low-emissive glass) [15, 38, 39]. Furthermore, silver is highly ductile and durable, making it ideal for flexible electronics [15, 40]. Furthermore, ultra-thin silver has a high plasmonic figure of merit, making it useful for plasmonic applications [1, 19, 35, 41].

However, two main issues limit the use of ultra-thin silver films. First, fabricating continuous silver films that are less than 9 nm thick is challenging because they tend to follow a Volmer-Weber growth mode that results in the formation of isolated islands [2, 3, 4, 42, 43]. Second, silver films are prone to degradation and de-wetting when exposed to reactive gases and/or at elevated temperature [5, 6, 7, 44, 45, 46]. They can react easily with gases such as

hydrogen sulfide, forming dark grey compounds like Ag_2S that reduce the film transmittance [47]. These issues need to be addressed in order to expand the use of ultra-thin silver films. **Figure 4.16** and **Figure 4.17** illustrate visual representations of the challenges reflected in optical transmittance spectra. The figure reveals the degradation of transmittance spectra thermally and environmentally for typical 6 nm silver films deposited by RF magnetron sputtering without any treatment or protective measures. In **Figure 4.16** (a), we see a film taken out immediately after deposition, while in **Figure 4.16** (b), a film was left in a vacuum chamber for 2 hours before removal.

At time 0, the transmittance spectra of both films exhibit a noticeable dip spanning from 400 to 900 nm, attributable to the well-known plasmonic effect associated with non-continuous silver [34]. However, both transmittance spectra of these ultra-thin silver films degrade rapidly in ambient air due to an agglomeration process that results in discontinuous films. This degradation is evident from the distinctive concave curve in the 400 - 600 nm wavelength range of the transmittance spectra.

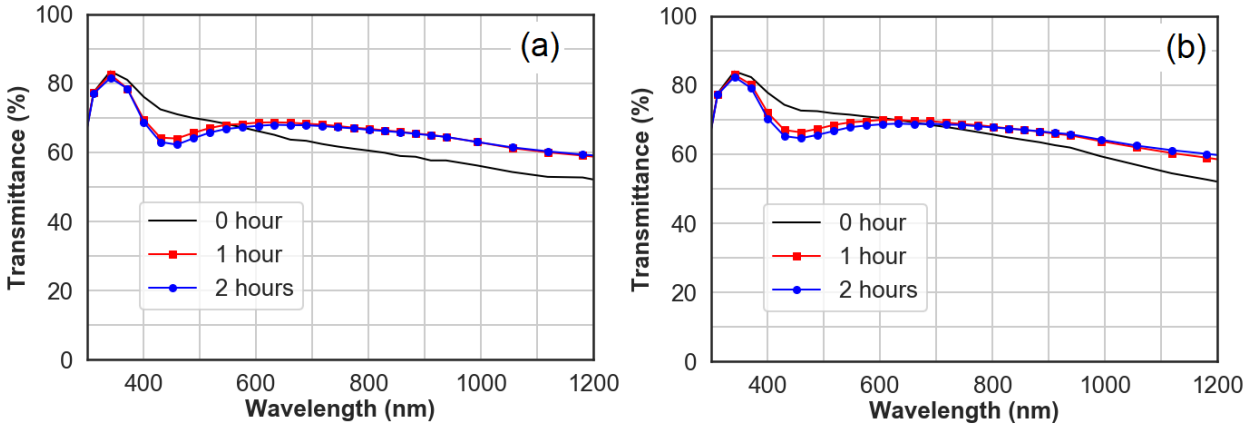

Figure 4.16: Transmittance spectra of typical 6 nm silver films exposed to the ambient air for different exposing times after being kept in vacuum chamber for (a) 0 hour and (b) 2 hours after deposition

Comparing the spectra at different time points, we observe that the 0-hour spectra for both films display only slight deviations, while the 1-hour and 2-hour spectra show significant

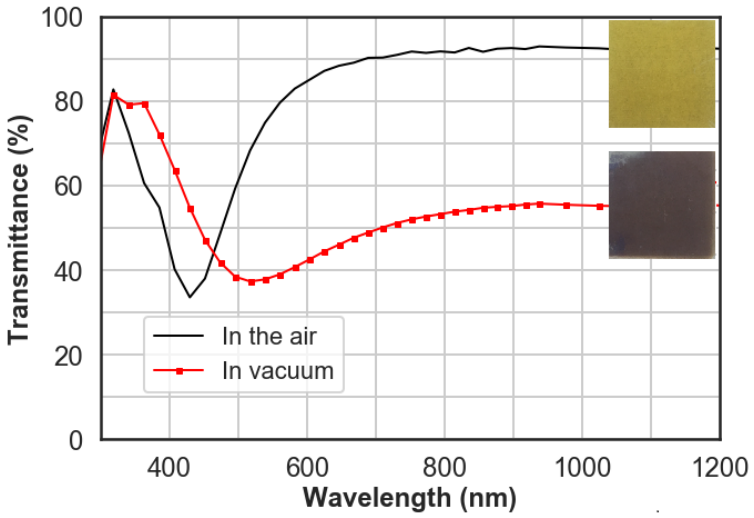

Figure 4.17: Transmittance of degraded films at high temperature in the air and in vacuum

deviations. This indicates that agglomeration occurs within the vacuum and accelerates once the films are exposed to ambient air, a phenomenon reported by Sharma et al. [7]. Furthermore, it is important to note that the degradation of silver thin films becomes more pronounced, even in a vacuum, at higher temperatures [44]. In **Figure 4.17**, silver films are degraded in air and vacuum due to high temperature. They show different appearances due to the difference in microstructure of agglomeration.

Several approaches have been developed to address the issue of fabricating continuous, ultra-thin silver films. One common method is to add a wetting layer of Ge, Cu, or Ni, although this often leads to reduced transmittance [8, 9, 10, 11, 13]. Our previous work demonstrates that using a 1 nm wetting layer of ion beam treated silver helps to deposit a continuous ultra-thin silver film of around 6 nm in thickness without compromising its electrical and optical performances. The ion beam treated layer modified crystal orientation and improved the

wettability of silver film [37]. This technique was used as granted to deposit ultra-thin silver films in this work whereas the main focus of this paper is trying to address the second problem. The stability of ultra-thin silver films in ambient air and at high temperatures is another concern that has been addressed in the literature. Gu et al. (2014) found that adding 4 at% of aluminum to a 15 nm thick silver film greatly enhanced its stability. They demonstrated that the silver-aluminum alloy films were stable in N_2 even at 300 °C [5]. However, forming an alloy typically introduces defects and increases the scattering of charge carriers, leading to reduced electric conductivity according to Mathiessen's rule [20, 48]. Sasaki et al. recently reported that a thin aluminum layer (2-5 nm thick) deposited on top of a 150 nm silver film led to stable optical reflectance in ambient air with high humidity at 50 °C [47]. Although this aluminum cap layer is too thick for applications that require high transmittance, it shows that it is possible to achieve low electric resistivity in silver films with improved stability. Wu et al found that 2 nm of Al_2O_3 and 1.5 nm of MgO cap layers can prevent the degradation of silver films due to oxidation [49]. However, these non-conductive oxide cap layers are not suitable for transparent conductive electrodes. Alternative conductive oxides such as indium-tin-oxide thin films could be used to protect silver films. However, the deposition of transparent conductive oxide thin films often requires a small fraction of oxygen, which can be detrimental to the silver film.

This research investigates the use of an aluminum/silver duplex structure as a means of achieving excellent thermal and environmental stability without compromising the electric and optical properties of ultra-thin silver films. The key feature of this duplex structure is that the aluminum deposited on the silver is in the form of atomic cluster islands. This approach is motivated by two assumptions: firstly, that forming aluminum islands on top of a silver film could reduce scattering of the charge carriers compared to adding aluminum into the silver

matrix, and secondly, that aluminum has a lower electromotive force than silver and could protect silver from oxidation by forming a galvanic couple. The performance of the resulting films will be compared to that of pure silver films and co-deposited aluminum-silver thin films.

4.2.2 Experiment and Method

Borosilicate glass substrates was cut into 25×25 mm and cleaned using an ultrasonic bath with acetone and methanol, followed by baking at 100 °C for 30 minutes before deposition. The sputtering system (Kurt J. Lesker Company® PVD 75 PRO Line) had multiple sputtering magnetrons and each magnetron had a shutter for pre-sputtering. A single beam ion source (SPR-10, Scion Plasma LLC) was integrated into the sputtering system as shown in **Figure 4.18** [21, 22].

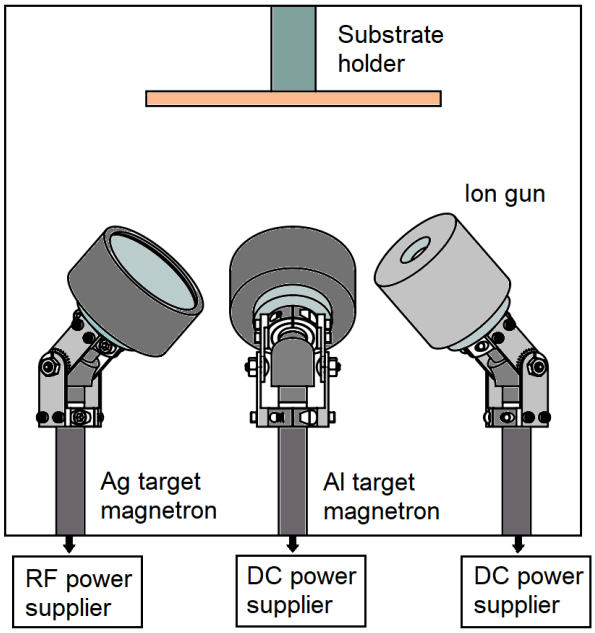

Figure 4.18: Configuration of the sputtering chamber

The vacuum chamber was pumped down to below 1.3×10^{-4} Pa before deposition. The sputtering gas was ultra-high purity grade argon (99.999%) at a pressure of 0.4 Pa. The processing parameters for creating a seed layer of silver using the ion beam treatment are summarized in **Table 4.5**. The ion source operated at 100 W with a corresponding discharge voltage of 120 V. At the same time, the silver was radio frequency (RF) sputtered at the power of 10W to deposit the seeding layer of 1 nm thick. Then, conventional sputtering was used to deposit the remaining silver films at a rate of 0.3 - 0.35 nm s^{-1} using RF power in the range of 90 – 100 W. Aluminum was co-sputtered or deposited on top of silver films using pulsed DC power, with the concentration of aluminum varied by adjusting the power applied to the aluminum target. The deposition rate-power correlations of these films are provided in the **Figure 4.19**. The substrate holder rotated at a constant speed of 10 rpm during the deposition. All the depositions were conducted at room temperature.

To compare the properties of pure silver films with aluminum-silver co-deposited and aluminum/silver duplex films, the total thickness was maintained at ~7 nm for all samples, including a 1 nm seed layer of silver, deposited using ion beam treatment as previously reported. Films with different atomic percentages of aluminum were fabricated to compare the optical and electrical properties. The aluminum-silver co-depositions were made by simultaneous sputtering of silver and aluminum. The aluminum atomic concentration was estimated according to the deposition rates. The duplex coatings were made by depositing a silver film on glass substrate first followed by depositing aluminum on top.

Table 4.5: Processing conditions

	IB pretreatment	**Silver (IB -treated)**	**Silver (pure)**	**Aluminum**
Target		Silver 99.99% purity	Silver 99.99% purity	Aluminum 99.99% purity
Target diameter		76.2 mm (3 inches)	76.2 mm (3 inches)	76.2 mm (3 inches)
Based pressure	1.3×10^{-4} Pa	1.3×10^{-4} Pa	1.3×10^{-4} Pa	1.3×10^{-4} Pa
Processing pressure	2 Pa	2 Pa	0.4 Pa	0.4 Pa
Processing gases	Argon (99.99%)	Argon (99.99 %)	Argon (99.99 %)	Argon (99.99%)
Discharge power	100 W	10 W	90 W-100 W	0 W-30 W
Deposition temperature	Room temperature	Room temperature	Room temperature	Room temperature
Deposition technique	Ion gun	RF magnetron sputtering	RF magnetron sputtering	DC magnetron sputtering

The film thickness was controlled by the deposition time, assuming a constant deposition rate under specific process conditions. For each set of process parameters, a rate test was performed first by depositing films for an extended period of time to achieve thicknesses over 100 nm to ensure measurement accuracy. The film thickness was determined by using a profilometer (DektakXT® stylus, Bruker). An ink line was marked across the center of a cleaned substrate. After deposition, the ink mark was removed together with the silver film on top using acetone in an ultrasonic bath leaving behind a step profile for the profilometer measurement. Then, the deposition rates were determined from the film thickness and the deposition time (see **Figure 4.19** for deposition rates of different films). The error bar for these thickness measurements was within 2%, hence for a 7 nm film, the error bar is interpolated to be 0.14 nm.

Normally, the early growth stage has the nucleation process, and it takes time, which is called incubation time. Therefore, the interpolated thickness for a thinner film is likely the upper bound of the actual thickness. In addition, we indirectly confirmed the film thickness by comparing the film transmittance with the simulated results, indicating they were in good agreement and our film thickness controlled by the deposition time was reasonably accurate.

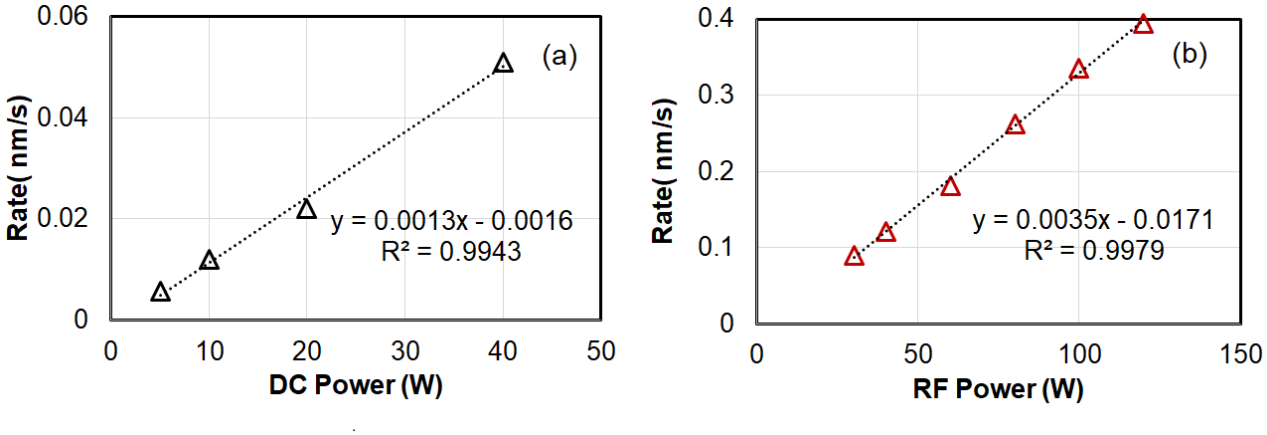

Figure 4.19: Magnetron power and deposition rates of (a) aluminum and (b) silver correlations

Figure 4.20 shows the comparison between deposited and simulated transmittance spectra of an ideal 7 nm silver films on glass. This shows a good agreement in transmittance of the long wavelength part (greater than 500 nm) and an offset of 5 % down at the peak's position of 350 nm. This can be explained by the structure of the films deposited. Although they are continuous, there are still pinholes and rough surfaces existing as shown in our reported work [37]. These pinholes and rough surfaces scatter better shorter wavelengths and result in the drop of transmittance in the short wavelength range less than 500 nm.

Optical transmittance was measured using a spectrophotometer (F20 thin-film measurement system, KLA Instruments) and sheet resistance was characterized using a four-point probe sheet resistivity meter (SRM-232-1000, Guardian Manufacturing), having a

measuring range of 0-1,000 Ω/□, resolution of 0.4 Ω/□, and accuracy of 0.7 Ω/□ at 100 Ω). The morphology of films was characterized using a scanning electron microscope (Auriga Dual Column Focus Ion Beam SEM, Carl Zeiss), and X-ray diffraction (XRD) was performed using Glancing Angle X-Ray Diffraction (GAXRD) [27] for thin films at a small incident angle of 2^{o} (SmartLab, Rigaku). The diffractometer uses Cu Kαradiation having a wavelength of 1.54 Å. The optical simulation was performed using a transfer matrix method [24, 25]. The refractive index of silver and glass was taken from Johnson and Christy [26] and SCHOTT Zemax catalog 2017-01-20b, respectively.

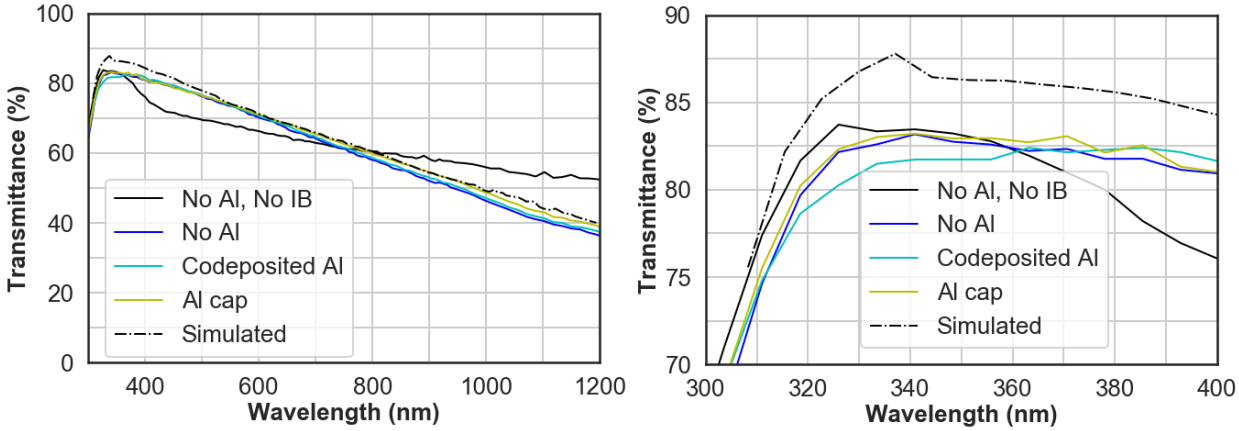

Figure 4.20: Simulated transmittance of 7 nm silver/glass compared with experimental films

4.2.3 Results and Discussion

All the silver films appeared to be continuous, as no concave feature was observed in the transmittance spectra illustrated in **Figure 4.21**. The peak transmittance at around 350 nm for the silver-aluminum alloy films slightly decreased as the aluminum concentration increased, but there was no noticeable change in the peak transmittance for the aluminum/silver duplex films.

As shown in **Figure 4.22**, the resistivity of duplex films was generally lower than that of co-deposited silver-aluminum binary alloy films. When the global atomic aluminum concentration was below 1 percent (at%), the effect of aluminum on film's resistivity was not

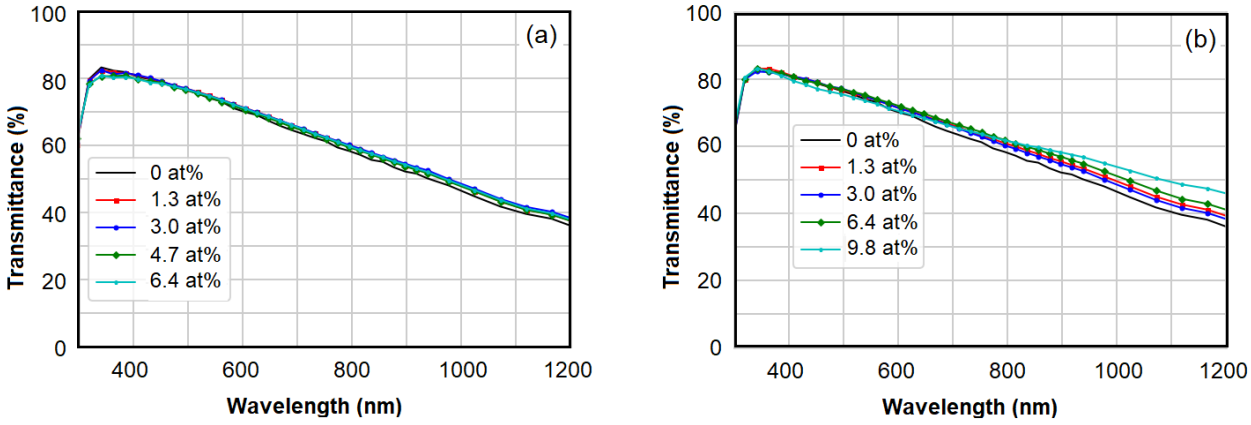

Figure 4.21: Transmittance spectra of 7 nm aluminum-added silver films with (a) aluminum co-deposited at different atomic concentration and (b) an aluminum cap layer of different thicknesses

significant for either type of film. However, the increase in the resistivity was observed for the silver-aluminum binary alloy, which is expected based on Matthiessen's rule. According to this rule, the total resistivity ρ_{matrix} of the silver film is:

$$\rho_{matrix} = \rho_{thermal} + \rho_{impurity} + \rho_{deformation} + \rho_{surface}$$

Where ρ_{matrix} is 9.1 $\mu\Omega.cm$ in this study, $\rho_{thermal}$, $\rho_{impurity}$, $\rho_{deformation}$ and $\rho_{surface}$ represent the resistivity due to electron scattering by thermal vibration, impurity, defects caused by deformation, and surfaces/interfaces, respectively [50]. When aluminum atoms are introduced into the matrix, they contribute to $\rho_{impurity}$. According to Andersson et al., aluminum and silver form a single-phase solid solution when the aluminum atomic concentration is less than 10% [51]. The resistivity of silver-aluminum alloys can be calculated using Nordheim's rule [52]:

$$\rho_{alloy} = \rho_{matrix} + C\,X(1-X)$$

where C is the Nordheim coefficient calculated to be 94 $\mu\Omega.cm$ in average (**Table 4.6**) and X is the atomic percentage of aluminum.

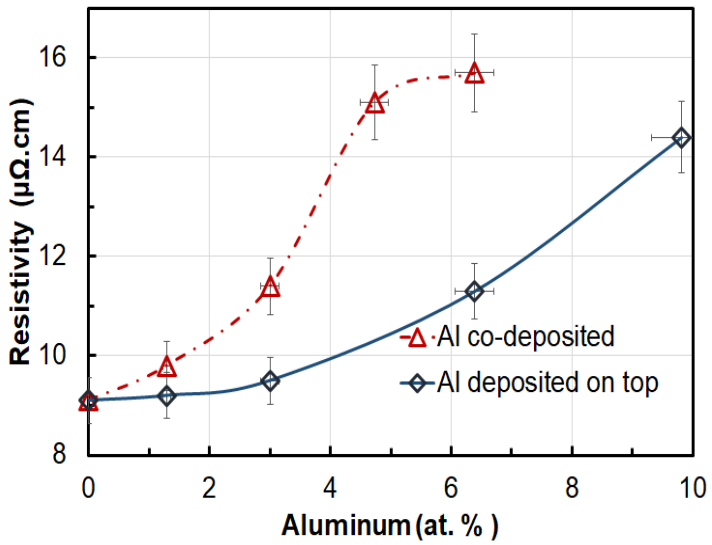

Figure 4.22: Resistivity of co-deposited and duplex aluminum films

Mao et al. reported that the influence of aluminum on the conductivity of bulk silver (1 − 1.8 μm thick) was found to increase the resistivity by ~3.5 $\mu\Omega.$ cm when 3 at. % of Al was added [20]. In co-deposited films, other factors such as surface roughness and stability may have less worse effect on resistivity, particularly $\rho_{deformation}$ and $\rho_{surface}$, compared to pure silver films as aluminum co-deposited is known to improve these properties [5]. However, the increase in impurity resistivity, $\rho_{impurity}$, outweighs the changes in deformation and surface resistivity, $\rho_{deformation}$ and $\rho_{surface}$, resulting in an overall increase in the resistivity of the silver-aluminum alloy film by ~2.5 $\mu\Omega.$ cm.

Table 4.6: Duplex and alloy silver films specifications. The calculated thicknesses are rounded as in the experiment, they have the uncertainty of 0.14 nm, corresponding to 2% of the whole thickness

Sample	Thickness (nm)	Global Al C. (at%)	Sheet R ($\Omega\backslash sq.$)	Resistivity ($\mu\Omega.cm$)	Condition	Nordheim coefficient C ($\mu\Omega.cm$)
1	7	0	13	9.1	Co-deposited	NA
2	7	1.29	14	9.8		54.97
3	7	3	16.3	11.4		79.04
4	7	4.73	21.5	15.1		133.15
5	7	6.39	22.3	15.7		110.33
6	7	0	13	9.1	Deposited on top	
7	7	1.29	14.3	10.1		
8	7	3	13.5	9.5		
9	7	6.39	16	11.3		
10	7	9.81	20.5	14.4		

In the case of duplex coating, the resistivity is increased due to the reduction in the thickness of silver film. A global aluminum concentration level of 3 % resulted in a reasonable increase of 0.4 $\mu\Omega.$ cm , or ~4 %, in resistivity. It is worth noting that, at this atomic concentration, adding aluminum on top of silver did not significantly affect the electrical conductivity of the duplex film compared to the pure silver film. At this global aluminum

concentration, the equivalent nominal aluminum thickness was 0.2 nm, and the underlying silver

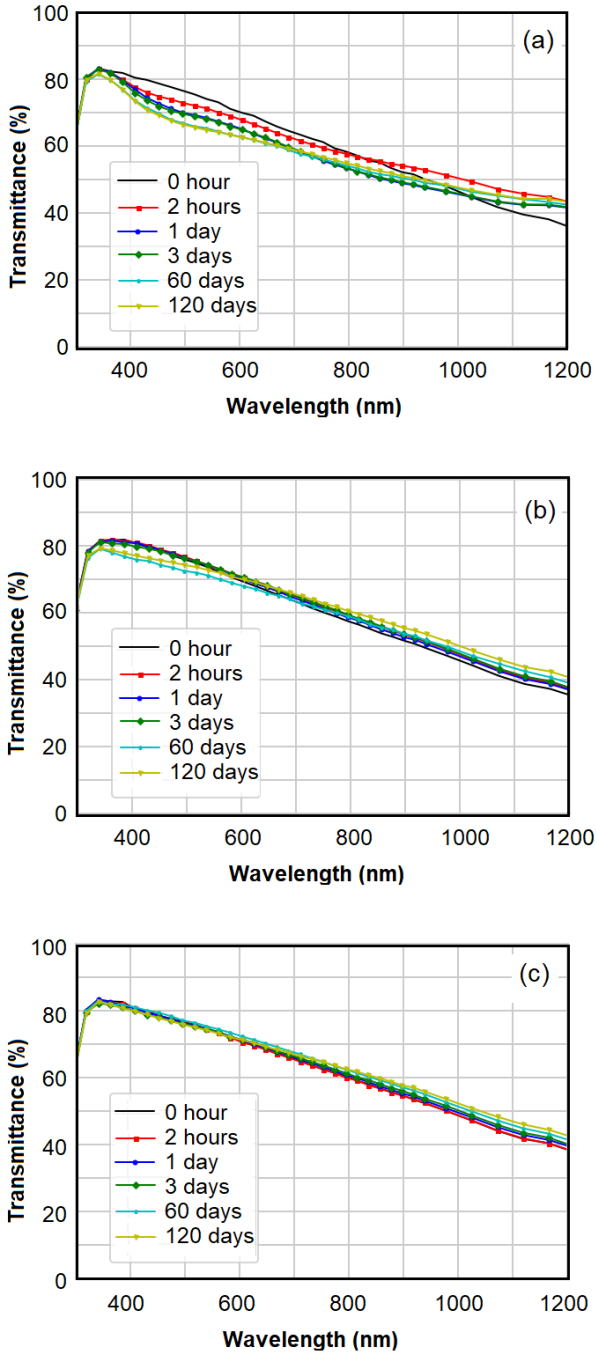

Figure 4.23: Transmission spectra of 7 nm silver films a) without aluminum, b) with aluminum co-deposited, and c) with aluminum on top after 0 hour, 2 hours, 24 hours, 3 days, 60 days, and 120 days

film was 6.8 nm thick, including the IB-treated layer. The 0.2 nm aluminum layer was likely not continuous, as the lattice constant of aluminum is 0.4 nm and it is unlikely magnetron sputtering could form a conformal single layer; therefore, the aluminum layer was expected to be composed of scattered atoms or clusters [53, 54]. Subsequently, global aluminum concentration of 3% were chosen for studying stability of the silver films.

The stability of three types of silver films was compared: a pure silver film, an aluminum/silver duplex coating, and a silver-aluminum alloy. The last two coatings were with a global aluminum concentration of 3%. All the films were approximately 7 nm thick. **Figure 4.23** shows optical degradation of these films after 120 days. The pure silver film degraded significantly after just two hours of exposure to ambient air at room temperature, while the aluminum/silver duplex coating and the silver-aluminum alloy film both showed less degradation. However, after 60 days, the duplex coating remained largely intact while the alloy film showed some degradation. After 120 days, the duplex film demonstrated negligible degradation, making it the most stable of the three films tested in terms of environmental stability. The deviation of transmittance spectra is quantitatively illustrated by root mean squares calculation expressed in **Figure 4.24**. This suggests that a thin layer of aluminum on top of the silver film can improve the stability of the silver film.

The degradation of silver films in ambient air is known as the silver mirror process. This process can lead to the degradation of silver films, which were observed through changes in their transmittance spectra. This process is thought to involve the oxidation of silver and the subsequent reaction of the resulting silver ions with hydrogen sulfide (H_2S) at the film surface to form silver sulfide [56]. A model for this process, called the oxidation-migration-reaggregation model, was first proposed by Henn and Wiest in 1963 [55]. According to this model, silver is

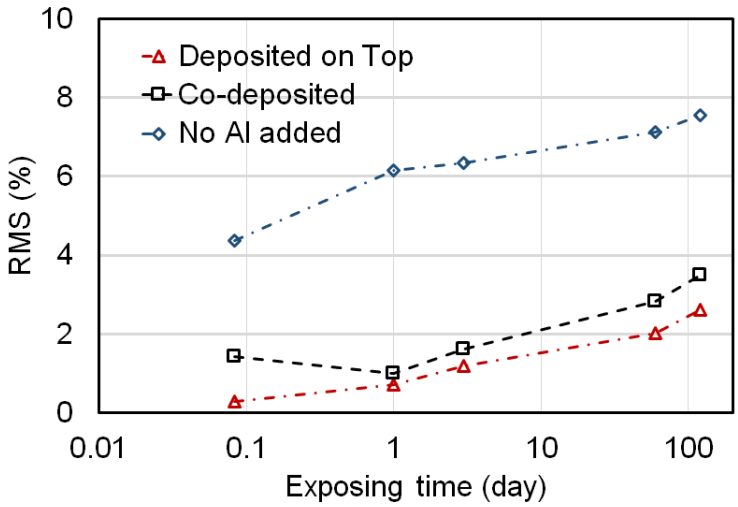

Figure 4.24: Root Mean Squares over time of transmittance spectra of three films compared to their initial spectra, measured within 5 minutes after taking the sample out of vacuum chamber

first oxidized by various oxidants present in the air, such as hydrogen peroxide, ozone, nitrogen monoxide, nitrogen dioxide, and dissolved oxygen. The silver ions then migrate to the film surface, where they react with H_2S to form silver sulfide as shown in equation below:

$$Ag_{(s)} \xrightarrow{H_2O_2/O_3/NO/NO_2/O_2} Ag^{+}_{(aq)} \xrightarrow{Migration + H_2S} Ag_2S_{(s)}$$

Aluminum and silver could form a galvanic cell as shown in **Figure 4.25**. The standard electromotive forces for aluminum and silver are -1.67 V and +0.8 V relative to a hydrogen electrode, respectively. Therefore, aluminum could prevent the silver from oxidation through a cathodic protection mechanism as predicted before [56]. Indeed, aluminum is used to clean oxidized silverware by the same mechanism [57]. In cathodic protection, aluminum atoms are oxidized and form transparent compounds such as alumina or aluminum sulfide.

The other possibility is that once aluminum reacts with oxygen, it forms an oxide cap layer. This layer could protect the underneath silver from direct contact with oxygen or prevent the migration of silver ions into the surface in the oxidation-migration-reaggregation model. Hence,

the duplex coatings appeared to be more stable than the silver-aluminum alloy films. Gu et al. also pointed out that the existence of aluminum and aluminum-oxygen bond could impede the surface diffusion of silver atoms and make the silver films stable at high temperatures [5].

Figure 4.26 below shows the XRD patterns of degraded co-deposited and duplex films

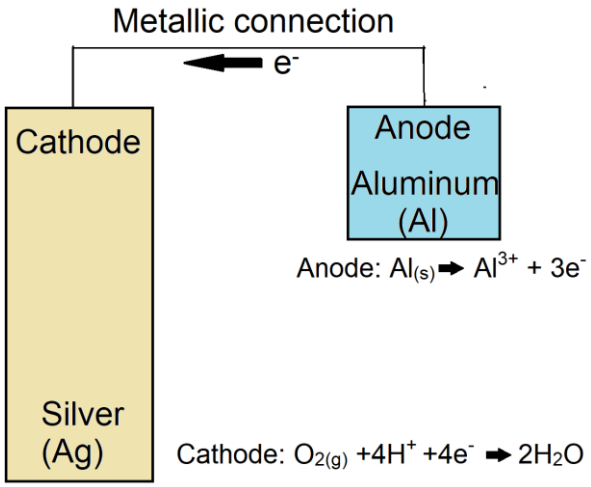

Figure 4.25: Cathodic protection mechanism of silver film using aluminum having lower standard electromotive force

after being exposed to the air for 1 year, which support the cathodic protection mechanism. An XRD peak at 30^{o} in the co-deposited and duplex films was observed. It is most possibly related to Al because silver and Ag_2O do not have an XRD diffraction peak at that angle. As we discussed before, the Al cap layer is unlikely a continuous layer, rather it exists in the form of islands, each consisting of multiple layers of Al atoms. The surface layers of these Al islands would be oxidized first, which would be attributed to the cathodic protect mechanism. The oxidation would result in the formation of a mixture of Al_2O_3, Al_2S_3, and other compounds. In the presence of H_2S, the main components of corrosion products are aluminum hydroxide,

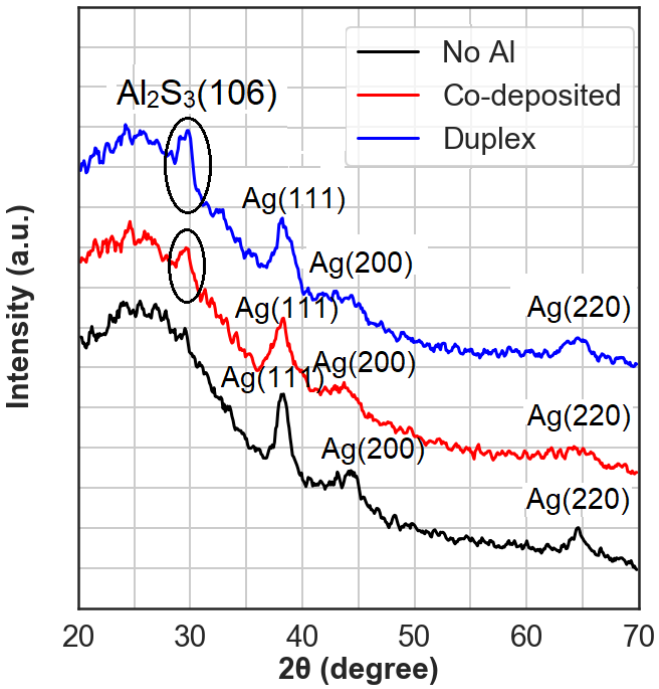

Figure 4.26: XRD patterns of the three degraded films: no Al added, co-deposited, and duplex films 1 year after deposition. The aluminum sulfide peak (106) is found in aluminum added films. The peak is higher in duplex film meaning that aluminum protect silver by cathodic mechanism more effectively in duplex film than the co-deposited one

alumina, and aluminum sulfide [58]. However, XRD only detected an additional peak around 30°, which appears to be related to Al_2S_3 as aluminum sulfide has the peak (106) at the 2θ of 30 degrees [59, 60]. The intensities of the other Al_2S_3 and Al_2O_3 XRD peaks might be at the noise level. Although this research aims to validate that an ultra-thin Al cap layer can also protect Ag from oxidation, it will be very interesting to clarify the surface chemistry in a future comprehensive study. The aluminum sulfide peak for the duplex film is more intensive than the co-deposited film. The observation is reasonable as in the duplex film, there are more aluminum atoms at the surface to react with H_2S. This result agrees with the longer protection time of the duplex film compared to the co-deposited one. On the other hand, the film without aluminum

added shows no aluminum sulfide peak. Silver sulfide peaks were not detected or distinguished in the XRD patterns as they can convolute with the other peaks and background noise. However, the detrimental effects of hydrogen sulfide (H_2S) on silver film have been well recognized [46].

Figure 4.26 also reveals the crystallinity of deposited films. The duplex film shows a slightly better crystallization compared to the co-deposited film. The higher diffusivity of silver's surface atoms in the absence of aluminum atoms during the silver deposition process helped the

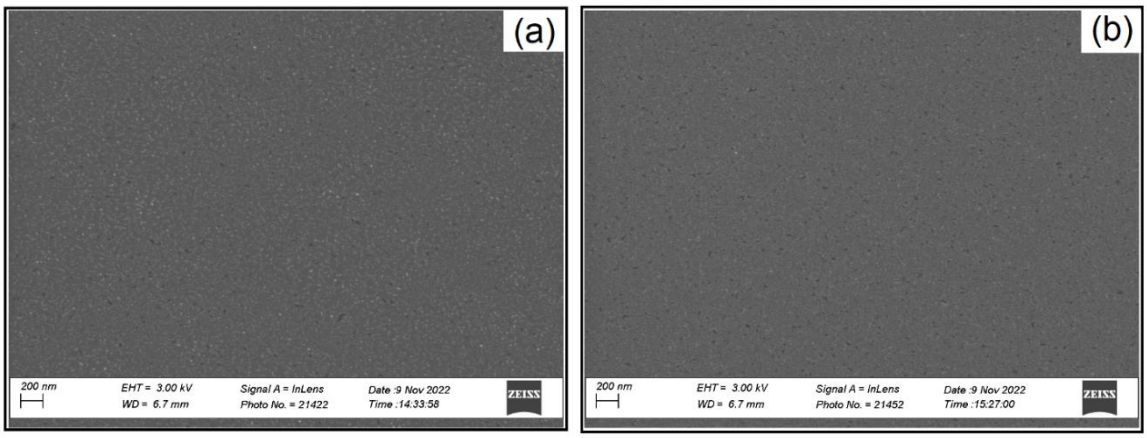

Figure 4.27: SEM images of (a) co-deposited and (b) duplex 7 nm silver film with equivalent global aluminum concentration added: 3% in co-deposited one and 0.2 nm in duplex one

film to crystallize and clump together. This is supported by the fact that the as-deposited duplex film, as shown in **Figure 4.27**, had more pinholes compared to the co- deposited film. The pure silver film shows the best crystallinity as a result of no aluminum incorporated in the silver lattice to prevent the agglomeration or crystallization process.

The stability of the silver films was further studied by annealing them in vacuum at different temperatures. As shown in **Figure 4.28** (c), the transmittance spectra indicate that strong agglomeration occurred in the pure silver film after just one hour of annealing at 100 °C, as evidenced by the concave curve due to plasmonic scattering and the dark appearance. The

agglomeration occurred because of the high mobility of surface atoms at high temperature. The high mobility assisted the agglomeration process to form isolated islands to reduce surface

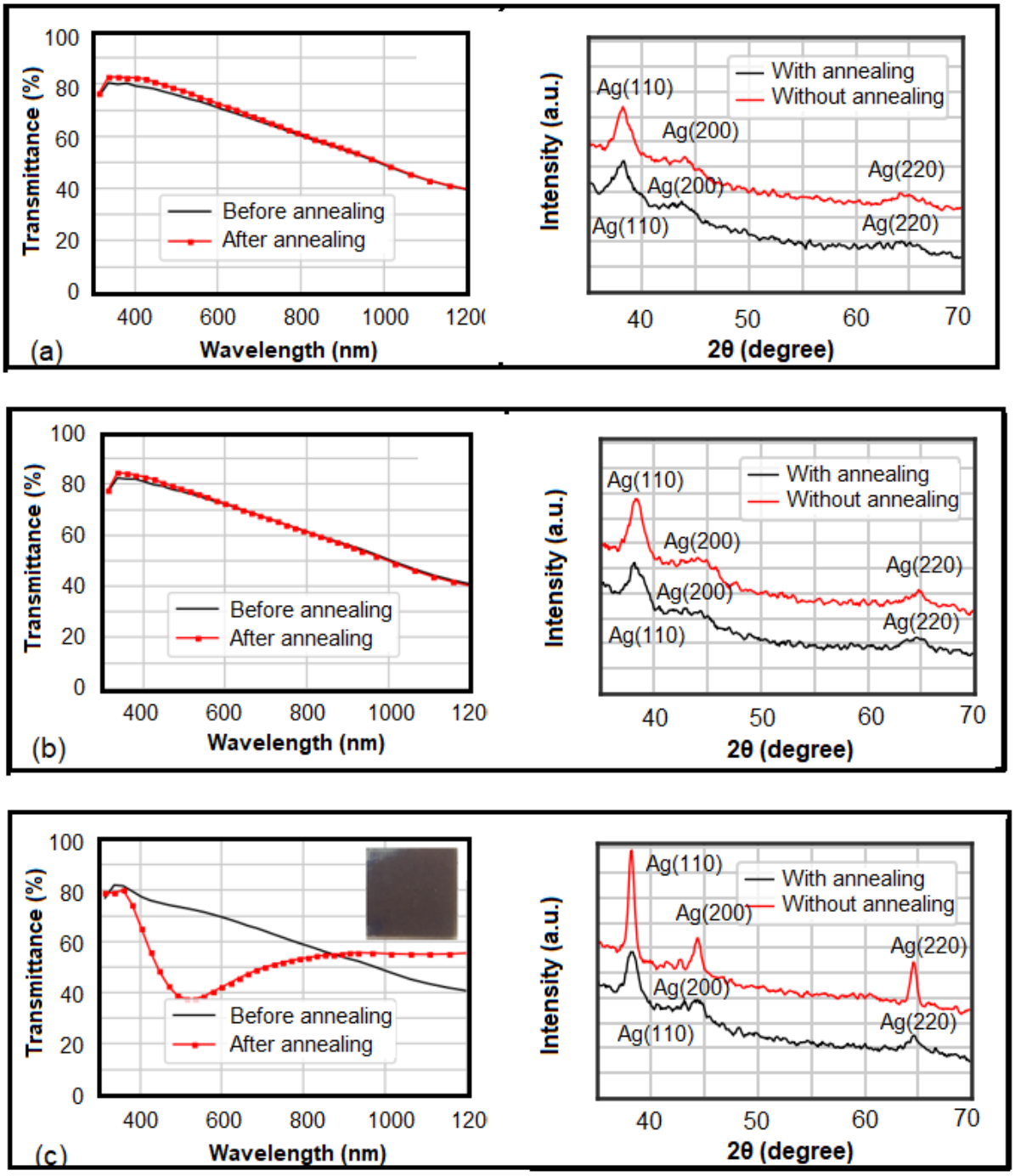

Figure 4.28: Transmission spectra of silver films with a): Al co-deposited b): Al deposited on top and c) without Al added after annealing at 200°C in vacuum and the corresponding XRD patterns

energy and made the film non-conductive. Once the agglomeration occurred in the pure silver film, the sheet resistance dramatically increased beyond the measurement range of the four-point probe (1,000 Ω/□). Consequently, its sheet resistance was not shown in annealing steps of the **Figure 4.30**. In contrast, **Figure 4.28** (a) and (b) shows that the transmittance of the co-deposited and duplex coatings improved slightly after annealing. It is thought that adding aluminum can reduce the mobility of surface silver atoms [61] and slow down silver agglomeration. Alternatively, the bond dissociation energy of Ag-Ag is 162.9 kJ/mol, which is lower than that of Ag-Al at 183.7 kJ/mol [62]. Therefore, aluminum atoms or clusters might act as anchor point for silver atoms and suppress their surface diffusions.

The variation of the sheet resistance of the 7 nm silver films after 10 days being exposed to ambient air is shown in **Figure 4.29**. It clearly shows that the film without aluminum added and the film with aluminum co-deposited is degraded over time due to the agglomeration process happening in the appearance of oxygen. On the other hand, the film with aluminum deposited on top gets better over time. This can be explained by the better crystallization outweighs

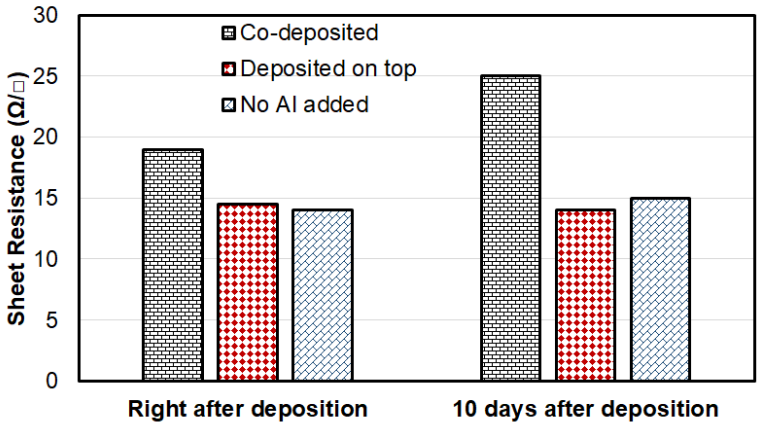

Figure 4.29: Sheet resistance degrading in the ambient environment of 7 nm ion-treated silver films without Al added, with Al co-deposited, and with Al deposited on top

agglomeration. It also means that there was not much agglomeration involved.

The variations in the sheet resistance of the silver films at different annealing conditions are shown in **Figure 4.30**. Annealing in vacuum resulted in a decrease in the sheet resistance of the duplex aluminum/silver and co-deposited silver-aluminum films, indicating that no further agglomerations occurred in these films. This suggests that aluminum can increase the thermal stability of silver films. Furthermore, vacuum annealing can improve the transmission and conductivity of silver films by removing micro voids and improving the crystallinity of the film, which helps to reduce the carrier-scattering defects [63]. The XRD patterns in **Figure 4.28** confirm that annealing results in better crystallinity for the duplex and co-deposited films, as evidenced by more intense and narrow peaks. The lowest sheet resistance of 11 Ω/□, equivalent to 7.7 $\mu\Omega$.cm, was obtained for the duplex film annealed in vacuum at 200°C.

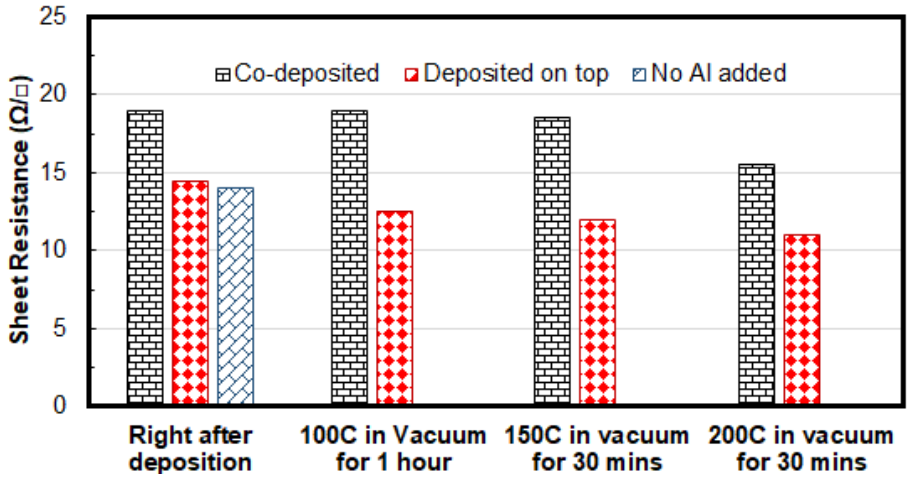

Figure 4.30: Changes of sheet resistance of silver films in annealing tests. The No Al added film became discontinuous after annealing at 100oC in vacuum for 1 hour

Table 4.7 compares the sheet resistance of various ultra-thin silver films and shows that the films produced in this study are among the top performers in terms of sheet resistance. Since our film thickness was reasonably accurate, the comparison of the sheet resistance in Table 1 is meaningful. Furthermore, the smooth change in the sheet resistance of our 6 and 7 nm Ag films implies that the films are continuous in this range and a small error in the thickness would not

affect the sheet resistance significantly. Additionally, the duplex film does not require additional coatings such as ZnO or foreign element-based wetting layers while still exhibiting high thermal and environmental stability.

Table 4.7: Sheet resistance of some silver ultra-thin films reported. The effective thickness is the sum of thickness of silver film and seeding layer. (*)N/A: There is no wetting layer

Film structure	Wetting layer	Effective thickness (nm)	Sheet resistance (Ω/□)	Reference
Ag/Glass	IB-treated Ag	6	15	This work
Ag/Glass	IB-treated Ag	7	11	This work
Ag/Glass	IB-treated Ag	6	19	[37]
Ag/Glass	Al-doped	6	73.9	[5]
Ag/Glass	Ge	6	23	[12]
Ag/Glass	Cu	6	20	[12]
Ag/Glass	N/A (*)	6	>1000	[12]
Ag/SiO_2/Si	Ge	12	20	[10]
Ag/SiO_2/Si	Cu	7	15	[11]
Ag/ZnO/Glass	Ag(O)	6	12.5	[64]
ZnO/Ag(O)/ZnO/PET	Ag(O)	8	27	[16]
Ag/Glass	Al	11	13	[14]

4.2.4 Conclusions

This study presents an effective method for protecting sputter-grown ultra-thin silver film using an extremely thin aluminum cap. The duplex coating consisting of an aluminum cap layer or islands on silver films was found to be superior to co-deposited silver-aluminum binary alloy

films in terms of optical transmittance and electrical conductivity. The effects of various factors on electron scattering in silver films were discussed and correlated to previous research. It was found that the scattering caused by aluminum impurities was significant and outweighed the slight improvement in continuity, leading to the high resistivity of the co-deposited silver-aluminum alloy film. In terms of environmental stability, the aluminum cap layer showed high stability compared to other treatments. The stability is thought to be due to the cathodic protection mechanism, in which aluminum is sacrificed to react with oxidants and form transparent compounds, while the silver is protected by its higher standard electromotive forces until aluminum is used up. The hypothesis is supported by XRD characterization results showing the presence of (106) peak of Al_2S_3 in degraded films having aluminum added. In terms of thermal stability, pure silver films agglomerated in air and at elevated temperatures during annealing tests. In contrast, the aluminum/silver duplex coatings and co-deposited silver-aluminum alloy films showed excellent thermal stability, as indicated by the reduced resistance, increased transmittance, and improved crystallinity after vacuum annealing. This stability is thought to be due to the reduction of surface atoms diffusivity in the presence of aluminum atoms. This technology allows for the fabrication of ultra-thin, stable silver films with high transmittance and low sheet resistance. The resulting 6 nm and 7 nm films had transmittance spectra comparable to simulation results and low sheet resistances of 15 and 11 Ω/□, respectively. These stable, ultra-thin, continuous silver films (6-7 nm) have many potential applications. The method of applying a cap layer of aluminum could be useful not only for ultra-thin silver film, but also for thicker silver films used in applications such as mirroring and silver-based photography.

REFERENCES

[1] Zhang, C., Kinsey, N., Chen, L., Ji, C., Xu, M., Ferrera, M., ... & Guo, L. J. (2017). High-performance doped silver films: overcoming fundamental material limits for nanophotonic applications. *Advanced Materials, 29*(19), 1605177.

[2] Neddermeyer, H. (1990). STM studies of nucleation and the initial stages of film growth. *Critical Reviews in Solid State and Material Sciences, 16*(5), 309-335.

[3] Kundu, S., Hazra, S., Banerjee, S., Sanyal, M. K., Mandal, S. K., Chaudhuri, S., & Pal, A. K. (1998). Morphology of thin silver film grown by dc sputtering on Si (001). *Journal of Physics D: Applied Physics*, *31*(23), L73.

[4] Kikuchi, A., Baba, S., & Kinbara, A. (1985). Measurement of the adhesion of silver films to glass substrates. *Thin Solid Films, 124*(3-4), 343-349.

[5] Gu, D., Zhang, C., Wu, Y. K., & Guo, L. J. (2014). Ultrasmooth and thermally stable silver-based thin films with subnanometer roughness by aluminum doping. *Acs Nano*, *8*(10), 10343-10351.

[6] Thürmer, K., Williams, E. D., & Reutt-Robey, J. E. (2003). Dewetting dynamics of ultrathin silver films on Si (111). *Physical Review B, 68*(15), 155423.

[7] Sharma, S. K., & Spitz, J. (1980). Hillock formation, hole growth and agglomeration in thin silver films. *Thin Solid Films, 65*(3), 339-350.

[8] Chen, W., Thoreson, M. D., Ishii, S., Kildishev, A. V., & Shalaev, V. M. (2010). Ultra-thin ultra-smooth and low-loss silver films on a germanium wetting layer. *Optics express*, *18*(5), 5124-5134.

[9] Zhang, J., Fryauf, D. M., Leon, J. J. D., Garrett, M., Logeeswaran, V. J., Islam, S. M., & Kobayashi, N. P. (2015, September). Deposition and characterizations of ultrasmooth silver thin films assisted with a germanium wetting layer. In *Low-Dimensional Materials and Devices* (Vol. 9553, pp. 136-143). SPIE.

[10] Logeeswaran, V. J., Kobayashi, N. P., Islam, M. S., Wu, W., Chaturvedi, P., Fang, N. X., ... & Williams, R. S. (2009). Ultrasmooth silver thin films deposited with a germanium nucleation layer. *Nano letters, 9*(1), 178-182.

[11] Formica, N., Ghosh, D. S., Carrilero, A., Chen, T. L., Simpson, R. E., & Pruneri, V. (2013). Ultrastable and atomically smooth ultrathin silver films grown on a copper seed layer. *ACS applied materials & interfaces*, *5*(8), 3048-3053.

[12] Park, Y. B., Jeong, C., & Guo, L. J. (2022). Resistivity scaling transition in ultrathin metal film at critical thickness and its implication for the transparent conductor applications. *Advanced Electronic Materials, 8*(3), 2100970.

[13] Liu, H., Wang, B., Leong, E. S., Yang, P., Zong, Y., Si, G., ... & Maier, S. A. (2010). Enhanced surface plasmon resonance on a smooth silver film with a seed growth layer. *ACS nano*, *4*(6), 3139-3146.

[14] Li, D., Pan, Y., Liu, H., Zhang, Y., Zheng, Z., & Zhang, F. (2022). Study on Ultrathin Silver Film Transparent Electrodes Based on Aluminum Seed Layers with Different Structures. *Nanomaterials*, *12*(19), 3540.

[15] Zhao, G., Shen, W., Jeong, E., Lee, S. G., Yu, S. M., Bae, T. S., ... & Yun, J. (2018). Ultrathin silver film electrodes with ultralow optical and electrical losses for flexible organic photovoltaics. *ACS applied materials & interfaces*, *10*(32), 27510-27520.

[16] Wang, W., Song, M., Bae, T. S., Park, Y. H., Kang, Y. C., Lee, S. G., ... & Yun, J. (2014). Transparent ultrathin oxygen-doped silver electrodes for flexible organic solar cells. *Advanced Functional Materials*, *24*(11), 1551-1561.

[17] Pierson, J. F., Wiederkehr, D., & Billard, A. (2005). Reactive magnetron sputtering of copper, silver, and gold. *Thin Solid Films*, *478*(1-2), 196-205.

[18] Al-Kuhaili, M. F. (2007). Characterization of thin films produced by the thermal evaporation of silver oxide. *Journal of Physics D: Applied Physics*, *40*(9), 2847.

[19] Goetz, S., Bauch, M., Dimopoulos, T., & Trassl, S. (2020). Ultrathin sputter-deposited plasmonic silver nanostructures. *Nanoscale Advances*, *2*(2), 869-877.

[20] Mao, F., Taher, M., Kryshtal, O., Kruk, A., Czyrska-Filemonowicz, A., Ottosson, M., ... & Jansson, U. (2016). Combinatorial study of gradient Ag–Al thin films: microstructure, phase formation, mechanical and electrical properties. *ACS Applied Materials & Interfaces*, *8*(44), 30635-30643.

[21] Tran, T., Kim, Y., Baule, N., Shrestha, M., Zheng, B., Wang, K., ... & Fan, Q. H. (2022). Single-beam ion source enhanced growth of transparent conductive thin films. *Journal of Physics D: Applied Physics*, *55*(39), 395202.

[22] Fan, Q. H., Schuelke, T., Haubold, L., & Petzold, M. (2021). *U.S. Patent No. 11,049,697*. Washington, DC: U.S. Patent and Trademark Office.

[23] Marechal, N., Quesnel, E. A., & Pauleau, Y. (1994). Silver thin films deposited by magnetron sputtering. *Thin solid films*, *241*(1-2), 34-38.

[24] Byrnes, S. J. (2016). Multilayer optical calculations. *arXiv preprint arXiv:1603.02720*.

[25] Katsidis, C. C., & Siapkas, D. I. (2002). General transfer-matrix method for optical multilayer systems with coherent, partially coherent, and incoherent interference. *Applied optics*, *41*(19), 3978-3987.

[26] Johnson, P. B., & Christy, R. W. (1972). Optical constants of the noble metals. *Physical review B*, *6*(12), 4370.

[27] Bouroushian, M., & Kosanovic, T. (2012). Characterization of thin films by low incidence X-ray diffraction. *Cryst. Struct. Theory Appl*, *1*(3), 35-39.

[28] Hyett, G., Green, M., & Parkin, I. P. (2006). X-ray diffraction area mapping of preferred orientation and phase change in TiO2 thin films deposited by chemical vapor deposition. *Journal of the American Chemical Society*, *128*(37), 12147-12155.

[29] Hu, Y., Zhu, J., Zhang, C., Yang, W., Fu, L., Li, D., & Zhou, L. (2019). Understanding the preferred crystal orientation of sputtered silver in Ar/N 2 atmosphere: a microstructure investigation. *Advances in Materials Science and Engineering*, *2019*.

[30] Tran, R., Xu, Z., Radhakrishnan, B., Winston, D., Sun, W., Persson, K. A., & Ong, S. P. (2016). Surface energies of elemental crystals. *Scientific data*, *3*(1), 1-13.

[31] Poletaev, G. M., Kaygorodova, V. M., Elli, G. A., Uzhakina, O. M., & Baimova, J. A. (2014). Research of the atomic clusters diffusion over the (111) and (100) surfaces of Ni crystal. *Letters on Materials*, *4*(4), 218-221.

[32] Lim, S. H., & Kim, H. K. (2020). Deposition rate effect on optical and electrical properties of thermally evaporated WO3− x/Ag/WO3− x multilayer electrode for transparent and flexible thin film heaters. *Scientific Reports*, 10(1), 8357.

[33] Cattin, L., Lare, Y., Makha, M., Fleury, M., Chandezon, F., Abachi, T., ... & Bernède, J. C. (2013). Effect of the Ag deposition rate on the properties of conductive transparent MoO3/Ag/MoO3 multilayers. *Solar energy materials and solar cells*, 117, 103-109.

[34] Gong, J., Dai, R., Wang, Z., & Zhang, Z. (2015). Thickness dispersion of surface plasmon of Ag nano-thin films: Determination by ellipsometry iterated with transmittance method. *Scientific reports*, *5*(1), 9279.

[35] Jelle, B. P., Kalnæs, S. E., & Gao, T. (2015). Low-emissivity materials for building applications: A state-of-the-art review and future research perspectives. *Energy and Buildings*, *96*, 329-356.

[36] Matula, R. A. (1979). Electrical resistivity of copper, gold, palladium, and silver. *Journal of Physical and Chemical Reference Data*, *8*(4), 1147-1298.

[37] Thanh, T., Xiaobo, W., Maheshwar, S., Keliang, W., & Qi, H. F. (2023) Ultra-thin silver films grown by sputtering with a soft ion beam-treated intermediate layer. *Journal of Physics D: Applied Physics*.

[38] Abe, Y., & Nakayama, T. (2007). Transparent conductive film having sandwich structure of gallium–indium-oxide/silver/gallium–indium-oxide. *Materials letters*, *61*(18), 3897-3900.

[39] Ren, N., Zhu, J., & Ban, S. (2017). Highly transparent conductive ITO/Ag/ITO trilayer films deposited by RF sputtering at room temperature. *AIP Advances*, *7*(5), 055009.

[40] Sibin, K. P., Srinivas, G., Shashikala, H. D., Dey, A., Sridhara, N., Sharma, A. K., & Barshilia, H. C. (2017). Highly transparent and conducting ITO/Ag/ITO multilayer thin films on FEP substrates for flexible electronics applications. *Solar Energy Materials and Solar Cells*, *172*, 277-284.

[41] Blaber, M. G., Arnold, M. D., & Ford, M. J. (2010). A review of the optical properties of alloys and intermetallics for plasmonics. *Journal of Physics: Condensed Matter*, *22*(14), 143201.

[42] Im, H., Lee, S. H., Wittenberg, N. J., Johnson, T. W., Lindquist, N. C., Nagpal, P., ... & Oh, S. H. (2011). Template-stripped smooth Ag nanohole arrays with silica shells for surface plasmon resonance biosensing. *Acs Nano*, *5*(8), 6244-6253.

[43] Sennett, R. S., & Scott, G. D. (1950). The structure of evaporated metal films and their optical properties. *Josa*, *40*(4), 203-211.

[44] Kim, H. C., Alford, T. L., & Allee, D. R. (2002). Thickness dependence on the thermal stability of silver thin films. *Applied physics letters*, *81*(22), 4287-4289.

[45] Hafezian, S., Beaini, R., Martinu, L., & Kena-Cohen, S. (2019). Degradation mechanism of protected ultrathin silver films and the effect of the seed layer. *Applied Surface Science*, *484*, 335-340.

[46] Di Pietro, G. (2002). *Silver mirroring on silver gelatin glass negatives* (Doctoral dissertation, University_of_Basel).

[47] Sasaki, Y., Kawamura, M., Kiba, T., Abe, Y., Kim, K. H., & Murotani, H. (2020). Improved durability of Ag thin films under high humidity environment by deposition of surface Al nanolayer. *Applied Surface Science*, *506*, 144929.

[48] Dugdale, J. S., & Basinski, Z. S. (1967). Mathiessen's rule and anisotropic relaxation times. *Physical Review*, *157*(3), 552.

[49] Wu, Y., Zhang, C., Estakhri, N. M., Zhao, Y., Kim, J., Zhang, M., ... & Li, X. (2014). Intrinsic optical properties and enhanced plasmonic response of epitaxial silver. *Advanced Materials*, *26*(35), 6106-6110.

[50] Zhou, T., & Gall, D. (2018). Resistivity scaling due to electron surface scattering in thin metal layers. *Physical Review B*, *97*(16), 165406.

[51] Andersson, J. O., Helander, T., Höglund, L., Shi, P., & Sundman, B. (2002). Thermo-Calc & DICTRA, computational tools for materials science. *Calphad*, *26*(2), 273-312.

[52] Olmsted, B. A., & Davis, M. E. Principles of Electronic Materials and Devices.

[53] Davey, W. P. (1925). Precision measurements of the lattice constants of twelve common metals. *Physical Review*, *25*(6), 753.

[54] Batchelder, D. N., & Simmons, R. O. (1965). X-Ray Lattice Constants of Crystals by a Rotating-Camera Method: Al, Ar, Au, CaF2, Cu, Ge, Ne, Si. *Journal of Applied Physics*, *36*(9), 2864-2868.

[55] Henn, R. W., & Wiest, D. G. (1963). Microscopic spots in processed microfilm: their nature and prevention. *Photographic science and engineering*, *7*(5), 253-261.

[56] Mohamed Hendy, Reham Tarek, Rasha Shaheen, Enrico Ciliberto, "Aluminum foil as cathodic protector to prevent silver mirroring," 2021. [Online]. Available: https://www.culturalheritage.org/docs/default-source/publications/annualmeeting/2021-posters/aluminum-foil-as-cathodic-protector-to-prevent-silver-mirroring--mohamed-hendy.pdf?sfvrsn=a2211420_7.

[57] Pedeferri, P., & Pedeferri, P. (2018). Galvanic corrosion. *Corrosion Science and Engineering*, 183-206.

[58] Cao, X., Lu, Y., Wang, Z., Wei, H., Fan, L., Yang, R., & Guo, W. (2023). Corrosion behavior of aluminum alloy in sulfur-associated petrochemical equipment H_2S environment. *Chemical Engineering Communications*, *210*(2), 233-246.

[59] Yoon, I. S., Kim, C. D., Min, B. K., Kim, Y. K., Kim, B. S., & Jung, W. S. (2009). Characterization of graphene sheets formed by the reaction of carbon monoxide with aluminum sulfide. *Bulletin of the Korean Chemical Society*, *30*(12), 3045-3048.

[60] Akhgar, B. N., & Pourghahramani, P. (2016). Mechanochemical reduction of natural pyrite by aluminum and magnesium. *Journal of Alloys and Compounds*, *657*, 144-151.

[61] Yan, H., Xu, X., Li, P., He, P., Peng, Q., & Ding, C. (2022). Aluminum Doping Effect on Surface Structure of Silver Ultrathin Films. *Materials*, *15*(2), 648.

[62] Haynes, W. M., Lide, D. R., & Bruno, T. J. (2016). Properties of solids. *CRC handbook of chemistry and physics.*

[63] Auer, S., Wan, W., Huang, X., Ramirez, A. G., & Cao, H. (2011). Morphology-induced plasmonic resonances in silver-aluminum alloy thin films. *Applied Physics Letters*, *99*(4), 041116.

[64] Zhao, G., Shen, W., Jeong, E., Lee, S. G., Yu, S. M., Bae, T. S., ... & Yun, J. (2018). Ultrathin silver film electrodes with ultralow optical and electrical losses for flexible organic photovoltaics. *ACS applied materials & interfaces*, *10*(32), 27510-27520.

CHAPTER 5

HIGHLY TRANSPARENT AND CONDUCTIVE OXIDE/ULTRA-THIN SILVER/OXIDE/GLASS SANDWICH STRUCTURE FOR OPTICAL COATINGS AND OPTOELECTRONIC DEVICES

5.1 Highly Transparent and Conductive ITO/Ultra-Thin Silver/ITO/Glass Sandwich Structure for Optical Coatings and Optoelectronic Devices

This part of this chapter is adapted from Thanh Tran, Maheshwar Shrestha and Qi Hua Fan, "*Highly Transparent and Conductive ITO/Ultra-thin Silver/ITO/Glass Sandwich Structure for Optical Coatings and Optoelectronic Devices*", MRS Communication

Publication Date: September 9, 2023

5.1.1 Introduction

Indium tin oxide (ITO) is a widely used transparent conductive oxide (TCO) material in various optoelectronic applications, including liquid crystal displays, touchscreens, and solar cells [1, 2]. It exhibits excellent transparency across a broad spectrum of light ranging from 300 nm to 1200 nm, along with high electrical conductivity, making it an ideal material for such applications. However, due to its ceramic nature, ITO is inherently brittle, which limits its practicality. To overcome this limitation, the implementation of a sandwich structure known as ITO/silver/ITO (IAI) has been explored to enhance the flexibility of the films for use in flexible devices [3]. Moreover, the use of IAI sandwich structure improves transmittance in the visible wavelength range and enhances electrical conductivity compared to standalone ITO films [4]. Silver, with its low product of reflective index, n×k, is an ideal metal for optical applications [5]. Therefore, silver-based sandwich structures have been extensively researched and applied in

low-E glasses, touchscreens, solar cells, organic light-emitting diodes (OLEDs), and electrochromic devices [6, 7].

To utilize IAI sandwich structures in the applications, several challenges need to be addressed. Firstly, when the silver thickness in the IAI sandwich structure exceeds 9 nm, a significant reduction in transmittance occurs at wavelengths beyond 700 nm. To broaden the working window of the transmittance spectrum required for multiple applications, it becomes necessary to use a thinner silver film. Various research studies have explored alternatives such as silver nanowire networks or silver mesh/grids to overcome this issue [8, 9]. However, these methods inherently result in high roughness and low surface-covering ratios, making them unsuitable for certain applications, particularly in solar cells. Moreover, the fabrication of these silver forms is often complex and costly. The second challenge pertains to the thermal and environmental stability of the silver film. Silver layers are prone to oxidation and corrosion, which can significantly impact the optical and electrical performance of the film.

In this study, we incorporate our silver deposition technique for fabricating the IAI sandwich structure on a glass substrate [10, 11]. Our technique enables the deposition of stable continuous silver films as thin as 6 nm. Due to the reported high stability of these silver films, we anticipate that the resulting sandwich structure will exhibit excellent stability in ambient environments and at high temperatures, while maintaining exceptional optical and electrical properties. The high thermal stability also allows for annealing at elevated temperatures in vacuum and in the air, which is expected to further improve the film's quality [12].

5.1.2 Experiment and Method

The sandwich structure design is illustrated in **Figure 5.1**, which consists of a borosilicate glass substrate with a thickness of approximately 0.5 mm. The bottom layer is a

thickness-optimized ITO layer. The next layer is a 1 nm ion beam-treated silver layer, aimed at improving the wettability of the silver film for depositing ultra-thin layers below 9 nm [10]. Conventional sputtering is then used to deposit the silver layer with a thickness of (X-1-0.2) nm, where X represents the overall thickness of the silver layer in further communications. Following the silver layer, there is an aluminum cap layer with a thickness of 0.2 nm serving multiple purposes. It acts as an anode in cathodic protection to protect the silver from oxidation and enhances the thermal stability of the silver film by reducing the mobility of surface atoms [11]. Additionally, the aluminum cap layer protects the silver layer during the deposition of the top ITO layer. During the ITO deposition, oxygen is introduced into the chamber, and the aluminum cap layer ensures the stability of the silver film, preventing agglomeration triggered due to high mobility of surface atoms in the appearance of oxygen [13]. The presence of aluminum atoms and clusters restricts the mobility of silver surface atoms and prevents further agglomeration of

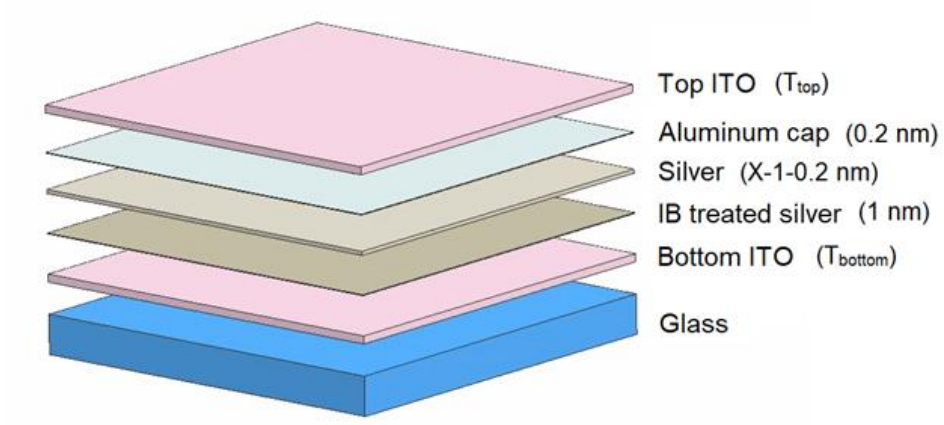

Figure 5.1: Configuration of the sandwich structure

the silver film [11]. The top layer in the sandwich structure is also a thickness-optimized ITO layer.

In the experiments, the borosilicate glass substrate was cut into 1x1 inch-squared pieces (6.45 cm^2). The substrate underwent cleaning in acetone and methanol using an ultrasonic bath,

followed by baking at 100°C for 30 minutes before deposition. The sputtering system (Kurt J. Lesker Company® PVD 75 PRO Line) employed multiple sputtering magnetrons, with each magnetron equipped with a shutter for pre-sputtering to clean the target surface. For depositing the silver intermediate layer, a single beam ion source (SPR-10, Scion Plasma LLC) was integrated into the sputtering system, as depicted in our reported works [14].

Table 5.1: Processing conditions of sputtered layers

	IB pretreatment	**ITO (bottom and top)**	**Silver**	**Aluminum**
Target		97 wt%In_2O_3 + 3 wt%SnO_2	Silver 99.99% purity	Aluminum 99.99% purity
Target diameter		76.2 mm (3 inches)	76.2 mm (3 inches)	76.2 mm (3 inches)
Based pressure	1.3×10^{-4} Pa	1.3×10^{-4} Pa	1.3×10^{-4} Pa	1.3×10^{-4} Pa
Processing pressure	2 Pa	0.67 Pa	0.4 Pa	0.4 Pa
Processing gases	Argon (99.99%)	Argon/O_2 (98.5/1.5)	Argon (99.99 %)	Argon (99.99%)
Discharge power	100 W	60 W	97 W	10 W
Deposition temperature	Room temperature	Room temperature	Room temperature	Room temperature
Deposition technique	Ion beam pretreatment	DC magnetron sputtering	RF magnetron sputtering	DC magnetron sputtering

The processing parameters for these layers are summarized in **Table 5.1**. The vacuum chamber was initially pumped down to a base pressure of 1.33E-4 Pa. Ultra-high purity grade (99.999%) argon gas was used as the sputtering gas. The sputtering/processing pressure was maintained at 0.4 Pa for pure silver and aluminum depositions, while it was set at 2 Pa during the

ion beam pre-treatment process and 0.67 Pa for ITO deposition. During silver deposition, an RF power of 97 W was applied, resulting in a deposition rate of approximately 0.32 nm/s. Aluminum deposition was conducted at a DC power of 10 W for 18 seconds, resulting in a deposition rate of approximately 0.011 nm/s. For ITO deposition, the same deposition recipe was used for both bottom and top layers. An oxygen percentage of 1.5% was chosen to achieve good transmittance (**Figure 5.2**), and the ITO deposition rate was approximately 12 nm/min. The substrate holder rotated at a constant speed of 10 rpm during the deposition process, and all depositions were performed at room temperature.

In this study, the deposition rate and deposition time were parameters used to control the thickness of the films, as elaborated in our previous works [10, 11]. Optical transmittance measurements were performed using a spectrophotometer (F20 thin-film measurement system, KLA Instruments). The sheet resistance of the films was characterized using a four-point probe sheet resistivity meter (SRM-232-1000, Guardian Manufacturing) with a range of 0-1000 Ω/□, a resolution of 0.4 Ω/□, and an accuracy of 0.7 Ω/□ at 100 Ω. GAXRD (Glancing Angle X-Ray Diffraction [15]) characterization was carried out using an X-Ray diffractometer (SmartLab, Rigaku) with a small incident angle of 2° and Cu Kα radiation (wavelength approximately 1.54 Å).To optimize the design of the sandwich structure, we employed global scanning of transmittance as presented in our recent work [16]. The method can optimize the structure for various conditions, including specific wavelength value/range or even across a random profile, such as the solar spectrum (AM 1.5-G). In this paper, the optimization focused on the average transmittance in the 400-800 nm range ($T_{\_avg\ 400\text{-}800}$). The transmittance of the multi-layer optical structures, consisting of four layers as shown in **Figure 5.3**, was computed using the transfer matrix method [17, 18]. The refractive index values used were obtained from Johnson and

Christy for silver [5], SCHOTT Zemax catalog 2017-01-20b for glass, and König et al. 2014 for ITO [19]. In the simulation, various thicknesses of silver were considered. A scanning process was conducted over the thickness of the top and bottom ITO layers, ranging from 0 to 100 nm with a step size of 5 nm, in order to obtain the transmittance data for further analysis. It is worth

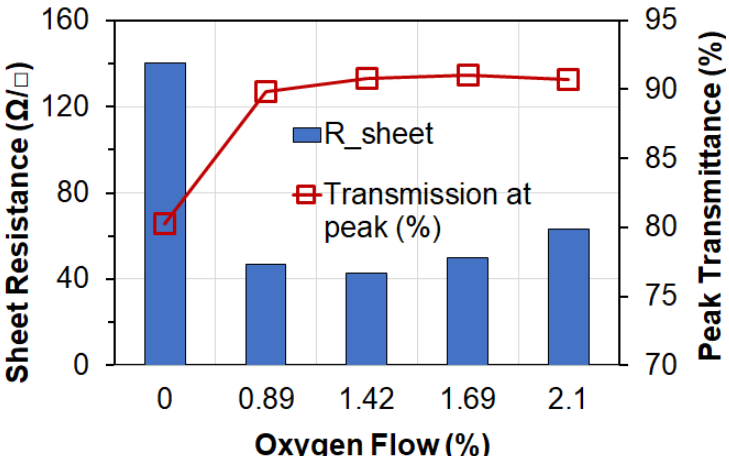

Figure 5.2: Optical and electrical performances of ITO films as functions of oxygen flow

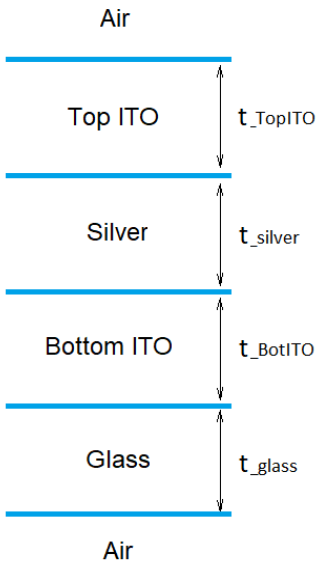

Figure 5.3: The simplified IAI sandwich structure used for simulation

noting that in practical applications, to optimize real structures, the reflective index of the films is needed to be measured experimentally to be used as inputs for the calculation. For metal ultra-thin films, getting reflective index can be challenging and was discussed by Zhang et. al. [20].

5.1.3 Results and Discussion

Figure 5.4 (a) presents contour maps displaying $T_{avg\ 400\text{-}800}$ for varying thicknesses of the silver layer, taking into account the matrix of ITO top and bottom thicknesses. The maps demonstrate a consistent trend: as the silver layer thickness increases, both the overall average

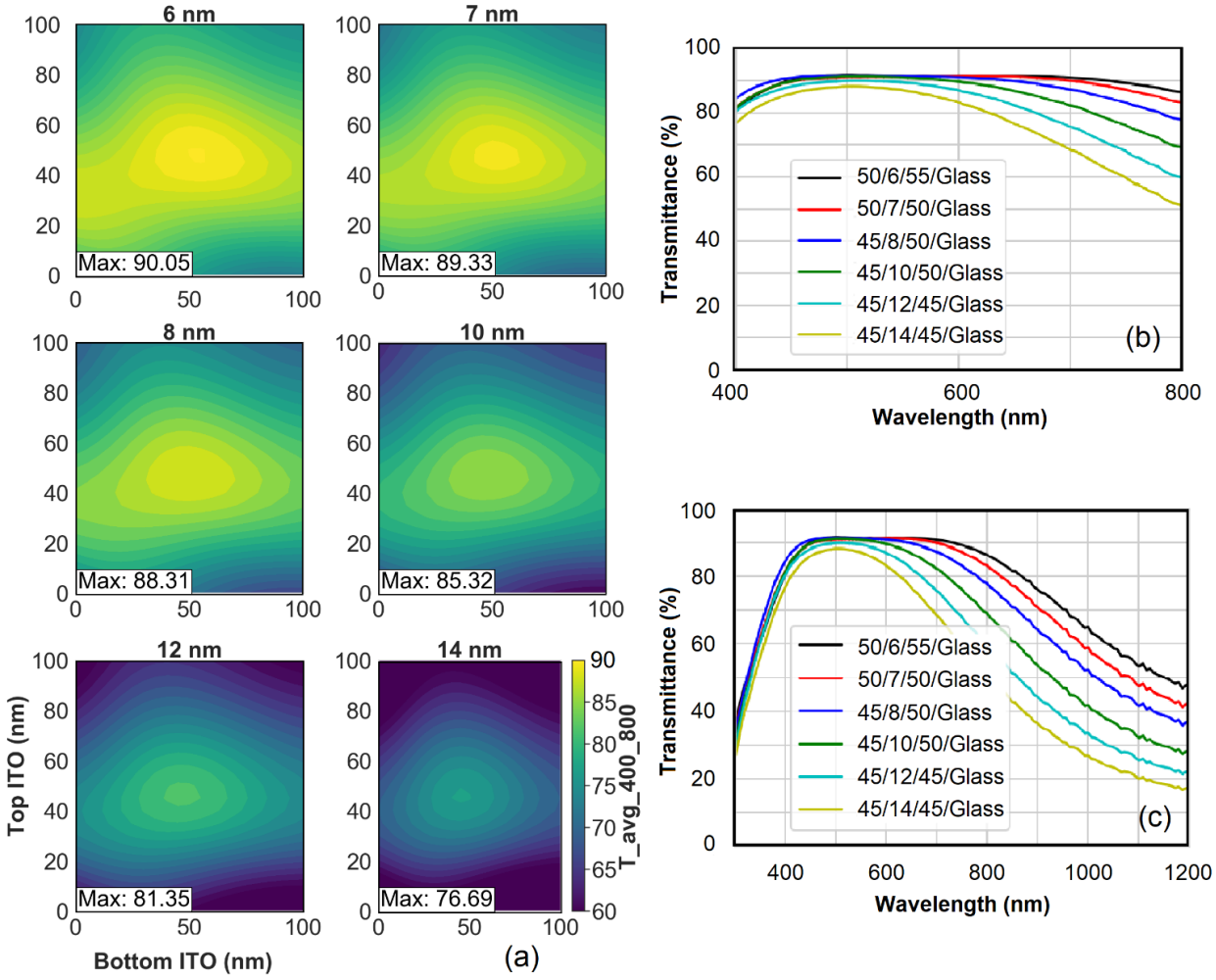

Figure 5.4: (a) Contour maps of average transmittance in the wavelength range of 400 nm-800 nm as a function of thicknesses of bottom and top ITO layers at various thicknesses of silver layer. The transmittance spectra of optimal structure in (b) 400-800 nm range and 300-1200 nm range

transmittance and the optimum average transmittance decrease. For instance, when the silver layer thickness is 6 nm, the optimal $T_{avg\ 400\text{-}800}$ reaches 90.05%. However, when the silver layer thickness increases to 14 nm, the corresponding transmittance drops to only 76.69%.

Figure 5.4 (b) and (c) display the transmittance spectra of optimal structures for each silver thickness in 400 nm-800 nm and 300 nm-1200 nm wavelength ranges, respectively. These

spectra reveal that the optimal design consists of a bottom ITO layer with a thickness of approximately 50 nm and a top ITO layer with a thickness of around 45 nm. Additionally, it is observed that as the thickness of the silver layer increases, the transmittance decreases more rapidly in the longer wavelength region as mentioned in the introduction.

Guided from the above simulation results, real IAI sandwich structures were fabricated using the configuration ITO (45 nm)/ Ag (X nm)/ ITO (50 nm)/ glass, where X represents the thickness of silver layer (chosen as 6, 7, 8, and 9 nm). These structures were then compared with the simulation results of the same configurations as depicted in **Table 5.2**.

Figure 5.5 (d) presents the XRD patterns of an ITO (45 nm)/Ag (6 nm)/ ITO (50 nm)/ glass structure in three different scenarios: as deposited, annealed in vacuum at 200°C, and annealed in air at 200°C for 1 hour. The as-deposited film exhibited poor crystallinity in the ITO layers with a dominant crystal orientation of (400). In the sample annealed in vacuum at 200°C, the crystallinity of ITO layers improved, while the dominant orientation remained (400). In the sample annealed in air at 200°C, the film's crystallinity of layers was further enhanced, comparable to the vacuum annealing. However, a significant difference in crystal orientation was observed. The dominant crystal orientation shifted from (400) to (222).

Notably, in the air-annealed sample, a strong peak of Ag (200) was observed, indicating the presence of highly crystallized silver ultra-thin layers oriented in the (200) direction. The introduction of oxygen significantly affected the mobility of silver atoms, leading to the formation of highly crystalized films. In conventional silver deposition process, the preferred growing orientation of (111) is influenced by surface energy [21]. However, in the sandwich structure, as there are no free silver film surfaces, the crystal orientation of the annealed silver film is determined by its interaction with the ITO surface. This approach allows for the

preparation of a (100) oriented silver layer tailored for specific applications. For example, (100) oriented silver exhibits improved wettability towards substrate, enabling the formation thinner silver films [10].

Table 5.2: Simulation results of transmittance of sandwich structures ITO (45 nm)/ Ag (X nm)/ ITO (50 nm) in 400-800 range and 300-1200 range calculated in some typical situations for comparison purposes

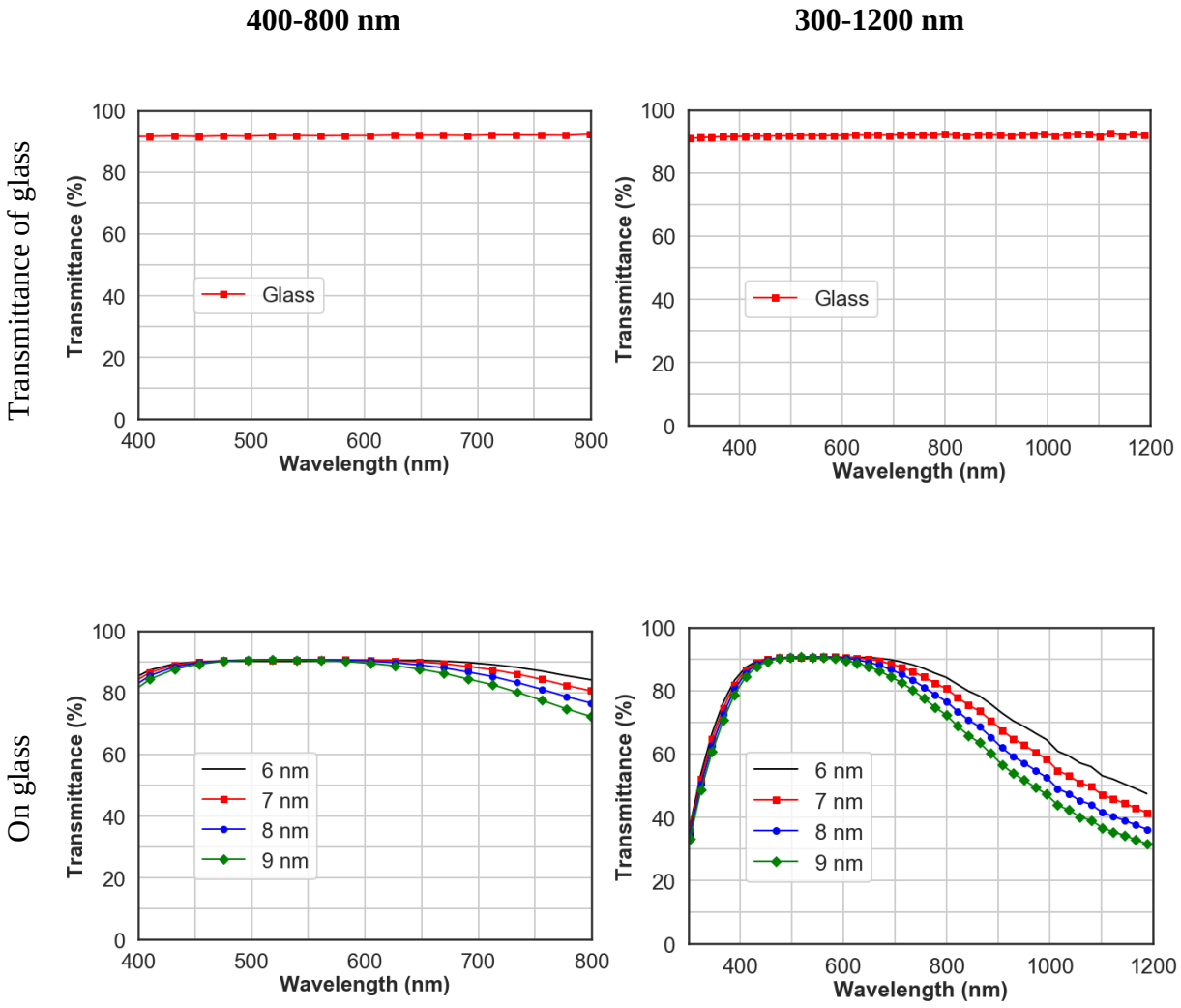

Table 5.2 (cont'd)

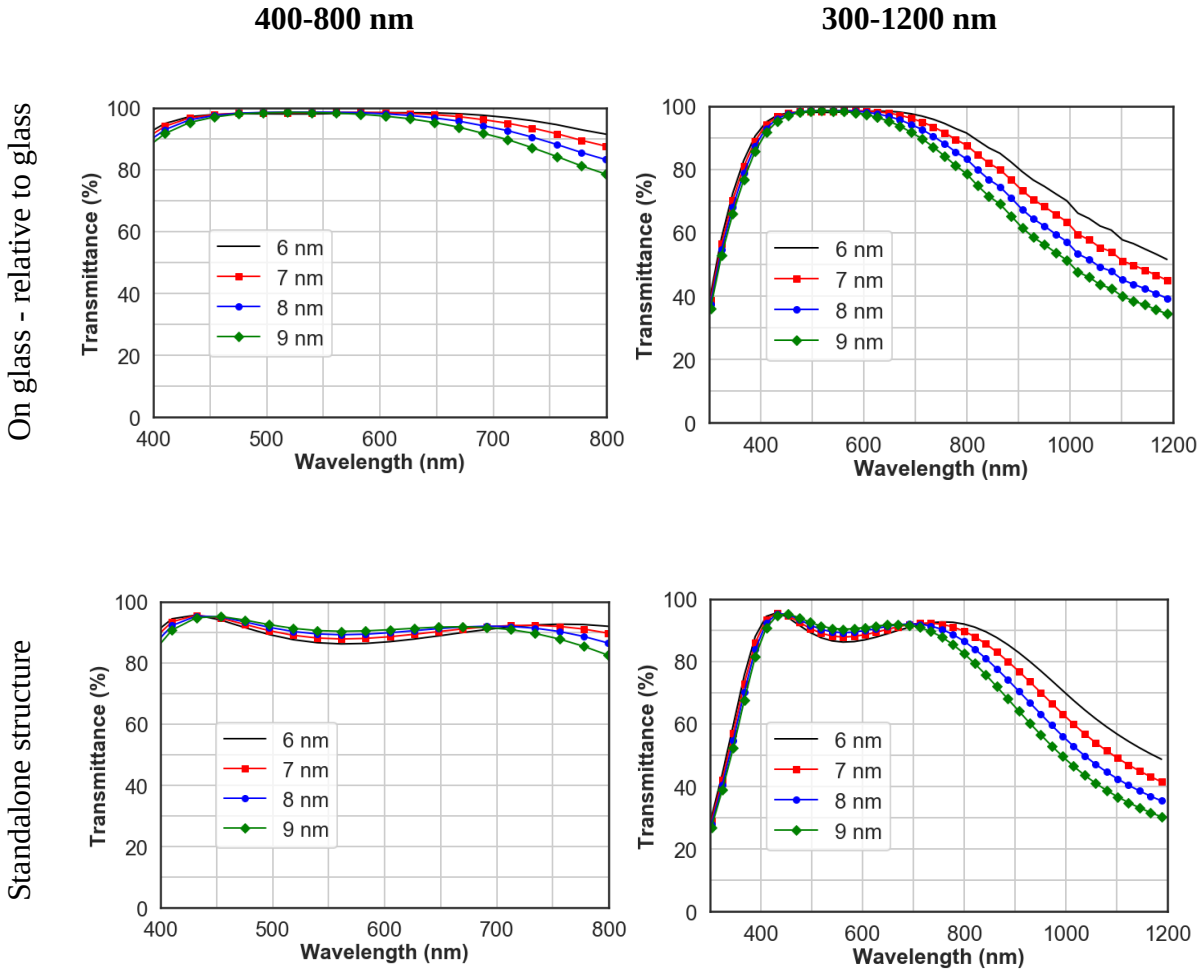

Using the Scherrer equation, $\mathcal{T} = \frac{K\lambda}{\beta \cos\theta}$, where $\mathcal{T}$ is the mean size of the oriented crystal, K is the shape factor (0.9 in this study), λ is the X-ray wavelength (0.154 nm), β is the full width at half maximum (FWHM) in radians, and θ is the Bragg angle, the crystal sizes of the ITO films were calculated to be 20 nm. Similarly, the crystal sizes of silver films were found to be the same as the ITO crystals, measuring 20 nm. This consistent value was observed for structures with silver thicknesses of 7, 8, and 9 nm (**Figure 5.6**). In our previous study, we

reported that a naturally grown silver layer exhibited a crystal size of approximately 6 nm, both with and without an ion beam-treated intermediate layer [10].

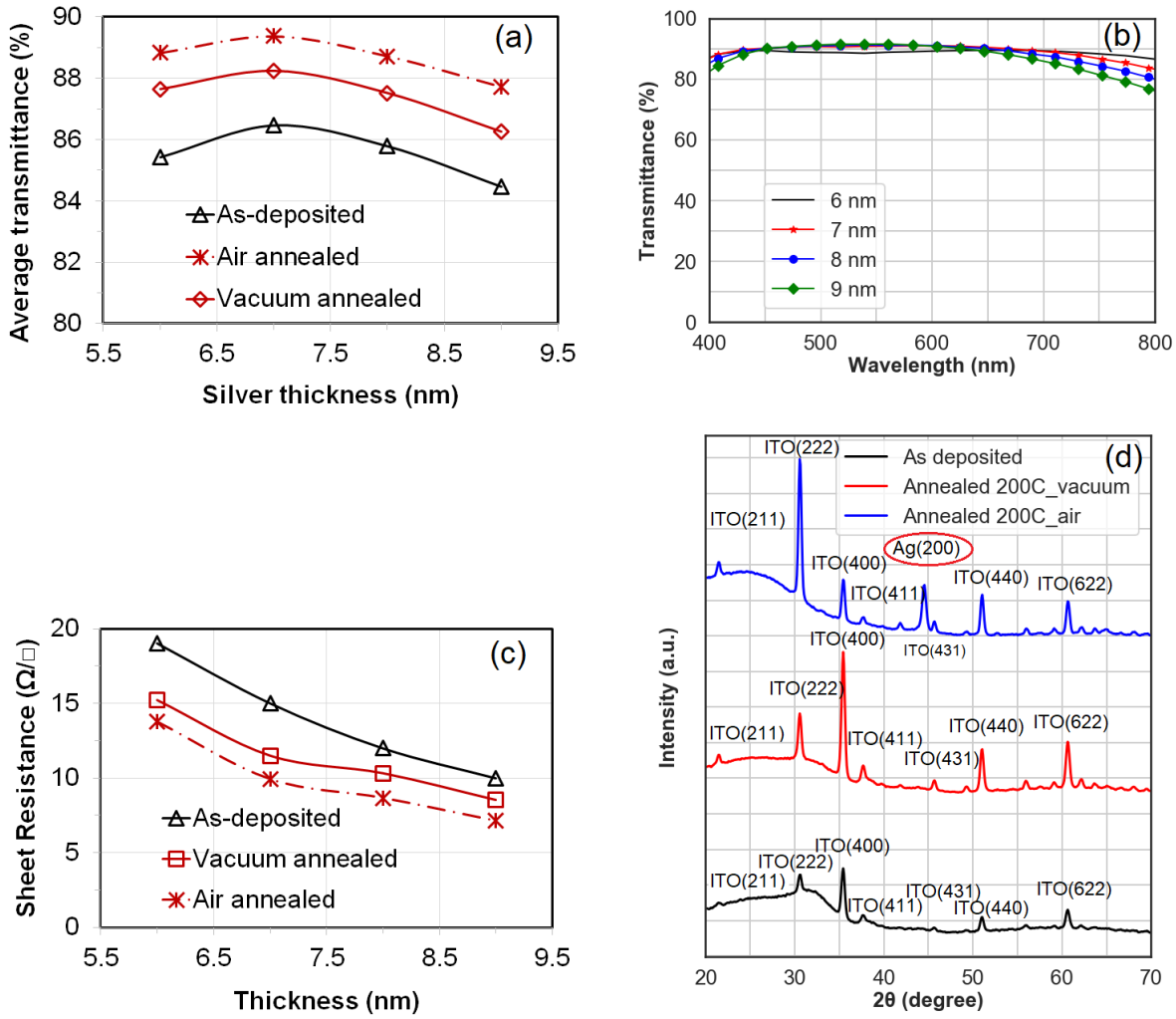

Figure 5.5: (a) Average transmittance in 400-800 nm range of the sandwich structures before and after annealing (b) transmittance spectra of the sandwich structures after being annealed, (c) sheet resistance of the sandwich structures before and after annealing, and (d) XRD patterns of ITO_45 nm/Ag_ 6nm/ITO_50 nm films before and after annealing

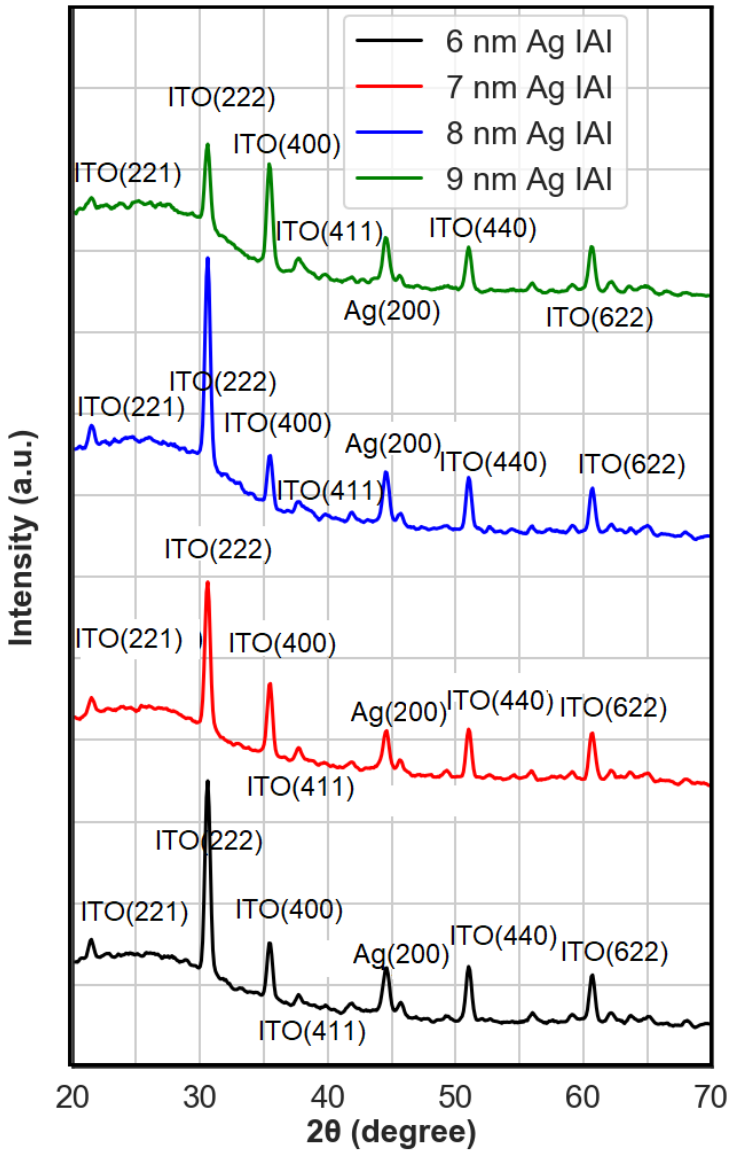

Figure 5.6: XRD patterns of ITO (45 nm)/Ag (X nm)/ ITO (50 nm)/ glass after annealing in the air at 200°C

Figure 5.5 (a) illustrates $T_{\_avg\ 400\text{-}800}$ of sandwich structures with varying thicknesses of the silver layer. The spectra of the as-deposited films are shown in **Figure 5.7**. Upon comparing these spectra with the simulation results in **Table 5.2**, we observe lower transmittance in the short wavelength range. Consequently, the average transmittance of the as-deposited films was

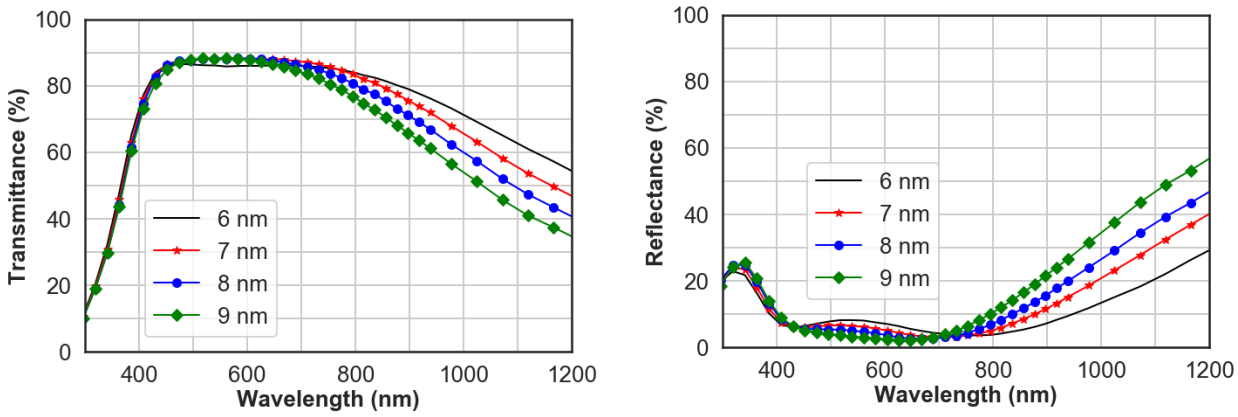

Figure 5.7: Transmittance and reflectance of as-deposited sandwich structures in 300-1200 range

relatively low compared to the annealed samples. This outcome was expected since the depositions were conducted at room temperature. As demonstrated in **Figure 5.8**, at room temperature, the transmittance of ITO is lower than that predicted by the simulation, particularly in the short wavelength region.

After annealing, the transmittance notably increased, particularly when annealed in air at 200°C, as shown in **Figure 5.5** (a) and (b). Transmittance improved in both the long and short wavelength ranges, resulting from enhancements in the transmittance of both the ITO and silver layer. **Figure 5.8** shows the improvement of transmittance of ITO film after annealing in the air. This is due to the enhanced crystallinity as shown in the **Figure 5.5** (d). The maximum transmittance reached 91.5% at a wavelength of 500 nm and the maximum average transmittance was 89.4%, equivalent to 96 % relatively to glass substrate, when the thickness of silver was 7 nm. These transmittance spectra agree well with the simulation results shown in **Table 5.2**. The enhancement of transmittance spectra is accompanied by an improvement in electrical conductivity. **Figure 5.5** (c) illustrates the sheet resistance of the sandwich structures before and after annealing. After annealing in vacuum at 200°C, the sheet resistances of the stacks improved

due to the enhanced crystallinity of the silver layer. This finding aligns with the annealing results of standalone silver films reported in our reported work [11]. Annealing in air further improved crystallinity of silver layer and consequently the sheet resistance of the sandwich structures, evidenced by the XRD patterns shown in **Figure 5.5** (d). Gong et al. calculated the mean free path of electrons in silver to be 53.3 nm [22]. Therefore, when the crystal size is smaller than 53.3 nm, grain boundaries have a significant impact on electron scattering. Increasing the crystal size diminishes electron scattering at boundaries and greatly enhances electrical conductivity. As a result, we observed a further decrease in the sheet resistance of the sandwich structures after annealing in air at 200°C for 1 hour, as shown in **Figure 5.5** (c). The clear peaks of ITO and Ag(200) one after annealing in the air, good agreement between simulation and experimental results of transmittance spectra, and enhancement of sheet resistance indicate that the layers are well defined after annealing without significant interdiffusion between layers.

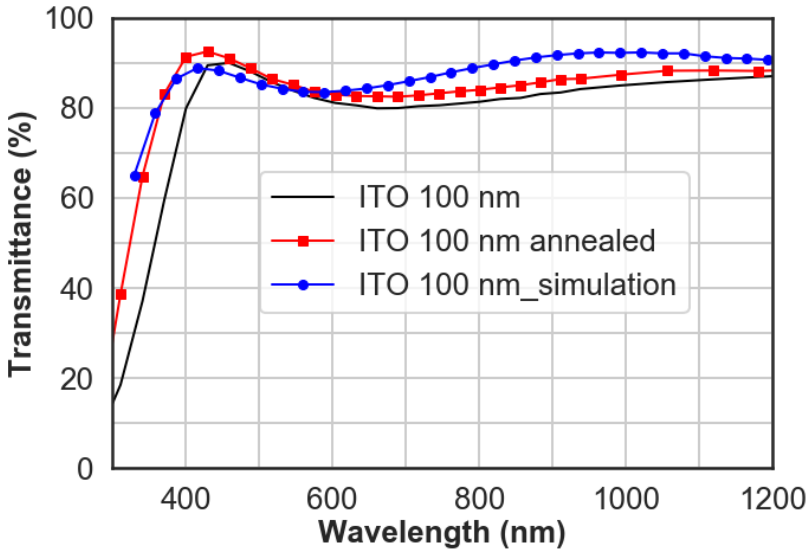

Figure 5.8: Comparing ITO as deposited, annealed in air, and simulation result

Figure 5.9 (a) presents $T_{\_avg\ 400\text{-}800}$ and $T_{\_avg\ 800\text{-}1200}$ together with maximum transmittance in the 400-800 nm range of the sandwich structures. For comparison purposes, **Figure 5.9** (b) shows these transmittances calculated relatively to the transmittance of the glass substrate. **Figure 5.9** (c) illustrates the Haccke Figure of Merit (FoM) of the sandwich structures after annealing in air at 200°C for 1 hour [23]. It demonstrates that as the thickness of the silver film increases, the FoM also increases due to the lower sheet resistance out weighting the decreasing of transmittance. The highest FoM achieved was $77 \times 10^{-3}\Omega^{-1}$ at the silver thickness of 9 nm. Further increases in the thickness of the silver layer are likely to yield even higher FoM values. **Table 5.3** compares FoM of the sandwich structures in this study with those reported in other studies. In the calculation, the transmittance used is the average transmittance in the 400-800 nm range and it is relative to the corresponding substrates. The results indicate that the sandwich structure in this study exhibits outstanding FoM values. This achievement is again attributed to the optimization process, ultra-thin silver deposition technique, and the impact of annealing on the optical and electrical performance of the sandwich structures.

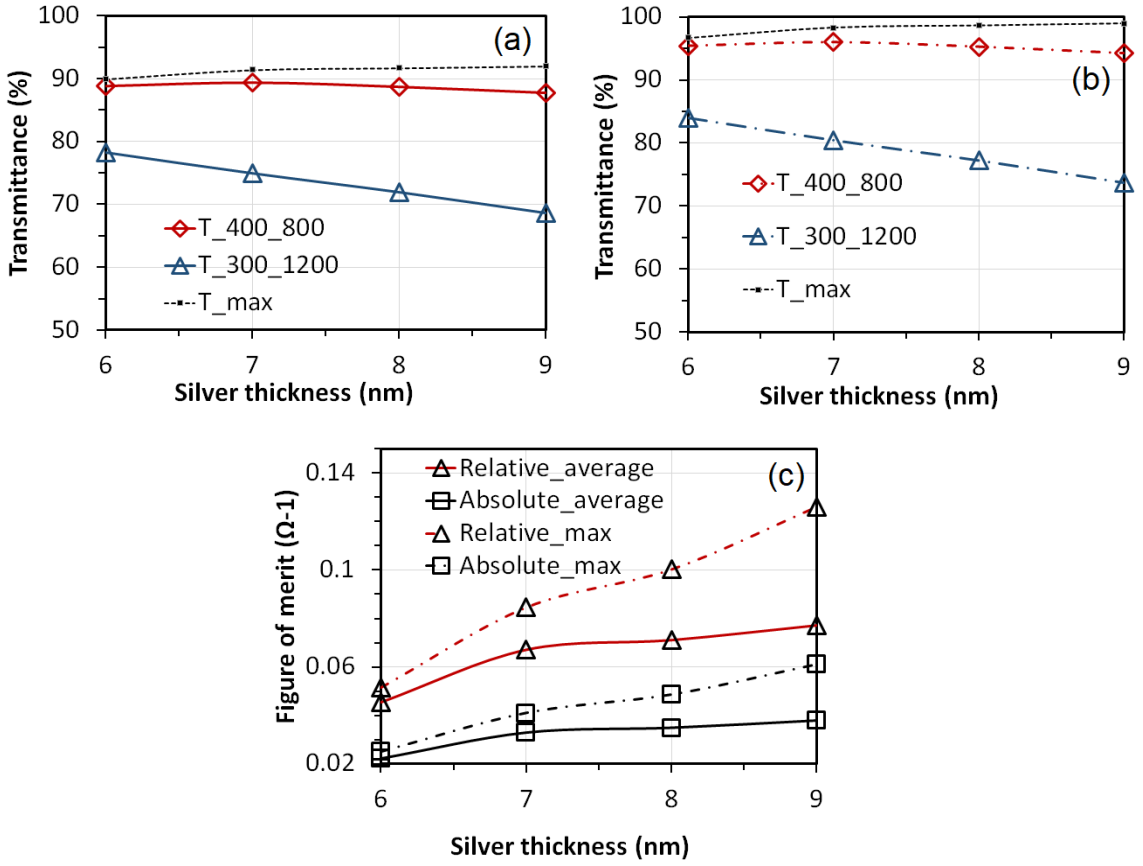

Figure 5.9: (a) absolute and (b) relative-to-glass average transmittance in two ranges 400nm-800nm and 300nm-1200nm, and maximum transmittance of the ITO_45/Ag_x/ITO_50/glass sandwich structures as function of thickness of silver layer. (c) Figure merits of sandwich structures. Transmittance is calculated in several ways for comparison purpose: "Relative": relative to glass substrate, "Absolute": relative to the air, "average": average transmittance in 400-800 nm range, and "max": maximum transmittance in the 400-800 nm range

Table 5.3: Figure of Merit of some sandwich structures reported. [(a)] The transmittance is relative to transmittance of substrate. [(b)]NA: no deposition method specified

Structure	Silver (nm)	$R_{\_sheet}$ (ohm/sq.)	$T_{\_avg\ (400\text{-}800)}$ (%) [(a)]	FoM [23] ($10^{-3}\Omega^{-1}$)	Method	Reference
ITO/Ag/ITO/glass	7	9.94	96	67	Sputtering	This work
ITO/Ag/ITO/glass	9	7.13	94.2	77	Sputtering	This work
ITO/Ag/ITO/PET	10	6.14	90.83	54.05	Sputtering	[24]
ITO/Ag/ITO/CPI	11.4	6.4	~87.5	41	Sputtering	[25]
GIO/Ag/GIO/quartz	8	11.3	92.9	42.4	Sputtering	[26]
ZnO/Ag/ZnO/PET	6	12.5	94.0	43	Sputtering	[3]
ITO/Ag/AZO/quartz	10	5.8	90.28	62	PLD and sputtering	[27]
ITO/Ag/ITO/glass	15	7.04	88.04	39.6	Sputtering	[28]
MGZO/Ag/MGZO /glass	9.5	10	94.7	58	Sputtering	[29]
ITO/glass	0	10	93	50	NA [(b)]	[30]

5.1.4 Conclusions

This paper presents a highly transparent and conductive ITO/ultra-thin silver/ITO sandwich structure on glass substrate. The superior optical and electric properties are achieved through the growth of stable continuous ultra-thin silver films, structural optimization using the transfer matrix method (TMM), and the utilization of high-temperature annealing in air. The resulting 7 nm-silver-thick structure demonstrates an average transmittance of up to 89.4% in the 400-800 nm range, equivalent to 96.0% relative to the glass substrate, and a sheet resistance of ~10 Ω/sq. These values surpass those of ITO films. This study also highlights the feasibility of

ion beam treatment for depositing ultra-thin silver films (6-7 nm) on ITO surfaces. Both vacuum annealing and annealing in air enhanced optical and electrical properties of the sandwich structure and annealing in air proves to be more effective, particularly in terms of silver film crystallization, which significantly influences the conductivity of the structure. After annealing in air, a distinct silver (200) peak, absent in as-deposited and vacuum-annealed samples, is observed. The close agreement between the experimental and simulation transmittance spectra indicates a cost-effective and efficient approach to engineering multi-layer optical structures. Overall, the resulting structure is an attractive transparent conductive electrode for various optoelectronic applications, as well as optical coatings such as low-E glass.

5.2 Examine the Optical Properties of Oxide / Ultra-Thin Silver / Oxide Sandwich Structures

This part of the chapter is adapted from Thanh Tran, and Qi Hua Fan, *"Examine the optical properties of oxide/ultra-thin silver/oxide sandwich structures",* MRS Advances

Publication Date: August 07, 2023

https://doi.org/10.1557/s43580-023-00624-z

5.2.1 Introduction

The scarcity of indium in the Earth's crust and its high demand for producing indium tin oxide (ITO) as transparent conductive electrodes in display and solar-cell applications have led to a rapid increase in indium prices [31]. Therefore, finding materials to replace ITO is crucial. However, replacing ITO in terms of electrical performance is challenging. Most reported transparent conductive oxides have conductivities higher than that of ITO [32, 33, 34]. Using a sandwich structure with a silver layer in the middle can solve the problem of low conductivity as

the silver layer can be highly conductive and contributes mostly to the conductivity [28]. Additionally, using a conductive and flexible metal layer in the middle can improve the electrode's flexibility [35]. Regarding the cost of the sandwich structures compared to ITO, we see that silver although as expensive as indium for now, the thickness of silver being used in the structure (6-7 nm) is much smaller than that of ITO (100-200 nm). By using this structure, we can reduce approximately 80% of materials costs compared to that of ITO if we use some low-cost oxides such as tin oxide (SnO_2). The other challenge is finding a structure with good transmittance in a desired wavelength range. Often, in sandwich structures, a thick layer of silver is used, which reduces the transmittance of the resulting film, especially in the infrared range, making it unsuitable for applications that require harnessing the light in that range [28]. With the help of an ion beam produced from a patented ion source, we were able to deposit ultra-thin and continuous silver films with thicknesses as thin as 6 nm [14, 36, 10, 11]. Based on our experimental results of depositing silver on glass, we expect the sheet resistances of sandwich structures containing 6 nm and 7nm silver films to be ~19 Ω/□ and ~11 Ω/□, respectively. It is good enough for most optoelectronic applications. Moreover, we were able to implement the silver layer in between two ITO layers to have electrical and optical properties as desired [37]. In this paper, we computationally examine the optical performance of sandwich structures of some typical oxides when implementing the 6 nm and 7 nm silver films. We use a Python package that employs the transfer matrix method (TMM) technique to calculate the transmittance spectrum [17, 18]. Our goal is to computationally find the best structures and specific designs to achieve optimum optical performance so that it can be a guidance for further experimental works.

5.2.2 Materials and Methods

In this work, we examine six different sandwich structures on glass, which are shown in **Table 5.4** with their corresponding names.

Table 5.4: Six sandwich structures examined in this work

Structure	Name
Glass / TiO_2 / Ag / AZO	Structure 1
Glass / ITO / Ag / SnO_2	Structure 2
Glass / ITO / Ag / ITO	Structure 3
Glass / AZO / Ag / SnO_2	Structure 4
Glass / SnO_2 / Ag / SnO_2	Structure 5
Glass / TiO_2 / Ag / SnO_2	Structure 6

Graphic illustration of sandwich structures is presented in **Figure 5.10**. In the execution, all the structure's designs with the top and bottom oxide layers having the thickness scanned in the range of 0-100 nm with a step size of 5 nm are calculated. In this work, two different values are used to evaluate the optical performance of a structure: average transmittance in the 300-1200 nm range ($T_{avg\text{-}300\text{-}1200}$) and average transmittance in the 400-800 nm range ($T_{avg\text{-}400\text{-}800}$). Average temperature in the range between wavelength $\lambda 1$ and $\lambda 2$ is calculated using the below formula:

$$T_{avg\_\lambda 1\_\lambda 2} = \frac{1}{(\lambda 2 - \lambda 1)} \int_{\lambda 1}^{\lambda 2} T_\lambda \, d\lambda$$

It is worth noticing that we should use a specific value to apply for a specific application. For example, to be used in different solar cells, different wavelength ranges should be applied and also the weight of transmittance at a certain wavelength should be calibrated according to the photon intensity of the solar radiation spectrum at that wavelength.

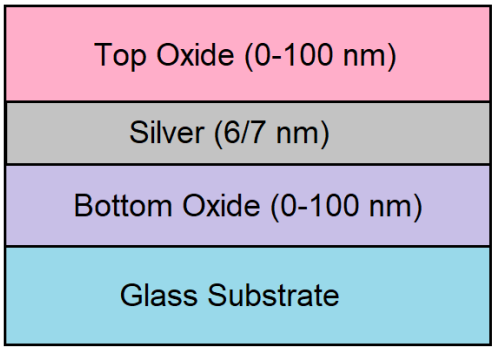

Figure 5.10: Sandwich structure examined in the simulation. Thickness of top and bottom oxides are varied from 0 to 100 nm with a step size of 5 nm. Thickness of silver layer is either 6 nm or 7 nm

After having the values calculated, the relationship between these values and the thicknesses of the top and bottom oxides layers are plotted in contour maps for each thickness of silver and each structure. Also, the optimum designs for each structure are extracted together with the transmittance spectrum for closer looks. The reflective indices are chosen for their high recognition among research societies as follows: Silica fused glass by Malitson et al. (1965) [38], ITO by König et al. (2014) [19], TiO2 by Sarkar et al. (2019) [39], SnO2 by Salman et al. (2018) [40], Ag by Rakić et al. (1998) [41], and AZO by Treharne et al. (2011) [42].

5.2.3 Optimizing average transmittance

Figure 5.11 shows an example of contour mapping for structure 6, where the values of $T_{avg\text{-}300\text{-}1200}$ and $T_{avg\text{-}400\text{-}800}$ are calculated and presented. The whole contour maps are shown in **Figure 5.12** and **Figure 5.13**. It is observed that each structure has an optimal design for the thickness of the bottom and top oxide layers to maximize the values of $T_{avg\text{-}300\text{-}1200}$ or $T_{avg\text{-}400\text{-}800}$. These designs vary for each structure and for each considered value.

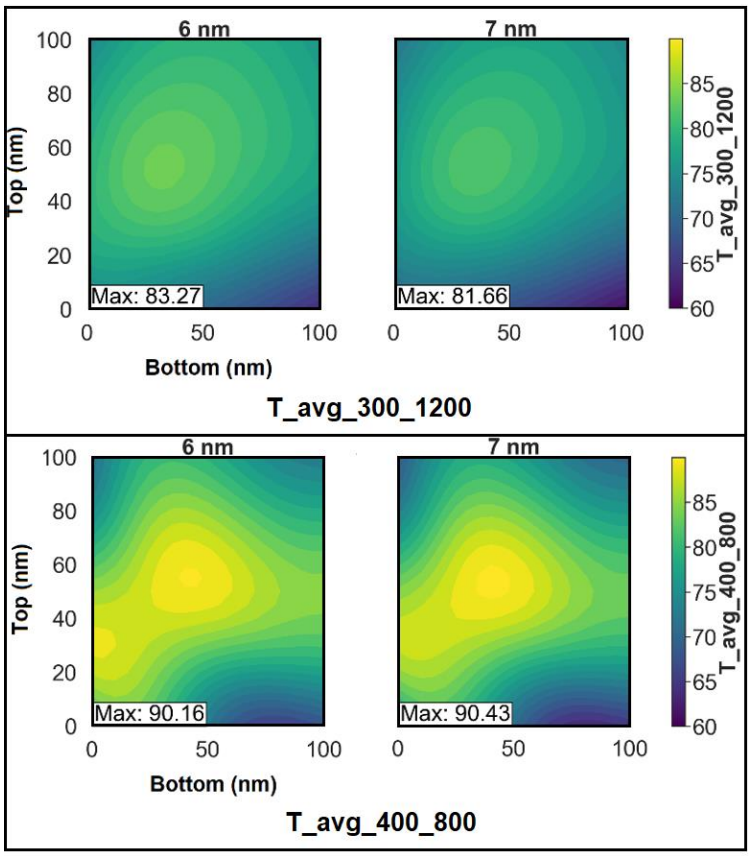

Figure 5.11: Contour maps of average transmittance in the 300-1200 nm wavelength range and 400-800 nm wavelength range of structure 6

Figure 5.14 illustrates the transmittance spectra of optimum designs of each structure when the thickness of the silver layer is 6 nm and 7 nm. Structure 1 is composed of a top oxide layer of aluminum-doped zinc oxide (AZO) and a bottom oxide layer of titanium dioxide (TiO_2). AZO exhibits higher transmittance than ITO [43], making the AZO sandwich structure better in terms of optical performance. According to simulation results, the maximum $T_{avg\text{-}300\text{-}1200}$ is 82.1 % when the silver film thickness is 6 nm, TiO_2 thickness is 35 nm, and AZO thickness is 55 nm.

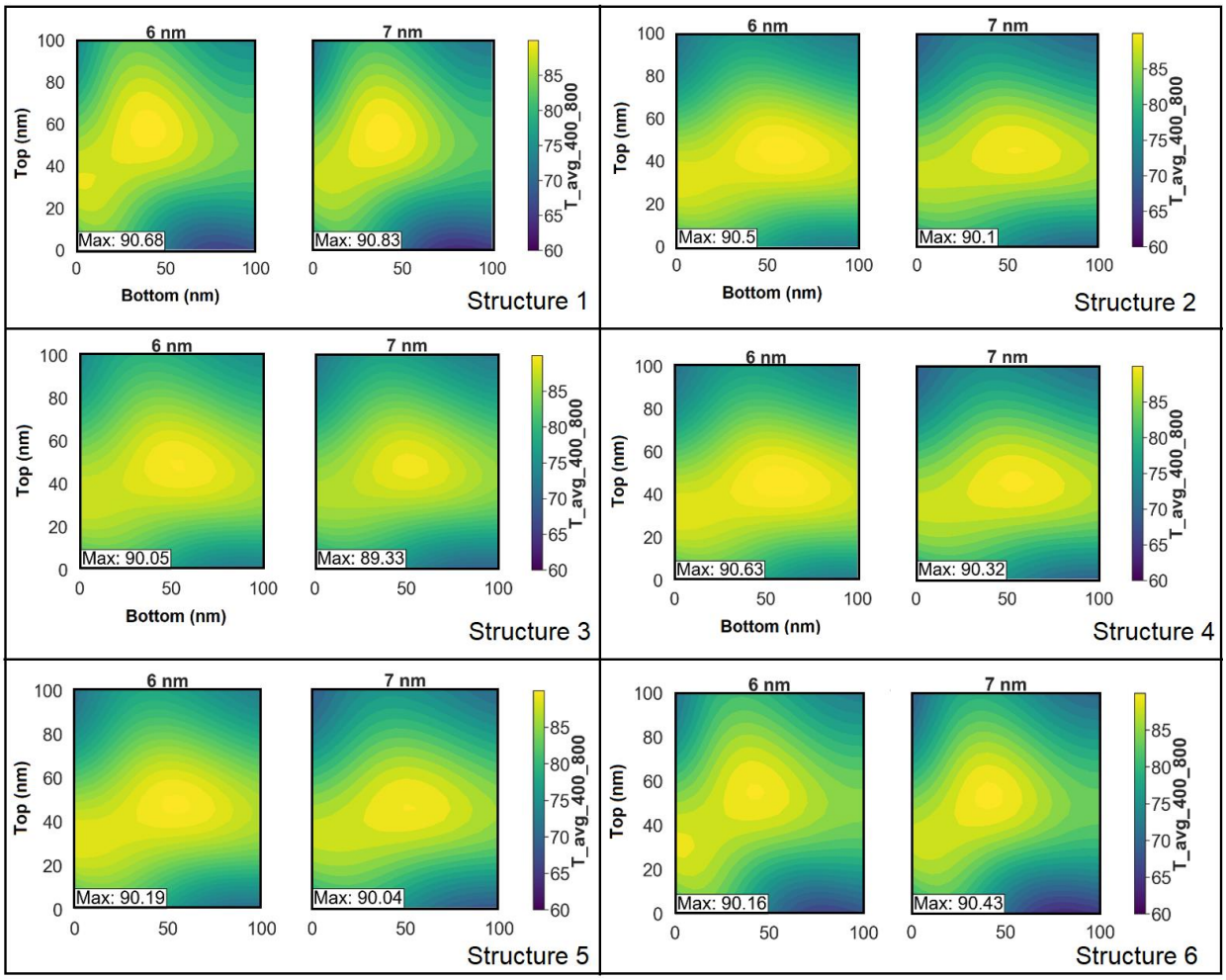

Figure 5.12: Contour maps presenting average transmittance in 400-800 nm range of the sandwich structures

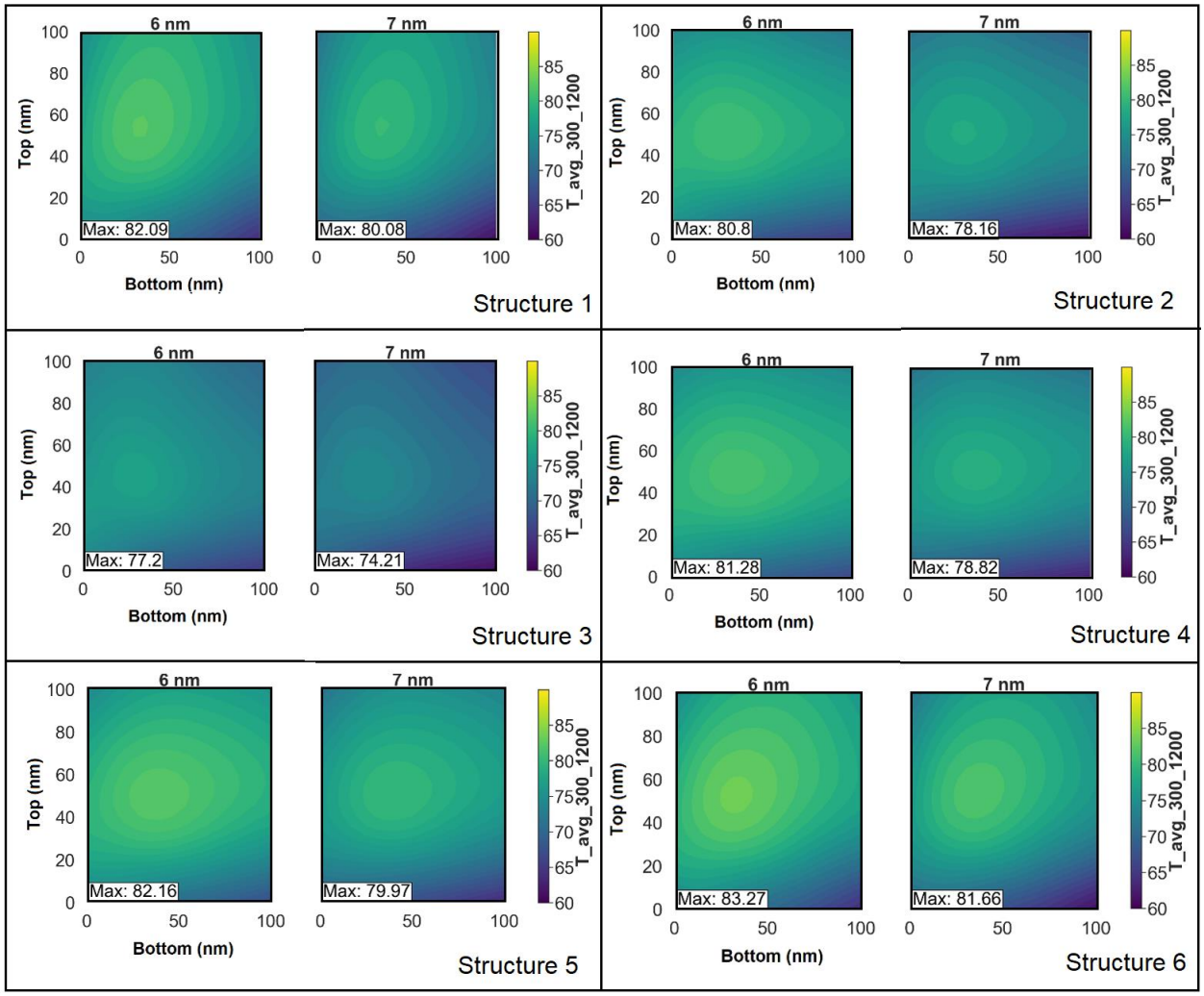

Figure 5.13: Contour maps presenting average transmittance in 300-1200 nm range of the sandwich structures

Even at a wavelength of 1200 nm, the transmittance of the structure can still reach 70%. The maximum $T_{avg\text{-}400\text{-}800}$ is 90.8 when the silver film thickness is 7 nm, TiO2 thickness is 40 nm, and AZO thickness is 55 nm. However, a drawback of this structure is that AZO degrades quickly when exposed to damp heat at 80°C and 85% relative humidity (RH) [44].

Structure 2 consists of a top oxide layer of tin oxide (SnO_2) and a bottom oxide layer of ITO. The maximum $T_{avg\text{-}300\text{-}1200}$ is 80.8 % when the silver film is 6 nm thick, ITO is 30 nm thick, and SnO_2 is 50 nm thick. The maximum $T_{avg\text{-}400\text{-}800}$ is 90.5 when the silver film is 6 nm thick,

ITO is 55 nm thick, and SnO_2 is 45 nm thick. The transmittance of this structure drops to around 60 % at 1200 nm when the thickness of silver is 6 or 7 nm. The advantage of this structure is that both ITO and SnO_2 are stable in damp heat [44].

Structure 3 consists of a top oxide layer of ITO and a bottom oxide layer of ITO. The maximum $T_{avg\text{-}300\text{-}1200}$ is 77.2 % when the silver film is 6 nm thick, the bottom ITO layer is 30 nm thick, and the top ITO layer is 45 nm thick. In this structure, the performance in the 300-1200 nm range is worse so far due to the rapidly decreasing transmittance in the infrared range. The maximum $T_{avg\text{-}400\text{-}800}$ is 90.0 when the silver film is 6 nm thick, the bottom ITO layer is 55 nm thick, and the top ITO layer is 50 nm thick. Another drawback of this structure is the uses of expensive materials: indium and silver.

Structure 4 consists of a top oxide layer of SnO_2 and a bottom oxide layer of AZO. Similar to structure 1, this structure contains AZO and it is not suitable for damp heat environment. The maximum $T_{avg\text{-}300\text{-}1200}$ is 81.3 % when the silver film is 6 nm thick, the bottom AZO layer is 35 nm thick, and the top SnO_2 layer is 50 nm thick. The maximum $T_{avg\text{-}400\text{-}800}$ is 90.6 when the silver film is 6 nm thick, the bottom AZO layer is 60 nm thick, and the top SnO_2 layer is 45 nm thick.

Structure 5 comprises a top oxide layer of SnO_2 and a bottom oxide layer of SnO_2, making it highly resistant to damp heat as SnO_2 is the best performer among SnO_2, AZO, and ITO [44]. The maximum $T_{avg\text{-}300\text{-}1200}$ is 82.2 % when the silver film is 6 nm thick, the bottom SnO2 layer is 40 nm thick, and the top SnO_2 layer, which are relatively high compared to other

structures. The transmittance at 1200 nm can be as high as 70% when the thickness of silver

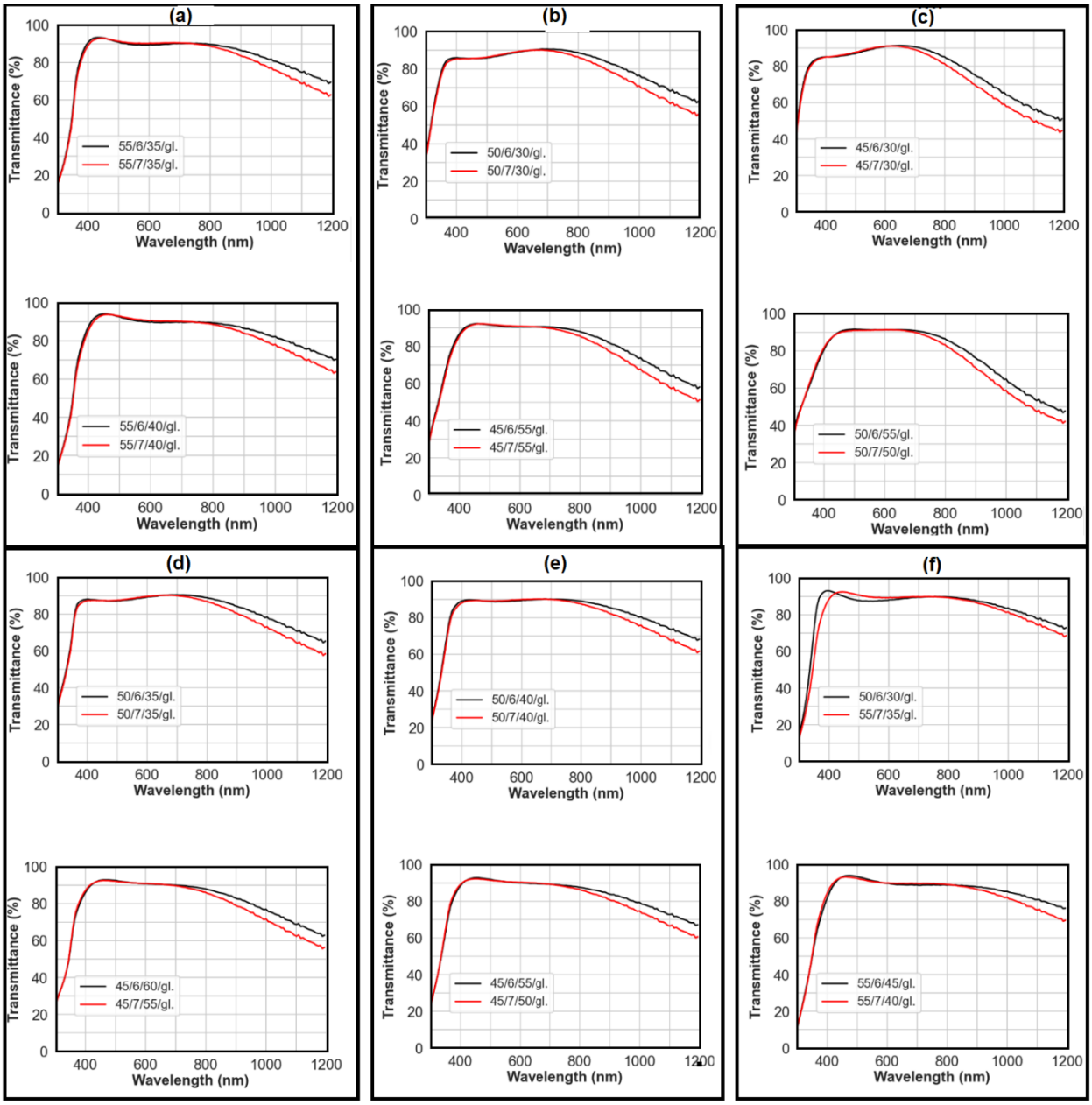

Figure 5.14: Transmittance spectra of optimum designs of six structures 1 (a), 2 (b), 3 (c), 4 (d), 5 (e), and 6 (f) with the top graph is for Tavg-300-1200 (top graph) and Tavg-400-800 (bottom graph)

layer is 6 nm. The maximum $T_{avg\text{-}400\text{-}800}$ is 90.2 % when the silver film is 6 nm thick, the bottom SnO_2 layer is 55 nm thick, and the top SnO_2 layer is 45 nm thick.

Structure 6 comprises a top oxide layer of SnO_2 and a bottom oxide layer of TiO_2, making it suitable for use in damp heat environments as both SnO_2 and TiO_2 are known to perform well in such conditions [44, 45]. The maximum $T_{avg\text{-}300\text{-}1200}$ is 83.3 % when the silver film is 6 nm thick, the bottom TiO_2 layer is 30 nm thick, and the top SnO_2 layer is 50 nm thick. This structure provides good transmittance in both infrared and ultraviolet ranges and therefore has the best $T_{avg\text{-}300\text{-}1200}$ among other structures studied in this work. The maximum $T_{avg\text{-}400\text{-}800}$ is 90.4 when the silver film is 7 nm thick, the bottom TiO_2 layer is 40 nm thick, and the top SnO_2 layer is 55 nm thick.

Figure 5.15 compares the optimum transmittances of the six structures side by side and reveals that Structure 3, which uses ITO as the oxide layers, provides worse performance. Most

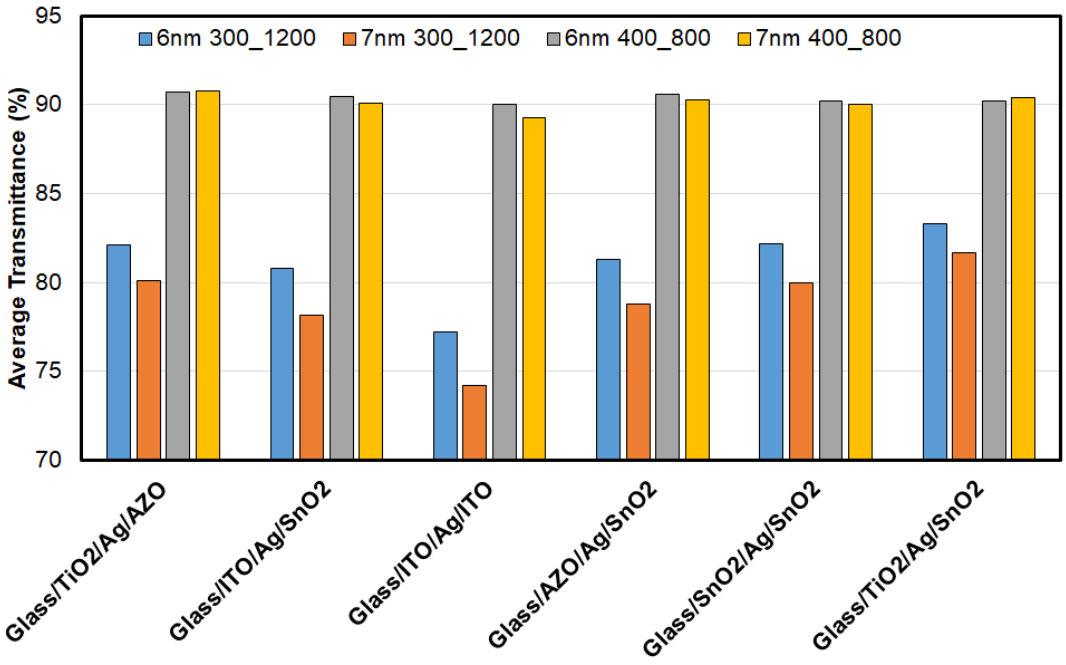

Figure 5.15: Summary of optimum transmittances of the six structures

of the structures can achieve similar $T_{avg\text{-}400\text{-}800}$. However, Structure 6 provides outstanding $T_{avg\text{-}300\text{-}1200}$ due to its high performance in the infrared and ultraviolet range of the light spectrum. Thinner silver films result in higher transmittance at the infrared range of the light spectrum for the 300-1200 nm range. On the other hand, for the 400-800 nm range, a 7 nm silver layer in Structures 1 and 6 can result in a higher average transmittance than a 6 nm layer. Among these cases, Structures 5 and 6 are potential choices for high optical performance and stability in a damp heat environment. In actual deposition of oxides films, it is likely that high temperature processing is needed so that the film's transparency can be high and comparable with simulation result as the reflective index are of highly crystallized films. For example, to obtain transmittance comparable to simulation results, the ITO/Ag/ITO/glass structure need annealing in air at 200C for 1 hour as reported [37]

For comparison purpose, **Figure 5.16** and **Figure 5.17** show the average transmittance in 400-800 nm range and 300-1200 nm range, respectively, of ITO films as functions of thickness ranging from 50 nm to 200 nm. The figures illustrate that in the 300-1200 range, ITO can give a

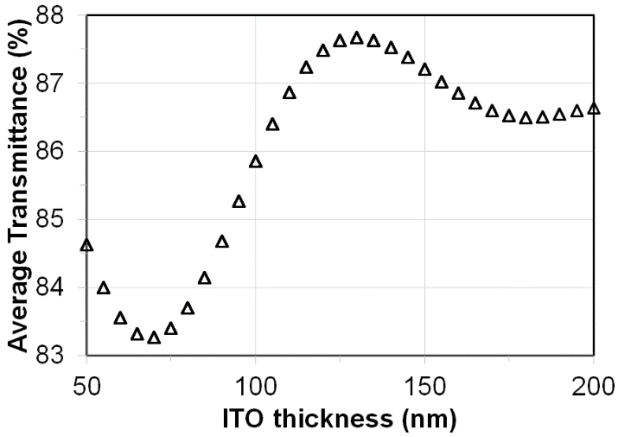

Figure 5.16: Average transmittance in 400-800 nm range of ITO films

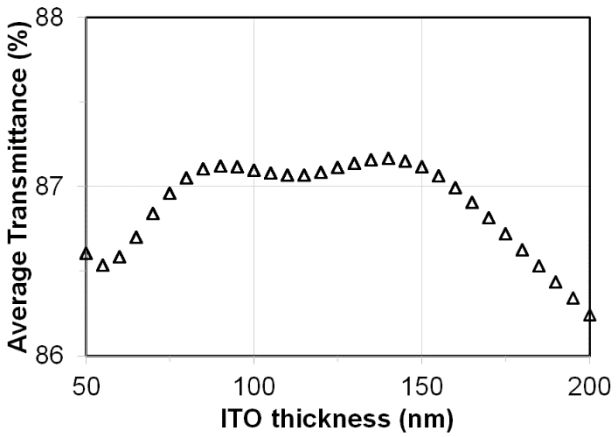

Figure 5.17: Average transmittance in 300-1200 nm range of ITO films

high average transmittance of 87.2 % at the thickness of around 140 nm. This is better than all of the reported structures in this work. This explains why ITO is still the best for silicon based solar cells, which harness wavelengths less than 1200 nm. However, in the 400-800 nm range, ITO yields the highest average transmittance of 87.5% at the thickness of around 130 nm. This is lower than most of the reported structure in this work.

5.2.4 Optimizing solar radiation for different applications

Figure 5.18 shows the three standard spectra of solar radiation. For space application, the standard spectrum is referred to as AM0 and it has an integrated power of 1366.1 W/m^2. Two standards are defined for terrestrial use. The AM1.5 Global spectrum is designed for flat plate

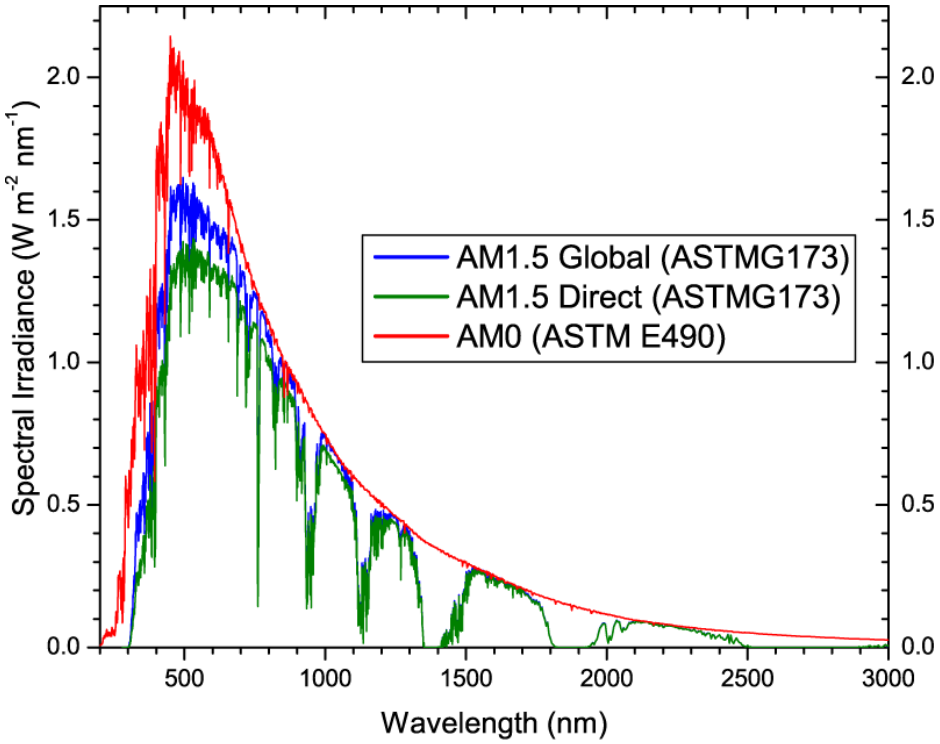

Figure 5.18: Standard Solar Spectra for space and terrestrial uses

modules and has an integrated power of 1000 W/m2 (100 mW/cm2). The AM1.5 Direct (+circumsolar) spectrum is formulated specifically for solar concentrator applications,

encompassing both the direct sunlight and the circumsolar component within a 2.5-degree radius around the sun. This combined spectrum, comprising direct and circumsolar components, exhibits an integrated power density of 900 W/m2. The SMARTS (Simple Model of the Atmospheric Radiative Transfer of Sunshine) program serves as a tool for producing standard spectra and is versatile enough to generate alternative spectra based on specific needs [46].

To evaluate the effectivity of the structure toward transferring solar radiation, we compare the energy of radiation going through the structure with the total energy of solar radiation. The

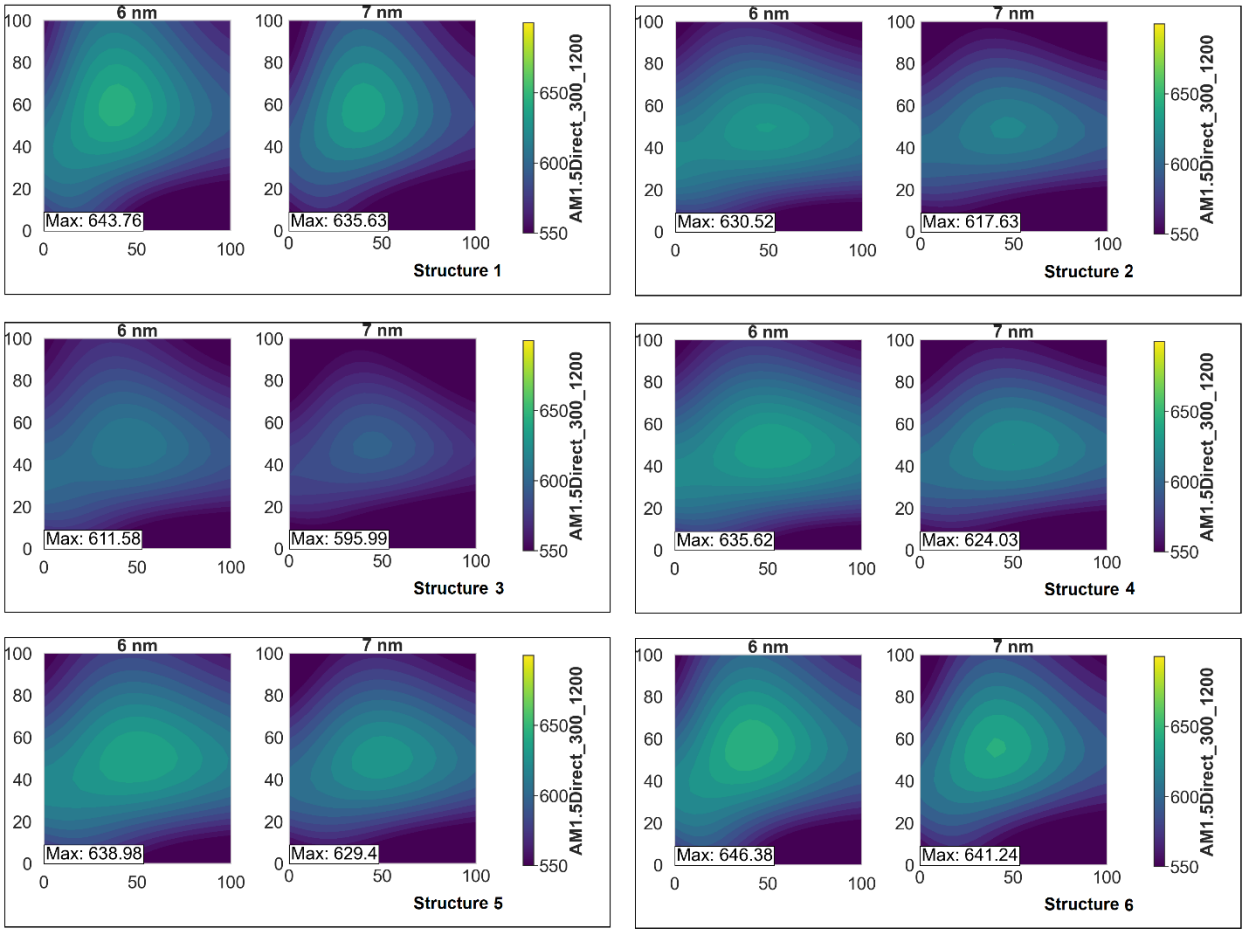

Figure 5.19: Contour maps of amount of energy from AM1.5 Direct solar radiation can transmit through the structures

formula below is used for calculating the energy passing through the structure of the wavelength from 300 nm to 1200 nm:

$$E = \int_{300}^{1200} AM\_1.5\_Direct_{\lambda}\, T_{\lambda}\, d\lambda$$

For the total solar energy of this range, we can do integral:

$E_{300-1200} = \int_{300}^{1200} AM1.5Direct_{\lambda}\ d\lambda = 740.7\ W/m^2$ out of 900 W/m^2 of the whole spectrum.

Structure 6 give the maximum transmitted energy of ~646 W/m^2, corresponding to ~87% of solar spectrum in the 300-1200 nm range (**Figure 5.19)**. **Figure 5.20** shows the transmitted energy of ITO film in the 300-1200 nm range as a function of thickness of ITO layer. It shows the maximum transmitted energy of ~652 W/m^2 at the thickness of ~130 nm. This is 1% higher than that of what structure 6 can provide shown in **Figure 5.19**.

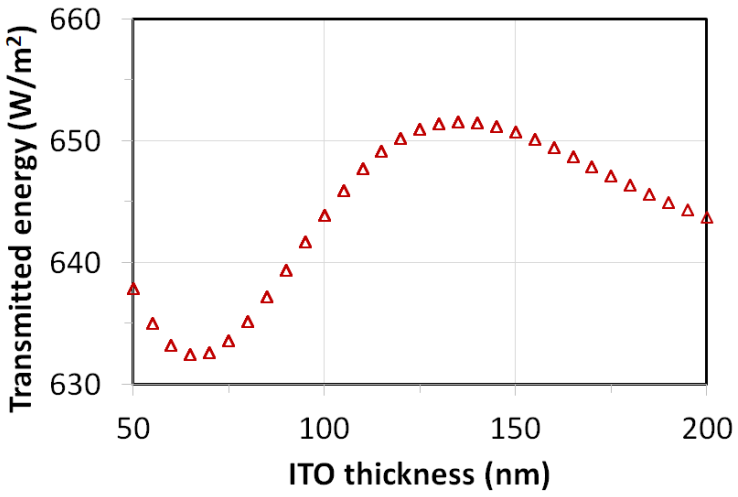

Figure 5.20: AM1.5Direct radiation transmission energy through ITO films as a function of ITO thickness

For solar panel application, the wavelength range can be different for different types of photovoltaic materials systems as shown in **table 5.5** [47]. Moreover, for solar panels, energy is quantized and therefore the number of photons above a specific energy should be taken into

consideration. Therefore, the power in the irradiation unit should be converted into the flux of photons using the equation calculating energy of one photon:

$$E_\lambda = \frac{hc}{\lambda}$$

We have the photon flux density is calculated as following:

$$I_{photon} = \frac{Irradiation}{E_\lambda} = Irradiation \times \frac{\lambda}{hc} \ (photon.s^{-1}.m^{-2}.nm^{-1})$$

As a result, **Figure 5.21** shows the density of photon flux as function of wavelength, and this illustrates the importance of long wavelength light. This emphasizes further the influence of ITO films in silicon-based solar cells as ITO has high transmittance in the infrared range of solar radiation. However, for other photovoltaic material systems such as typical OPV, perovskite and a-Si, GaInP, some of the reported structure might have better performance.

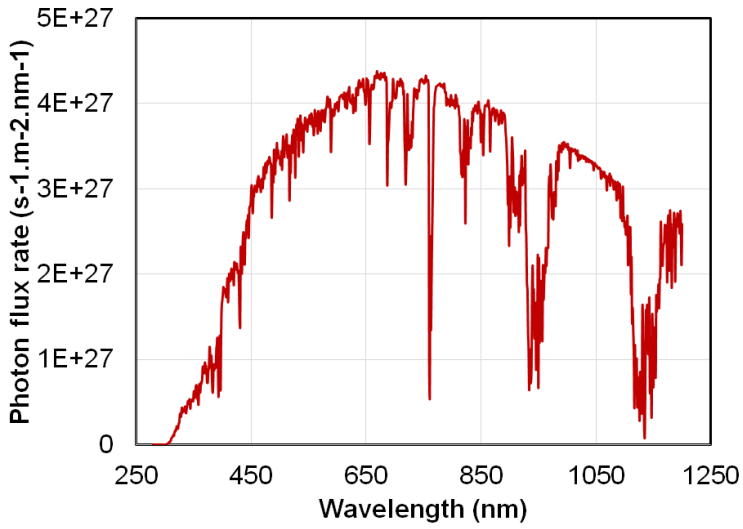

Figure 5.21: Photon spectra passing perpendicularly through a surface of 1 m2 in one second resulted from the AM1.5 Direct spectra

Table 5.5: Different photovoltaic material systems and their characteristics [47]. Reprinted with permission from Wiley

Photovoltaic material systems	Wavelength range Δλ [nm]	Bandgap [eV]	Efficiency SQL AM1.5G [%]
c-Si, m-Si, nc-Si, CIGS, CZTS	280–1100	1.13	33.4
GaAS, CdTe, InP, PbS QD	280–900	1.38	33.6
Dye/TiO_2 (DSSC)	280–830	1.49	32.2
Typical OPV, perovskite	280–800	1.55	31.4
a-Si, GaInP	280–700	1.77	27.7
AgrOPV (OPV for Agrivoltaics)	700–1100	1.13	17.4

5.2.5 Conclusion

This work employs the Transfer Matrix Method to compute the transmittances of multilayer films. The optical performances of six different sandwich structures containing typical oxides: TiO2, AZO, SnO_2, and TiO_2, were analyzed. Contour maps of $T_{avg\text{-}300\text{-}1200}$ and $T_{avg\text{-}400\text{-}800}$ as functions of the bottom and top oxide layer thicknesses were constructed with a thickness resolution of 5 nm, demonstrating that Glass / TiO_2 / Ag / SnO_2 and Glass / SnO_2 / Ag / SnO_2 are the two promising structures for optoelectronic applications. With the thickness of silver as thin as 6 nm, the transmittance at 1200 nm of these structures can be as high as 70-80%. The Glass / TiO_2 / Ag / AZO structure possesses high optical performance; however, AZO is not stable in damp heat environments, limiting this structure's applications. The method was applied for finding the structure to maximize energy of solar spectra transmitted as well as other optoelectronic applications. The result shows that structure 6 can provide a performance

comparable to the performance of ITO films. This work can guide further experimental work on making oxide-silver-oxide sandwich structures for a specific application.

REFERENCES

[1] Stadler, A. (2012). Transparent conducting oxides—an up-to-date overview. *Materials*, *5*(4), 661-683.

[2] Granqvist, C. G., & Hultåker, A. (2002). Transparent and conducting ITO films: new developments and applications. *Thin solid films*, *411*(1), 1-5.

[3] Zhao, G., Shen, W., Jeong, E., Lee, S. G., Yu, S. M., Bae, T. S., ... & Yun, J. (2018). Ultrathin silver film electrodes with ultralow optical and electrical losses for flexible organic photovoltaics. *ACS applied materials & interfaces*, *10*(32), 27510-27520.

[4] Lei, P., Chen, X., Yan, Y., Zhang, X., Hao, C., Peng, J., ... & Zhong, Y. (2022). Sputtered ITO/Ag/ITO Films: Growth Windows and Ag/ITO Interfacial Properties. *Journal of Electronic Materials*, *51*(5), 2645-2651.

[5] Johnson, P. B., & Christy, R. W. (1972). Optical constants of the noble metals. *Physical review B*, *6*(12), 4370.

[6] Nezhad, E. H., Haratizadeh, H., & Kari, B. M. (2019). Influence of Ag mid-layer in the optical and thermal properties of ZnO/Ag/ZnO thin films on the glass used in Buildings as insulating glass unit (IGU). *Ceramics International*, *45*(8), 9950-9954.

[7] Szczyrbowski, J., Dietrich, A., & Hartig, K. (1989). Bendable silver-based low emissivity coating on glass. *Solar Energy Materials*, *19*(1-2), 43-53.

[8] Hu, M., Gao, J., Dong, Y., Li, K., Shan, G., Yang, S., & Li, R. K. Y. (2012). Flexible transparent PES/silver nanowires/PET sandwich-structured film for high-efficiency electromagnetic interference shielding. *Langmuir*, *28*(18), 7101-7106.

[9] Lee, D., Lee, H., Ahn, Y., & Lee, Y. (2015). High-performance flexible transparent conductive film based on graphene/AgNW/graphene sandwich structure. *Carbon*, *81*, 439-446.

[10] Tran, T., Wang, X., Shrestha, M., Wang, K., & Fan, Q. H. (2023). Ultra-thin silver films grown by sputtering with a soft ion beam-treated intermediate layer. *Journal of Physics D: Applied Physics*.

[11] Tran, T., Shrestha, M., Baule, N., Wang, K., & Fan, Q. H. (2023). Stable Ultra-thin Silver Films Grown by Soft Ion Beam-Enhanced Sputtering with an Aluminum Cap Layer. *ACS Applied Materials & Interfaces*, 15, 29102–29109.

[12] Meshram, N., Loka, C., Park, K. R., & Lee, K. S. (2015). Enhanced transmittance of ITO/Ag (Cr)/ITO (IAI) multi-layered thin films by high temperature annealing. *Materials Letters*, *145*, 120-124.

[13] Sharma, S. K., & Spitz, J. (1980). Hillock formation, hole growth and agglomeration in thin silver films. *Thin Solid Films*, *65*(3), 339-350.

[14] Tran, T., Kim, Y., Baule, N., Shrestha, M., Zheng, B., Wang, K., ... & Fan, Q. H. (2022). Single-beam ion source enhanced growth of transparent conductive thin films. *Journal of Physics D: Applied Physics*, *55*(39), 395202.

[15] Bouroushian, M., & Kosanovic, T. (2012). Characterization of thin films by low incidence X-ray diffraction. *Cryst. Struct. Theory Appl*, *1*(3), 35-39.

[16] Tran, T., & Fan, Q. H. (2023). Examine the optical properties of oxide/ultra-thin silver/oxide sandwich structures. MRS Advances, 1-5.

[17] Byrnes, S. J. (2016). Multilayer optical calculations. *arXiv preprint arXiv:1603.02720*.

[18] Katsidis, C. C., & Siapkas, D. I. (2002). General transfer-matrix method for optical multilayer systems with coherent, partially coherent, and incoherent interference. *Applied optics*, *41*(19), 3978-3987.

[19] Konig, T. A., Ledin, P. A., Kerszulis, J., Mahmoud, M. A., El-Sayed, M. A., Reynolds, J. R., & Tsukruk, V. V. (2014). Electrically tunable plasmonic behavior of nanocube–polymer nanomaterials induced by a redox-active electrochromic polymer. *ACS nano*, *8*(6), 6182-6192.

[20] Zhang, C., Ji, C., Park, Y. B., & Guo, L. J. (2021). Thin-Metal-Film-Based Transparent Conductors: Material Preparation, Optical Design, and Device Applications. Advanced Optical Materials, 9(3), 2001298.

[21] Hu, Y., Zhu, J., Zhang, C., Yang, W., Fu, L., Li, D., & Zhou, L. (2019). Understanding the preferred crystal orientation of sputtered silver in Ar/N 2 atmosphere: a microstructure investigation. *Advances in Materials Science and Engineering*, *2019*.

[22] Gong, Y., Zhao, J., & Wang, Q. (2020). Arbitrarily high-order linear energy stable schemes for gradient flow models. *Journal of Computational Physics*, *419*, 109610.

[23] Haacke, G. (1976). New figure of merit for transparent conductors. *Journal of Applied physics*, *47*(9), 4086-4089.

[24] Wang, H., Tang, C., Shi, Q., Wei, M., Su, Y., Lin, S., & Dai, M. (2021). Influence of Ag incorporation on the structural, optical and electrical properties of ITO/Ag/ITO multilayers for inorganic all-solid-state electrochromic devices. *Ceramics International*, *47*(6), 7666-7673.

[25] Wu, C. C. (2018). Highly flexible touch screen panel fabricated with silver-inserted transparent ITO triple-layer structures. *RSC advances*, *8*(22), 11862-11870.

[26] Abe, Y., & Nakayama, T. (2007). Transparent conductive film having sandwich structure of gallium–indium-oxide/silver/gallium–indium-oxide. *Materials letters*, *61*(18), 3897-3900.

[27] Ren, N., Shi, P., Sheng, Z., Zhong, K., Du, H., Shan, Q., ... & Ban, S. (2020). Up to 98.2% super transmittance and precise modification of wavelength band in vein-like Ag in ITO/Ag/AZO sandwich structure. *Solar Energy*, *203*, 240-246.

[28] Ren, N., Zhu, J., & Ban, S. (2017). Highly transparent conductive ITO/Ag/ITO trilayer films deposited by RF sputtering at room temperature. *AIP Advances*, *7*(5), 055009.

[29] Zhang, Y., Liu, Z., Ji, C., Chen, X., Hou, G., Li, Y., ... & Zhang, X. (2021). Low-temperature oxide/metal/oxide multilayer films as highly transparent conductive electrodes for optoelectronic devices. *ACS Applied Energy Materials*, *4*(7), 6553-6561.

[30] Anand, A., Islam, M. M., Meitzner, R., Schubert, U. S., & Hoppe, H. (2021). Introduction of a novel figure of merit for the assessment of transparent conductive electrodes in photovoltaics: Exact and approximate form. *Advanced Energy Materials*, *11*(26), 2100875.

[31] Angmo, D., & Krebs, F. C. (2013). Flexible ITO-free polymer solar cells. *Journal of Applied Polymer Science*, *129*(1), 1-14.

[32] Pandey, R., Yuldashev, S., Nguyen, H. D., Jeon, H. C., & Kang, T. W. (2012). Fabrication of aluminum doped zinc oxide (AZO) transparent conductive oxide by ultrasonic spray pyrolysis. *Current Applied Physics*, *12*, S56-S58.

[33] Al-Kuhaili, M. F. (2021). Co-sputtered tantalum-doped tin oxide thin films for transparent conducting applications. *Materials Chemistry and Physics*, *257*, 123749.

[34] Nguyen, N. M., Luu, M. Q., Nguyen, M. H., Nguyen, D. T., Bui, V. D., Truong, T. T., ... & Nguyen-Tran, T. (2017). Synthesis of tantalum-doped tin oxide thin films by magnetron sputtering for photovoltaic applications. *Journal of Electronic Materials*, *46*, 3667-3673.

[35] Yang, W., Gong, Y., Yao, C. Y., Shrestha, M., Jia, Y., Qiu, Z., ... & Li, W. (2021). A fully transparent, flexible PEDOT: PSS–ITO–Ag–ITO based microelectrode array for ECoG recording. *Lab on a Chip*, *21*(6), 1096-1108.

[36] Fan, Q. H., Schuelke, T., Haubold, L., & Petzold, M. (2021). *U.S. Patent No. 11,049,697*. Washington, DC: U.S. Patent and Trademark Office.

[37] Tran, T., Shrestha, M., & Fan, Q.H., Highly transparent and conductive ITO/Ultra-thin Silver/ITO/glass sandwich structure for optical coatings and optoelectronic devices. *MRS Communications*.

[38] Malitson, I. H. (1965). Interspecimen comparison of the refractive index of fused silica. *Josa*, *55*(10), 1205-1209.

[39] Sarkar, S., Gupta, V., Kumar, M., Schubert, J., Probst, P. T., Joseph, J., & König, T. A. (2019). Hybridized guided-mode resonances via colloidal plasmonic self-assembled grating. *ACS applied materials & interfaces*, *11*(14), 13752-13760.

[40] Manzoor, S., Häusele, J., Bush, K. A., Palmstrom, A. F., Carpenter, J., Zhengshan, J. Y., ... & Holman, Z. C. (2018). Optical modeling of wide-bandgap perovskite and perovskite/silicon tandem solar cells using complex refractive indices for arbitrary-bandgap perovskite absorbers. *Optics express*, *26*(21), 27441-27460.

[41] Rakić, A. D., Djurišić, A. B., Elazar, J. M., & Majewski, M. L. (1998). Optical properties of metallic films for vertical-cavity optoelectronic devices. *Applied optics*, *37*(22), 5271-5283.

[42] Treharne, R. E., Seymour-Pierce, A., Durose, K., Hutchings, K., Roncallo, S., & Lane, D. (2011, March). Optical design and fabrication of fully sputtered CdTe/CdS solar cells. In *Journal of Physics: Conference Series* (Vol. 286, No. 1, p. 012038). IOP Publishing.

[43] Thestrup, B., & Schou, J. (1999). Transparent conducting AZO and ITO films produced by pulsed laser ablation at 355 nm. *Applied Physics A*, *69*, S807-S810.

[44] Pern, F. J., Noufi, R., Li, X., DeHart, C., & To, B. (2008, May). Damp-heat induced degradation of transparent conducting oxides for thin-film solar cells. In *2008 33rd IEEE Photovoltaic Specialists Conference* (pp. 1-6). IEEE.

[45] Geretschläger, K. J., Wallner, G. M., Hintersteiner, I., & Buchberger, W. (2016). Damp heat aging behavior of a polyamide-based backsheet for photovoltaic modules. *Journal of Solar Energy Engineering*, *138*(4).

[46] [Online]. Available: https://www.pveducation.org/pvcdrom/appendices/standard-solar-spectra.

[47] Anand, A., Islam, M. M., Meitzner, R., Schubert, U. S., & Hoppe, H. (2021). Introduction of a novel figure of merit for the assessment of transparent conductive electrodes in photovoltaics: Exact and approximate form. *Advanced Energy Materials*, 11, 21.

CHAPTER 6

ION BEAM-ASSISTED DC SPUTTERING OF TANTALUM-DOPED TIN OXIDE AT ROOM TEMPERATURE

This chapter is adapted from Thanh Tran, Maheshwar Shrestha, and Qi Hua Fan, *"Ion Beam-Assisted DC Sputtering of Tantalum-Doped Tin Oxide at Room Temperature"*, SCV 2023 Proceedings

Publication Date: October 25, 2023

https://doi.org/10.14332/svc23.proc.0006

Under permission from Society of Vacuum Coaters

6.1 Introduction

Indium tin oxide (ITO) has become increasingly expensive due to the scarcity of indium resources [1]. Consequently, there is a growing movement to reduce dependence on ITO in optoelectronic applications [1, 2, 3]. Several alternatives have been discussed, including graphene [4], aluminum-doped zinc oxide (AZO) [5], antimony-doped tin oxide (ATO), and fluorine-doped tin oxide (FTO) [6, 7, 8]. Among these alternatives, tantalum-doped tin oxide (TTO) has shown promise as a replacement due to its high transparency and conductivity, which have been demonstrated both experimentally and theoretically [9, 10]. Moreover, tin oxide exhibits excellent stability when exposed to damp heat at 80°C and 85% relative humidity (RH) [11]. However, TTO typically requires high processing temperatures [12] and non-industrial fabrication methods like pulsed laser deposition (PLD), and MOCVD [13, 14]. High temperature deposition is not compatible for many substrates such as PET and many applications also require low processing temperatures. At room and low temperatures, the performance of TTO films is

poor. For example, Yamada et. al reported a resistivity of 10 mΩ.cm of TTO film sputtered at 200°C [15].

In this study, we employed DC sputtering to deposit TTO films as it offers a high sputtering yield and practicality for production, especially since it supports rotational targets, which are crucial for industrial applications [16]. Additionally, our study investigates the influence of a soft ion beam on TTO deposition at room temperature. Ion beam-assisted deposition is known to enhance the deposition process by making the film denser through the provision of extra energy to atoms reaching the substrate's surface, thereby increasing their mobility [17]. However, high-energy ions can potentially damage the films through sputtering. Therefore, the use of a low-energy ion source is advantageous for thin film deposition. **Figure 6.1** illustrates the configuration of the ion beam-assisted sputtering chamber utilized in this study. The sputtering system (Kurt J. Lesker Company® PVD 75 PRO Line) featured 3-inch sputtering magnetrons with a shutter for pre-sputtering. A single beam ion source (SPR-10, Scion Plasma LLC) was integrated into the sputtering system, with both the ion gun and magnetron positioned towards the substrate center from different directions at an angle of approximately 60° [18]. The ion gun emitted argon ions with an estimated peak energy of 60 eV and a flux density of $1 \times 10^{20}\ \mathrm{m}^{-2}.\mathrm{s}^{-1}$ [19]. During the treatment, the ion source emitted ions towards the substrate throughout the deposition process. Since the appearance of ion beam enhances deposition rate, we used two different processing powers to have the same deposition rate in the cases with and without ion source.

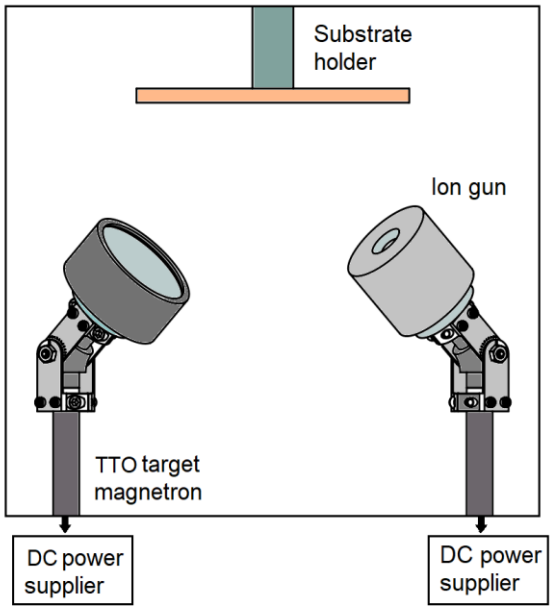

Figure 6.1: Configuration of sputtering chamber used in this study with an ion gun (source) implemented

6.2 Experimental and results

Two sets of samples were fabricated for comparison: one set was created with the assistance of an ion beam, while the other was created without such assistance. Each set of samples underwent a scan involving different flows of oxygen during the deposition process, as the oxygen flow plays a crucial role in TTO deposition. It is important to note that oxygen flow and ion beam are not independent variables. In conventional magnetron sputtering, the ion source can ionize oxygen atoms and propel an oxygen stream at a higher intensity and energy compared to oxygen simply hitting the substrate surface due to thermal dynamic movement. Consequently, the optical and electrical properties of the films in each set were compared.

In this study, the deposition rate and time were utilized as parameters to control the thickness of the films, assuming a constant deposition rate throughout the specific deposition

condition. Each rate test involved depositing a film for an extended period of time, ensuring a thickness exceeding 100 nm to guarantee measurement accuracy. The film thickness was measured using a profilometer (specifically, the DektakXT® stylus by Bruker). Prior to deposition, a thin ink line was drawn in the center of a cleaned substrate. After deposition, the ink layer, along with the atop TTO film layer, was removed using acetone in an ultrasonic bath, revealing a step profile that reflected the film's thickness. Subsequently, the deposition rates were determined based on the film thickness and the duration of the deposition process.

Table 6.1: Processing conditions of TTO films with and without IS. Ion source (IS) working condition: 120 V and 570 mA

Processing conditions of TTO	
Target	$Sn_{(1-x)}Ta_xO_2$, x=0.02
Target diameter	76.2 mm (3 inches)
Based pressure	1.3×10^{-4} Pa
Processing pressure	0.67 Pa
Processing gases	Argon and O_2
Discharge power	80 W (with IS)/ 60 W (without IS)
Deposition temperature	Room temperature
Deposition technique	DC magnetron sputtering

In the deposition process, borosilicate glass substrates were used, which have been previously reported to exhibit satisfactory optical performance [20]. Prior to deposition, these

substrates underwent a cleaning process followed by baking at elevated temperatures to eliminate contaminants and moisture from their surfaces. **Table 6.1** provides the processing parameters for the TTO deposition processes. The sputtering power was set at 80 W for the case without ion source (IS), and 60 W for the case with IS, in order to achieve similar deposition rates of approximately 10 nm/min, as the IS can enhance the deposition rate [19]. All depositions were carried out at room temperature. For the IS-enhanced deposition, the ion source was operated at 120V, resulting in a current of 570 mA. Under these conditions, the estimated ion energy is approximately 60V [19].

Optical transmittance was measured using a spectrophotometer (F20 thin-film measurement system, KLA Instruments). **Figure 6.2** depicts the transmittance spectra and the sum of transmittance and reflectance spectra of TTO films deposited without the assistance of an ion source. To achieve an optimal transmittance spectrum, a required oxygen flow rate of 1.25 sccm was observed in the total gas flow of 32 sccm, which resulted in a processing pressure of 0.67 Pa.

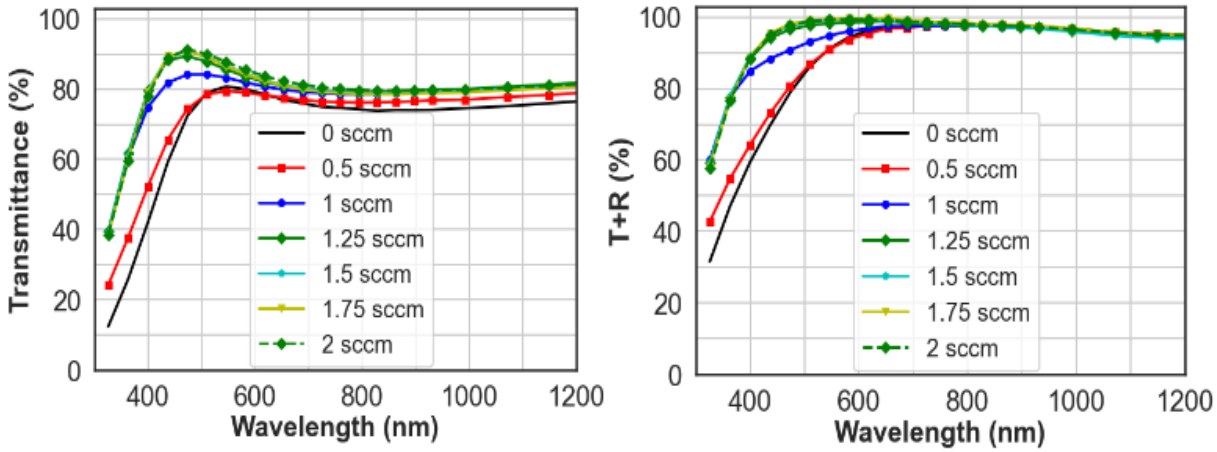

Figure 6.2: Transmittance (left) and sum of transmittance and reflectance (right) of TTO films deposited without assistance of ion beam at different flows of oxygen

A deficiency in oxygen content lowers the transmittance across the entire spectrum, but it primarily affects the sum of transmittance and reflectance in the short wavelength range. This indicates that the deficiency in this range of the T+R (transmittance plus reflectance) spectra is mainly attributed to the scattering of short wavelength light as it traverses through micro pores within the deposited films. The presence of oxygen enhances the mobility of metal atoms, as demonstrated in previous studies on silver metal, thereby aiding in the densification of the deposited films [21].

Figure 6.3 presents the optical performance of TTO films deposited with the assistance of an ion beam. In the case without oxygen added, the optical performance of the TTO film is slightly better than the case without ion-beam assistance. However, as soon as a small flow of oxygen (0.2 sccm in this case) was introduced into the chamber, the transmittance spectra of the TTO film significantly increased. This suggests that the ion beam amplifies the impact of oxygen on the sputtered films. The saturation spectrum of transmittance, beyond which the optical

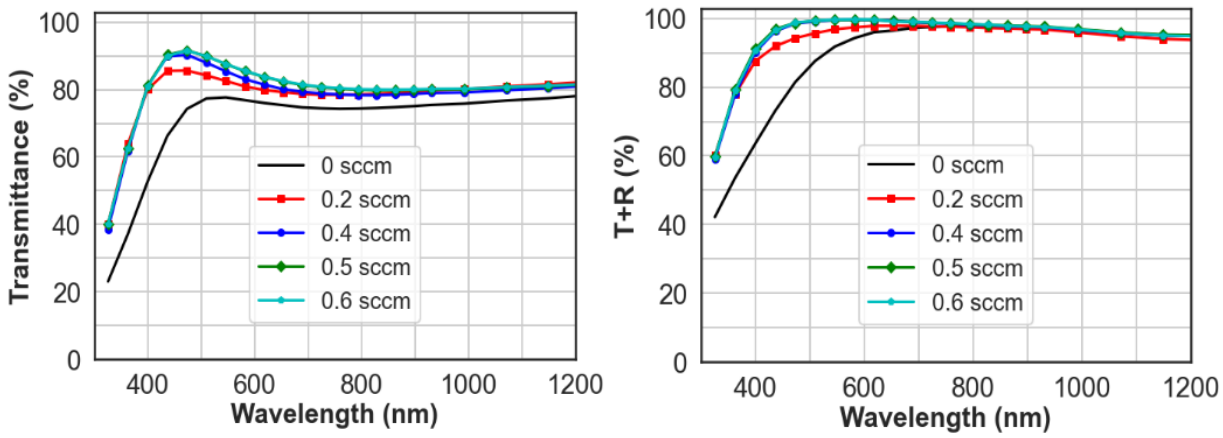

Figure 6.3: Transmittance (left) and sum of transmittance and reflectance (right) of TTO films deposited with the assistance of ion beam at different flows of oxygen

performance does not improve with the addition of more oxygen, is the same for both cases. This indicates that the porosity of the two films is likely similar.

The electrical properties were characterized using Hall measurements (MeasureReady ™ FastHall ™ Station, Lake Shore Cryotronics). **Figure 6.4** illustrates the resistivity of the deposited films in cases with and without ion source (IS) assistance. Other oxygen flow conditions are not shown in this figure as their resistivity is too high and it exceeds the measurement capacity of the Hall system. When the oxygen flow is too low, it can result in high porosity, as discussed in the optical performance section, leading to high resistivities due to reduced mobility of free carriers. As the oxygen flow over-increases, it lowers the free carrier concentration, as observed in **Figure 6.5**, consequently increasing the resistivity of TTO films. These mobility and carrier concentration behaviors give rise to the characteristic smile curve observed in the resistivity of typical transparent conductive oxides, such as ITO and TTO in this

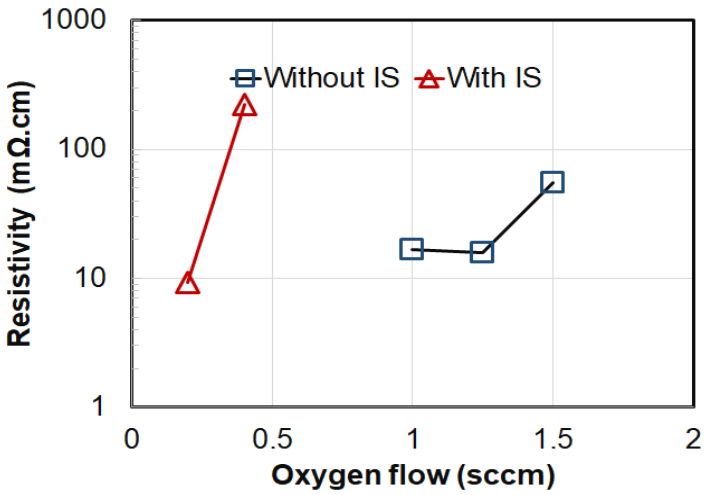

Figure 6.4: Resistivity of TTO films with and without assistance of ion beam at different flows of oxygen. Other data points are missing due to being out of measurement range

study. In the case with ion beam assistance, the lowest resistivity achieved was 9.3 mΩ.cm at an oxygen flow rate of 0.2 sccm, while in the case without IS, the optimum resistivity recorded was 15.9 mΩ.cm at an oxygen flow rate of 1.25 sccm.

Upon examining the concentration and mobility of free electrons in the TTO films as shown in **Figure 6.5**, no significant improvement in these properties is observed when the ion beam was utilized. However, the alignment of the optimum concentration and mobility of free electrons led to a better overall optimum resistivity in the TTO films with the assistance of the ion beam.

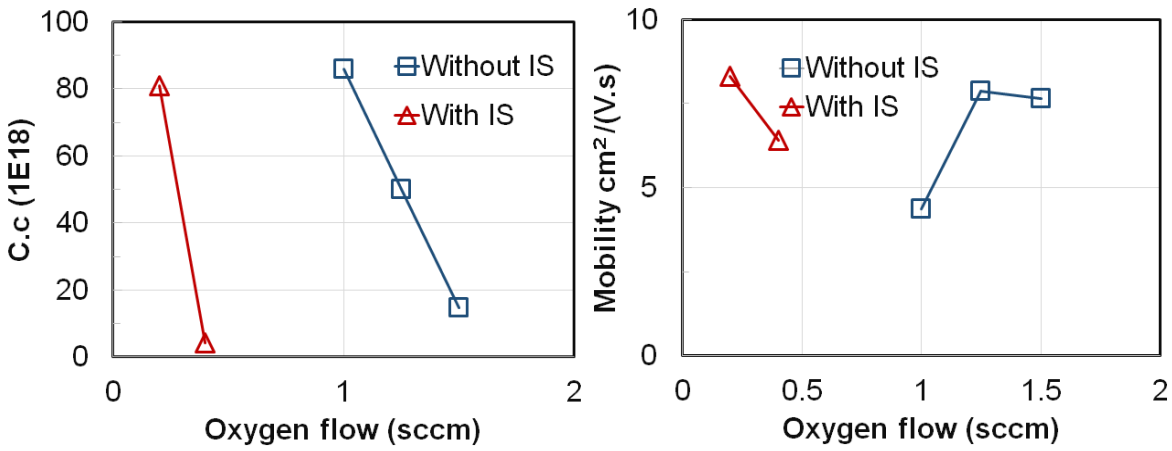

Figure 6.5: Carrier concentration (left) and mobility (right) of TTO films deposited with and without assistance of ion beam at varied flow of oxygen. Other data points are missing due to being out of measurement range

6.3 Discussion

The correlation between optical performance and oxygen flow was observed, and the deficiency of (T+R) was hypothetically explained by the scattering of light due to the presence of micro pores. These micro pores can account for the observed low mobility of free carriers. To further validate this hypothesis, additional analyses can be conducted to study the films. This includes XRD characterization using the Glancing Angle X-Ray Diffraction (GAXRD)

technique to examine thin films at a small incident angle of 2° [22]. Additionally, ellipsometry can be utilized as a useful method to analyze the refractive index and estimate the porosity of TTO films. Moreover, SEM imaging can provide valuable insights into the morphology of the TTO films.

With the introduction of the ion beam, the addition of oxygen into the films became more efficient, as evidenced by the lower oxygen flow required to achieve high transmittance and resistivity. The utilization of the ion beam as an assisting factor may be responsible for the improved alignment between the concentration and mobility of free carriers, resulting in a better resistivity when the ion beam was employed. The mechanism of incorporating oxygen into the film in the presence of the ion source is worth further investigation.

6.4 Conclusions

In conclusion, this research study has successfully investigated the influence of ion beam on the optical and electrical properties of DC-sputtered tantalum-doped tin oxide (TTO) films. By varying the oxygen flow, we demonstrated that the ion source plays a crucial role in facilitating the efficient incorporation of oxygen into the films, resulting in improved transparency and reduced resistivity. The observed alignment of mobility and concentration of free carriers in the ion beam treated TTO films further enhanced their resistivity. The obtained resistivity of 9.3 mΩ.cm and an average transmittance of 79% in the range of 400 nm to 1200 nm highlight the promising performance of the ion beam treated TTO films. These findings contribute to a better understanding of the ion beam-assisted deposition process for TTO films and open avenues for optimizing their optical and electrical properties for various applications.

REFERENCES

[1] Cattin, L., Bernède, J. C., & Morsli, M. (2013). Toward indium-free optoelectronic devices: dielectric/metal/dielectric alternative transparent conductive electrode in organic photovoltaic cells. *physica status solidi (a)*, 210(6), 1047-1061.

[2] Boileau, A., Hurand, S., Baudouin, F., Lüders, U., Dallocchio, M., Bérini, B., ... & Fouchet, A. (2022). Highly Transparent and Conductive Indium-Free Vanadates Crystallized at Reduced Temperature on Glass Using a 2D Transparent Nanosheet Seed Layer. *Advanced Functional Materials*, 32(5), 2108047.

[3] Kumar, A., & Zhou, C. (2010). The race to replace tin-doped indium oxide: which material will win?. *ACS nano*, 4(1), 11-14.

[4] Arvidsson, R., Kushnir, D., Molander, S., & Sandén, B. A. (2016). Energy and resource use assessment of graphene as a substitute for indium tin oxide in transparent electrodes. *Journal of Cleaner Production*, 132, 289-297.

[5] Eshaghi, A., & Hajkarimi, M. (2014). Optical and electrical properties of aluminum zinc oxide (AZO) nanostructured thin film deposited on polycarbonate substrate. *Optik*, 125(19), 5746-5749.

[6] Kwak, D. J., Moon, B. H., Lee, D. K., Park, C. S., & Sung, Y. M. (2011). Comparison of transparent conductive indium tin oxide, titanium-doped indium oxide, and fluorine-doped tin oxide films for dye-sensitized solar cell application. *Journal of Electrical Engineering & Technology*, 6(5), 684-687.

[7] Chowdhury, F. I., Blaine, T., & Gougam, A. B. (2013). Optical transmission enhancement of fluorine doped tin oxide (FTO) on glass for thin film photovoltaic applications. *Energy Procedia*, 42, 660-669.

[8] Weidner, M., Jia, J., Shigesato, Y., & Klein, A. (2016). Comparative study of sputter-deposited SnO2 films doped with antimony or tantalum. *physica status solidi (b)*, 253(5), 923-928.

[9] Al-Kuhaili, M. F. (2021). Co-sputtered tantalum-doped tin oxide thin films for transparent conducting applications. *Materials Chemistry and Physics*, 257, 123749.

[10] Williamson, B. A., Featherstone, T. J., Sathasivam, S. S., Swallow, J. E., Shiel, H., Jones, L. A., ... & Scanlon, D. O. (2020). Resonant Ta doping for enhanced mobility in transparent conducting SnO2. *Chemistry of Materials*, 32(5), 1964-1973.

[11] Pern, F. J., Noufi, R., Li, X., DeHart, C., & To, B. (2008, May). Damp-heat induced degradation of transparent conducting oxides for thin-film solar cells. In *2008 33rd IEEE Photovoltaic Specialists Conference* (pp. 1-6). IEEE.

[12] Nguyen, N. M., Luu, M. Q., Nguyen, M. H., Nguyen, D. T., Bui, V. D., Truong, T. T., ... & Nguyen-Tran, T. (2017). Synthesis of tantalum-doped tin oxide thin films by

magnetron sputtering for photovoltaic applications. *Journal of Electronic Materials*, 46, 3667-3673.

[13] Nakao, S., Yamada, N., Hitosugi, T., Hirose, Y., Shimada, T., & Hasegawa, T. (2010). Fabrication of highly conductive Ta-doped SnO2 polycrystalline films on glass using seed-layer technique by pulse laser deposition. *Thin Solid Films*, 518(11), 3093-3096.

[14] Lee, S. W., Kim, Y. W., & Chen, H. (2001). Electrical properties of Ta-doped SnO 2 thin films prepared by the metal–organic chemical-vapor deposition method. *Applied Physics Letters*, 78(3), 350-352.

[15] Yamada, N., Nakao, S., Hitosugi, T., & Hasegawa, T. (2010). Sputter Deposition of High-Mobility Sn1-xTaxO2 Films on Anatase-TiO2-Coated Glass. *Japanese journal of applied physics*, 49(10R), 108002.

[16] Kim, J. H., Seong, T. Y., Ahn, K. J., Chung, K. B., Seok, H. J., Seo, H. J., & Kim, H. K. (2018). The effects of film thickness on the electrical, optical, and structural properties of cylindrical, rotating, magnetron-sputtered ITO films. *Applied Surface Science*, 440, 1211-1218.

[17] Akbari, A., Templier, C., Beaufort, M. F., Eyidi, D., & Riviere, J. P. (2011). Ion beam assisted deposition of TiN–Ni nanocomposite coatings. *Surface and Coatings Technology*, 206(5), 972-975.

[18] Tran, T., Shrestha, M., Baule, N., Wang, K., & Fan, Q. H. (2023). Stable Ultra-thin Silver Films Grown by Soft Ion Beam-Enhanced Sputtering with an Aluminum Cap Layer. *ACS Applied Materials & Interfaces*.

[19] Tran, T., Kim, Y., Baule, N., Shrestha, M., Zheng, B., Wang, K., ... & Fan, Q. H. (2022). Single-beam ion source enhanced growth of transparent conductive thin films. *Journal of Physics D: Applied Physics*, 55(39), 395202.

[20] Tran, T., Wang, X., Shrestha, M., Wang, K., & Fan, Q. H. (2023). Ultra-thin silver films grown by sputtering with a soft ion beam-treated intermediate layer. *Journal of Physics D: Applied Physics*.

[21] Gu, D., Zhang, C., Wu, Y. K., & Guo, L. J. (2014). Ultrasmooth and thermally stable silver-based thin films with subnanometer roughness by aluminum doping. *Acs Nano*, 8(10), 10343-10351.

[22] Bouroushian, M., & Kosanovic, T. (2012). Characterization of thin films by low incidence X-ray diffraction. *Cryst. Struct. Theory Appl*, 1(3), 35-39.

CHAPTER 7

CONCLUSION AND FUTURE WORKS

7.1 Conclusion

This study has investigated the distinctive attributes of a novel ion source and its application in modifying sputtered transparent conductive materials. Notably, the ion source's capacity to generate an ion beam at low voltage and assist in magnetron sputtering has been pivotal. The resultant ITO films exhibit significantly improved electrical and optical performances. Furthermore, the ion beam induces alterations in the crystallization of silver films. By utilizing ion beam assistance, silver atoms rearrange in a (100) orientation, as opposed to their natural (111) orientation, thereby augmenting silver's wettability. This ion-beam-assisted silver layer serves as an intermediate structure, substantially enhancing the optical and electrical properties of ultra-thin silver films. Leveraging the ion source, continuous fabrication of silver films as thin as 6 nm has been achieved. To bolster the stability of these resulting silver films, an aluminum cap layer of approximately 0.2 nm was introduced. This layer operates expectedly under a cathodic protection mechanism, shielding the underlying silver films. Moreover, the aluminum cap layer mitigates the mobility of silver surface atoms, thereby enhancing the film's thermal stability. This low surface atoms mobility can help to prevent the migration of silver ions in the oxidation-migration-reaggregation model and enhance environmental stability of the silver layer.

Employing these ultra-thin stable silver films in an ITO/silver/ITO sandwich structure yields films with remarkable optical, electrical, and thermal stability. Subsequent annealing at elevated temperatures further enhances the films' optical and electrical properties, equaling simulation results and surpassing ITO in the visible range. Remarkably, we observed silver (200)

peak in sandwich structures after annealing in the air with grain size of that of ITO grains together with enhancement in optical and electrical performances. Computational analysis of additional sandwich structures, incorporating a 6 and 7 nm silver layer, has revealed the optical performance of structures like $SnO_2/Ag/TiO_2$ comparable to that of ITO across a broad spectrum of wavelengths. By employing an ultra-thin layer of silver and low-cost oxides like SnO_2, the expectation for material costs is as low as 20% of those associated with typical ITO films used in optoelectronic applications. This research lays the groundwork for the design of tailored sandwich structures for specific applications.

Lastly, an experimental study was conducted on ion beam-assisted sputtered tantalum-doped tin oxide. This investigation highlights the ion source's ability to enhance the electrical properties of TTO films deposited at room temperature by effectively infusing energized oxygen into the films. The explored TTO films hold promise as an oxide layer within the sandwich structure, potentially replacing ITO in various optoelectronic applications.

7.2 Future Works

This work lays the foundational groundwork for employing sandwich structures utilizing ultra-thin stable silver films as a substitute for ITO in optoelectronic applications. However, despite the accomplishments, there remain several areas for improvement and future exploration. The following suggestions for future work highlight these potential areas:

7.2.1 Investigate deposition of other TCOs

The efficacy of ion beam assistance has been demonstrated for ITO and TTO films. It is crucial to extend this investigation to encompass other Transparent Conductive Oxides (TCOs) such as AZO, TiO_2, and FTO, exploring both ion beam-assisted and non-assisted deposition methods. To enhance comprehensiveness, higher deposition temperatures, ions/atoms incident

angles, and post-processing techniques should be considered. Additionally, assessing the performance of deposited films using techniques like ellipsometry can contribute valuable data for designing sandwich structures. Determining the refractive index of deposited films through ellipsometry is recommended for a more comprehensive analysis. These reflective indices are useful for optical design of sandwich structures.

7.2.2 Study further wettability and stability of silver films

While this research considered 6 nm as the limit for silver film thickness, further exploration with even thinner ultra-thin silver films could lead to enhanced optical performance in sandwich structures. Therefore, investigating the wettability of ion beam-assisted silver layers on various substrates, such as TTO, FTO, AZO, and TiO2, is crucial. Exploring alternative sputtering gases, like nitrogen, which can potentially alter the growth direction of silver films, should also be considered, as it might offer improved properties over traditional argon gas. Moreover, conducting additional research on the protective mechanism of the aluminum cap layer is necessary to understand the physics behind it. In conjunction with experimental research, computational approaches can be employed. For instance, molecular dynamics (MD) simulation can be utilized to calculate the mobility of silver surface atoms in the presence of aluminum atoms. Additionally, testing other metals for comparison of mobilities can provide valuable insights.

7.2.3 Experimentally investigate other sandwich structures

The fabrication of potential sandwich structures is a practical focus of further research. While the ITO/Ag/ITO structure demonstrates excellent agreement between experimental and computational results after annealing in the air within this study, it is important to note that the

same level of success may not be guaranteed for other sandwich structures due to various possibilities.

For instance, silver ultra-thin films might not be stable on the surfaces of other oxides. In such cases, a thin layer of ITO can be employed as a stabilizing factor. Another consideration is that the processing or annealing temperature for other oxides might need to be elevated to achieve an optimum transmittance spectrum. In these instances, it becomes crucial to use compatible processing conditions to attain the corresponding refractive indexes for optimizing the structures.

7.2.4 Study environmental, thermal, and mechanical stability of Oxide/silver/oxide structures

Examining the stability of the mentioned sandwich structures is crucial for their practical application. Various environmental tests, such as annealing at high temperatures and damp heat tests, can provide valuable insights. In a standard damp heat test, samples are subjected to an environment with a temperature of approximately 85°C and a relative humidity of 85% for an uninterrupted period of 1,000 hours.